



Back to Single-carrier for beyond-5G communications above 90 GHz

Grant agreement ANR-17-CE25-0013

Deliverable D3.1

Performance assessments

| | |
|----------------------|--|
| Delivery date | 28/10/2021 |
| Version | 1.0 |
| Editor | J-B. Doré (CEA-Leti) |
| Authors | SIRADEL: Y. Corre, L. Mavel, CEA-Leti: J-B. Doré, CentraleSupélec: M. Alawieh, M. Saad, C. Bader |
| Dissemination | Public |
| Keywords | Sub-THz, Beyond 5G, Simulation, Integration, Evaluation plan |

History

| Version | Date | Modification | Author(s) |
|---------|------------|---------------|-----------|
| 1.0 | 30/11/2021 | First version | J-B. Doré |

Executive summary

The work package WP3 in BRAVE has two objectives: 1) integrate the main project's innovations and scenarios into simulation test platforms; and then 2) produce evaluation results for demonstration and dissemination of beyond-5G (B5G) technologies found valuable. This deliverable D3.1 describes the main integrated results of the project: Performance of investigated physical layers over various sub-THz environments digitally modelled.

The integration and tests rely on simulation platforms that produce the evaluation of our technologies performance in B5G scenarios and under realistic physical conditions.

- A **network design simulator** (S_5GConnect) gathers 3D geographical data, deterministic propagation models and system simulations for the calculation and analysis of KPIs (key performance indicators) related to the 5G mobile access network and last-mile wireless backhaul. It also embeds automatic design features (sites selection and configurations) for the optimization of various kinds of network topologies. The simulator is enriched by the integration of sub-THz channel models and modulations developed in BRAVE work package WP2. It is also extended with new indoor capabilities, and new automatic design algorithms devoted to the joint access and wireless backhaul optimization. This simulator has been employed in work package WP3 for the assessment of several networks that operate in the sub-THz spectrum: outdoor mesh last-mile backhaul, fixed wireless access (FWA), hotspot, and shopping mall broadband networks.
- A **link budget simulator** gathers or calculates all components of the system link budget, based on the considered scenario (e.g., range, phase noise and propagation conditions) and the system performance indicators (typically BER versus SNR). It facilitates the comparison between different system configurations or techniques; verifies the feasibility with current sub-THz transmission technologies, and the respect of existing regulation; and finally, evaluates what would be the power consumption by the proposed system. The link budget simulator is completed with two interfaced link-level simulators, which have been previously developed in work package WP2. Two scenarios have been considered: line-of-sight (LoS) device-to-device (D2D); and kiosk.

The above-mentioned test platforms are integrating four different PHY-layer innovations elaborated in BRAVE work package WP2:

1. [Innovation #1] The proposed **polar-modulation scheme (P-QAM)** is robust to medium and high phase noise levels, which are expected to affect the sub-THz RF chain. The performance of this P-QAM modulation has been evaluated under Gaussian phase noise and additive white gaussian noise (AWGN) channel to produce the SNR-SE mapping tables that relate the achievable spectral efficiencies (SE) to a required signal-to-noise ratio (SNR). Those tables are integrated in the WP3 test platforms, and applied in various scenarios: backhaul, FWA, and hotspot.
2. [Innovation #2] A **MIMO system with non-coherent modulation and simple energy detection at the receiver** is a convenient way to transport multiple streams and combat the phase noise

effect, along with limited complexity. The PHY link-level simulator that was developed in work package WP2 for design of the communication system and preliminary evaluation is extended by plugging a basic ray-tracing channel simulation and realistic antenna radiation patterns. Results will be fed into the link budget simulator, considering a D2D applications.

3. [Innovation #3] The **Generalized Space Modulation (GSM) and its dual-polarized version (DP-GSM)** have been identified as a possible solution to reach high spectral efficiency with lower power consumption. The PHY link-level simulator that was used for preliminary assessment of this technology is enhanced in work package WP3: made compliant with ray-tracing channel predictions; comparison of various modulation schemes, including the conventional Spatial Modulation (SM) and alternative Index Modulation approaches (IM). Results are outputted towards the link budget simulator to capture the performance of such a system in hotspot scenario.
4. [Innovation #4] The **reconfigurable Filter Shape Index Modulation (FSIM)** has been proposed recently along with novel filter IM domain, and it has been identified as a very promising candidate to reach low-power wireless ultra-high data rates while overcoming the main subTHz limitation. The PHY-link level simulator for SISO and MIMO FSIM also considers the sub-THz ray-tracing channels and the sectored antenna channel model with phase noise. This proposed reconfigurable system is evaluated in different configurations with/without channel coding for hotspot and D2D scenarios.

The assessment of sub-THz communication techniques requires the propagation channel to be properly simulated, i.e. with realistic path-loss, departure/arrival angles, frequency response, MIMO properties and adequate relationship with the environment. **Ray-based propagation models** for both outdoor and indoor scenarios have been upgraded for the considered frequencies, for instance with exploitation of a street-level LiDAR point cloud. Those models are employed in work package WP3 in two different ways, either by feeding link-level simulators (described here above) with realistic channel data; or by supporting the evaluation and dimensioning of candidate sub-THz network topologies into the network design simulator S_5GConnect.

The five considered test scenarios escribed in [1] are:

- Scenario #1: Outdoor mesh backhaul,
- Scenario #2: Fixed Wireless Access (FWA),
- Scenario #3: Shopping mall,
- Scenario #4: Short-range D2D,
- Scenario #5: Kiosk / hotspot.

The innovations, test platforms and scenarios are gathered to form the three BRAVE integrated demonstrators:

- Demonstrator #1: MIMO D2D (Device to Device),
- Demonstrator #2: Index Modulation D2D and hotspot,
- Demonstrator #3: Access and backhaul network design.

The shape of those demonstrators can be summarized as follow.

Blocks of the three BRAVE demonstrators.

| Demonstrators | Innovations | Simulators | Scenarios |
|------------------|-------------|----------------|----------------|
| MIMO D2D | #2,#4 | Link budget | #4 |
| Index Modulation | #3,#4 | Link budget | #4, #5 |
| Network design | #1, #3 | network design | #1, #2, #3, #5 |

Although lots of research efforts have been undertaken with state-of-the-art devices and channel propagation in the last years, sub-THz techniques are still not mature enough compared to microwave or photonics technologies. The substantial studies and technical advances provided in this project allow taking a step forward on developing realistic sub-THz communication systems.

We demonstrate that optimizing the modulation and demodulation schemes for PN channels results in significant performance gains for future sub-THz systems. In addition, the combination of MIMO with spectral-efficient IM scheme and power-efficient SC modulations allows reaching an ultra-high throughput with low power consumption. This combination considers that the long-term evolution roadmap of the next-generation telecommunications systems (Beyond-5G) will point to an energy-efficiency dominated era. This approach shows many advantages compared to its predecessor in sub-GHz high data-rate systems (e.g., IEEE 801.11ax). Following this approach, different MIMO candidate systems (GSM, SMX, DP-GSM, DP-SMX, SMX-FSIM) are investigated, where SMX-FSIM is the most promising developed solution for low-power wireless Tbps. Last, we have highlighted that using MIMO systems with ED receivers is a valuable solution for D2D applications. It allows achieving high data-rate communications with low complexity and low-power transceivers in sub-THz frequencies.

These results sound here of significant advances in a path still full of challenges. Several technical challenges on power consumption, low complexity RF architectures, and compact antenna designs need to be overcome to realize the development and deployment of future wireless sub-THz communication devices.

Table of content

| | |
|--|-----------|
| 1 INTRODUCTION | 7 |
| 2 CASE STUDIES..... | 9 |
| 2.1 SCENARIO #1: FIXED WIRELESS ACCESS | 9 |
| 2.1.1 <i>Introduction</i> | 9 |
| 2.1.2 <i>Models and assumptions</i> | 10 |
| 2.1.3 <i>Simulation results</i> | 16 |
| 2.1.4 <i>Conclusion</i> | 21 |
| 2.2 SCENARIO #2: WIRELESS BACKHAUL IN A LARGE VENUE (SHOPPING MALL)..... | 21 |
| 2.2.1 <i>Introduction</i> | 22 |
| 2.2.2 <i>Models and assumptions</i> | 22 |
| 2.2.3 <i>Simulation results</i> | 23 |
| 2.3 SCENARIO #3: KIOSK AND ENHANCED WLAN IN OFFICE ENVIRONMENT..... | 24 |
| 2.3.1 <i>Proposed S-EGSM system</i> | 25 |
| 2.3.2 <i>Proposed Generalized MIMO system with FSIM scheme</i> | 33 |
| 2.3.3 <i>Proposed coded FSIM</i> | 44 |
| 2.3.4 <i>Conclusion</i> | 48 |
| 2.4 SCENARIO #4: HOTSPOT ACCESS NETWORK | 49 |
| 2.4.1 <i>Introduction</i> | 49 |
| 2.4.2 <i>Models and assumptions</i> | 49 |
| 2.4.3 <i>Simulation results</i> | 51 |
| 2.5 SCENARIO #5: SHORT-RANGE D2D..... | 54 |
| 2.5.1 <i>Non coherent OOK transceiver with energy detection</i> | 54 |
| 2.5.2 <i>Coded coherent MIMO SMX-FSIM for D2D</i> | 61 |
| 3 CONCLUSION..... | 65 |
| 4 REFERENCES | 66 |
| 5 APPENDICES | 70 |
| 5.1 APPENDIX A: OPEN DATA | 70 |
| 5.1.1 <i>Point-to-point backhaul performance data</i> | 70 |
| 5.1.2 <i>MIMO channel samples for kiosk scenario</i> | 70 |
| 5.2 APPENDIX B: URBAN BACKHAUL LINK ANALYSIS | 74 |
| 5.2.1 <i>System parameters and Scenario</i> | 75 |
| 5.2.2 <i>Performance evaluation</i> | 76 |
| 5.2.3 <i>Impact of the Phase Noise level</i> | 78 |
| 5.2.4 <i>Conclusion</i> | 79 |

List of Acronyms

| | |
|------------------|---|
| 5G | 5th Generation |
| 5G-NR | 5G New Radio |
| APM | Amplitude Phase Modulation |
| AWGN | Additive White Gaussian Noise |
| B5G | Beyond 5G |
| BER | Bit Error Rate |
| CPE | Customer Premises Equipment |
| CPM | Continuous Phase Modulation |
| D2D | Device to Device |
| DPSK | Differential Phase Shift Keying |
| EIRP | Equivalent Isotropic Radiated Power |
| FEC | Forward Error Correction |
| FWA | Fixed Wireless Access |
| GSM | Generalized Spatial Multiplexing |
| IM | Index Modulation |
| KPI | Key Performance Indicator |
| LiDAR | Light Detection and Ranging |
| LoS | Line-of-Sight |
| MIMO | Multiple Inputs Multiple Outputs |
| NLoS | Non LoS |
| OOK | On Off Keying |
| PA | Power Amplifier |
| PAPR | Peak to Average Power Ratio |
| PER | Packet Error Rate |
| PHY-layer | Physical layer |
| PN | Phase Noise |
| P-QAM | Polar - Quadrature Amplitude Modulation |
| PSK | Phase Shift Keying |
| QAM | Quadrature Amplitude Modulation |
| QPSK | Quadrature Phase Shift Keying |
| RF | Radio Frequency |
| Rx | Receiver / Received |
| SE | Spectral Efficiency |
| SM | Spatial Multiplexing |
| SNR | Signal to Noise Ratio |
| Sub-THz | Sub-TeraHertz |
| Tx | Transmitter / Transmit |
| UE | User Equipment |
| ULA | Uniform Linear Array |
| URA | Uniform Rectangular Array |
| WLAN | Wireless local area network |

1 Introduction

After definition of beyond-5G scenarios and new spectrum opportunities in work-package WP1 of BRAVE project [1] [2], elaboration of new models for the sub-THz physical layer [3] and design of adapted efficient waveforms [3] [4] within work-package WP2, the proposed solutions are demonstrated in work-package WP3.

More precisely, the work-package WP3 has two main goals. First, it consists in integrating the building blocks developed in work-package WP2 for evaluation in a more sophisticated and realistic simulation environment. Second, it must produce evaluation results to assess the feasibility and interest of the proposed solutions and scenarios, but also feed the demonstration and promotion tasks. The wireless systems performance are evaluated based on different metrics: data rate, bit error rate, coverage range, network capacity, and power consumption.

The assessment studies rely on three demonstrators described in [5]:

1. Demonstrator #1: MIMO D2D (Device-to-device).
2. Demonstrator #2: Index modulation D2D and hotspot.
3. Demonstrator #3: Access and backhaul network design.

Section 2 of this document describes and assesses the performance of the WP2 investigated concepts in five scenarios.

1. **Scenario #1 (demonstrator #3):** Fixed wireless Access (FWA); Based on a fine model of the environment and the performance abstraction of the single carrier P-QAM modulation, results and statistical analysis are discussed. The network deployment optimization is designed with an automatic planning tool.
2. **Scenario #2 (demonstrator #3):** Indoor Wireless backhaul in a shopping mall. In this use case, a shopping-mall area with strong required capacity for mobile and fixed wireless connectivity is investigated. As for scenario #1, Single carrier P-QAM modulation is assumed to derive figure of merits of the sub-THz network.
3. **Scenario #3 (demonstrator #2):** Kiosk and enhance WLAN in an office environment. Based on a fine model of the channel propagation in an office area, the potential of the index modulation schemes (e.g., GSM, DP-GSM and FSIM) is demonstrated from different perspectives (e.g., spectral/energy efficiencies, robustness to PN, cost and computational complexity). In addition, a link budget estimation demonstrates the order of magnitude of the energy consumption for the envisaged schemes. Different configurations (number of antennas, indexation strategies) are investigated, discussed and compared.
4. **Scenario #4 (demonstrator #3):** Hotspot with very low complexity transceiver. The considered scenario is a small hotspot area for which a low complexity non-coherent receiver based on the concatenation of a LDPC coded OOK modulator / energy detector is investigated and compared to a coherent receiver with P-QAM modulation.

5. **Scenario #5 (demonstrators #1 and #2):** Short-range D2D. This last scenario explores the feasibility of providing short-range subTHz connectivity between devices with low complexity. For this use case, two strategies are discussed. On the one hand, we present a solution combining spatial multiplexing (with up to 8 antennas) and non-coherent receiver to increase the spectral efficiency. On the other hand, a coherent receiver using MIMO Filter Shape index modulation (FSIM) is investigated to reach much higher spectral and energy efficiencies at a low cost.

Many data sets describing the modulation and the channel realization used for the numerical simulations are open. We provide a description of how to use them in appendices.

2 Case studies

2.1 Scenario #1: Fixed Wireless Access

The presented case study is based on demonstrator #3 described in [5], using the access and backhaul network design functionalities, as well as the P-QAM modulation.

2.1.1 Introduction

5G standards and beyond aim at bringing broadband mobile connectivity everywhere. High-traffic areas such as urban centers are nowadays served through dense small-cell networks. Such high-capacity networks need appropriate backhauling and using sub-THz frequency bands is expected to be a key element to meet those requirements in the beyond-5G context [1] [6]. Fixed Wireless Access (FWA) networks take advantage of progress in mobile technology to offer high-speed fixed connectivity at a low cost. Indeed, while 80 % of the data traffic takes place indoors, fiber may not be available everywhere as it is sometimes too much of an investment for Internet Service Providers (ISPs). Combining FWA with a wireless transport backhaul is a relevant step-by-step process for an ISP who wants to start addressing the fixed data demand for a neighborhood. The network can later be complemented with more fiber points if the capacity is not sufficient. Such 5G solutions are already operational based on sub-6GHz or millimeter-wave frequencies, especially in North America. Using sub-THz frequencies for the last-mile backhaul, but also the access layer is a relevant option with FWA as links are static, which allows the choice of an ideal receiver position (height, optical visibility).

A preliminary BRAVE study was published in [7] for characterization of the backhaul sub-THz links in a North-American urban area; it is reported in Appendix B. In this section, we consider the realistic design of a FWA network in a residential environment, and we aspire at assessing and highlighting the challenges of a combined access and last-mile wireless backhaul at 150 GHz. The study relies on accurate simulations, namely through 1) detailed map data obtained with Light Detecting And Ranging (LiDAR) measurements, 2) cutting-edge propagation model [8] and 3), performance of an adequate polar-QAM sub-THz modulation scheme [9]. Algorithms for automated infrastructure design is another component that participates the study. Recently, the need for high-throughput wireless backhaul has pushed some actors to present innovative methods for millimeter-wave planning [10]. Beyond coverage, one of the main challenges in planning communication networks is to address the capacity constraints. The development of an adequate automated design process for a sub-THz FWA network was a strong activity in work-package 3, relying on the optimization codes available at SIRADEL.

All necessary elements for design and assessment of the sub-THz FWA network were integrated into the demonstrator #3 described in [5].

A major FWA use-case is for an ISP to bring coverage for individual homes in residential areas; this is the scenario we decided to investigate using the 150 GHz spectrum. A few fiber Point-of-Presences (PoP) with connection to the core network are distributed in main streets of the considered area. Lampposts and poles locations in the area have been designated as candidates for both the FWA and the wireless backhaul network. Our objective was to demonstrate by simulation the feasibility of such a deployment, to assess the achievable user throughputs and the required infrastructure, and to make

a comparison to a similar deployment at conventional 5G frequencies (3.5 GHz at the access layer, and 28 GHz for the backhaul).

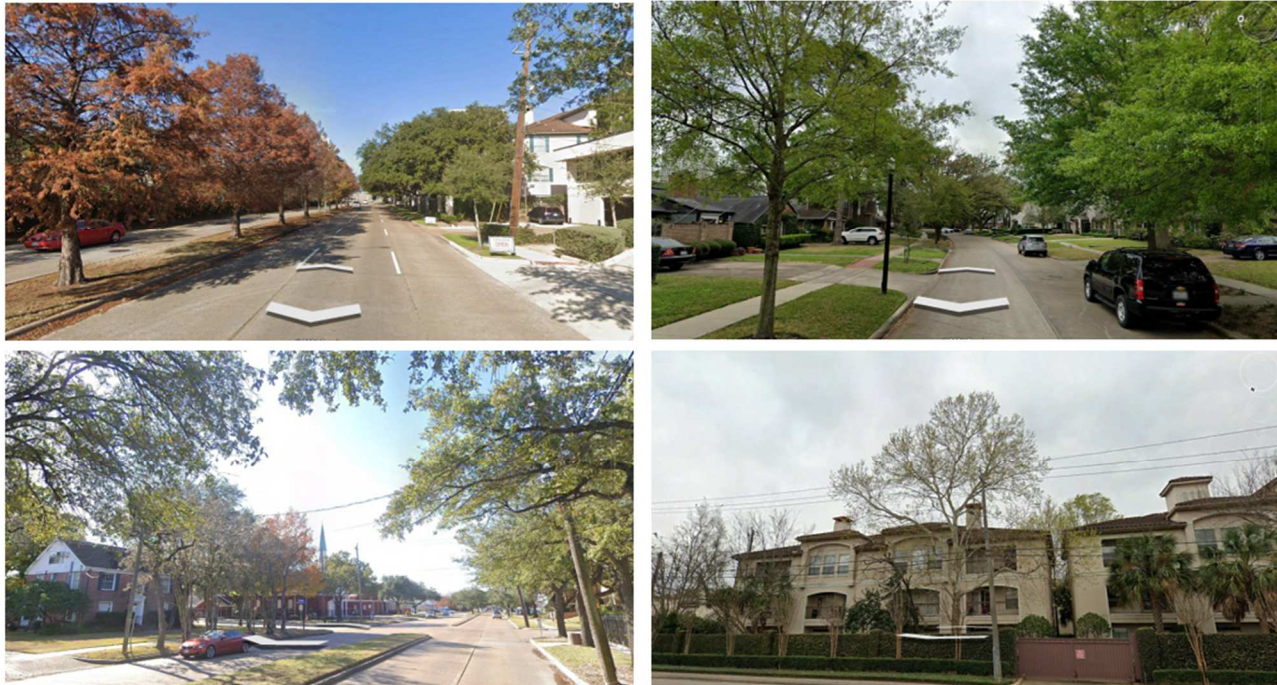


Figure 1 : Google Earth pictures from the considered study area.

2.1.2 Models and assumptions

2.1.2.1 Network architecture

The proposed case study does address the last-mile backhaul and access layers of the Fixed Wireless Access (FWA) network. The considered architecture is depicted in Fig. 2.

The fiber Points of Presence (PoPs) are nodes where the last-mile wireless backhaul connects the optical fiber and the core network. Backhaul Units (BUs) are wireless backhaul devices. In our scenario, a wireless backhaul link is formed by two dedicated connected BUs with static antenna orientations. A BU is possibly installed at the same site as other BUs to form a hierarchical multi-hop backhaul architecture. The wireless backhaul network is connected to the fiber PoP with a tree topology, i.e. the network is an acyclic graph where any node is at least of degree 1. An Access Point (AP) is the ultimate network node that connects the Customer Premises Equipment (CPE). It is either co-sited with a BU or PoP for attachment to the backhaul and core network. Sites that connect APs to the core network without providing any access connectivity are called relay sites. Finally, the CPE is installed at the user house or premises to get fixed broadband internet access, and then feed the user's local area network.

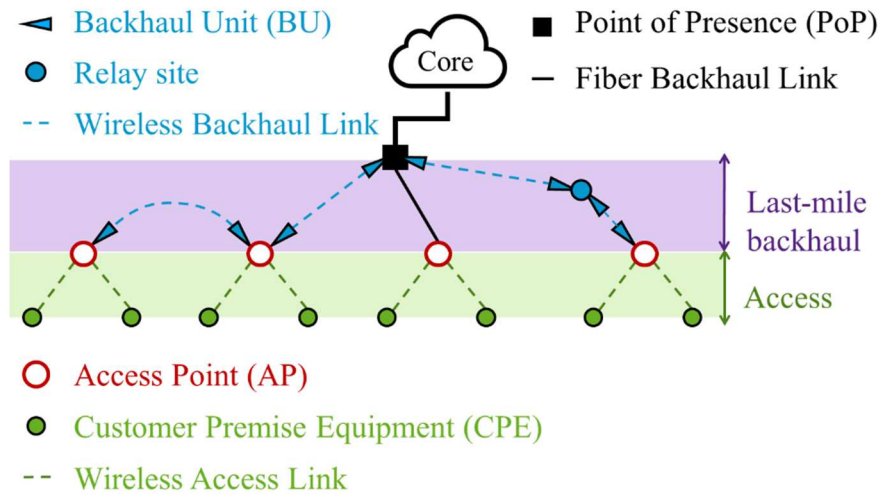


Figure 2 : Considered FWA network architecture.

2.1.2.2 3D digital model & Propagation losses

The case study is conducted in Houston's (US), into a 0.52 km² wide residential area where LiDAR data was recently collected by SIRADEL (Figure 3). The LiDAR data was processed and classified to get a very accurate digital representation of the environment, including buildings, slanted rooftops, trunks, foliage, and poles. It is completed with a vectorized representation of the building contours to form the 3D geographical digital model.

This 3D digital model provides several important inputs to the case study, incl.:

- Candidate CPE positions, i.e. typically against the building vertical façade or on the rooftop, depending on the FWA operator's installation strategy.
- Candidate positions for APs and backhaul DUs: lampposts, electrical poles or dominant rooftops.

The 3D digital model is also exploited for construction of the propagation multi-paths (reflections and diffractions on the vectorized building façades) and computation of the high-frequency propagation losses (obstruction by buildings and vegetation). Note that we have set the average in-vegetation loss equal to 6 dB/m. There is one difference compared to the predictions shown in previous BRAVE deliverables [11] [3]. Most buildings in the Houston case studies are houses with slanted rooftops; then the VOLCANO propagation model [11] has been enhanced to consider the LiDAR-based rooftop detailed representation. This allows for a more accurate discrimination between LoS and NLoS situations; this also prevents from the construction of erroneous reflections or diffractions at the higher part of the building façade.

Besides, when the radio network nodes and links are displayed on top of the 3D digital model, this offers a very comprehensible view of the proposed deployment and obtained performance.

The processing of the LiDAR point cloud consists in a series of operations, which have been increasingly automated by SIRADEL during the BRAVE project's period: data alignment, corrections, filtering, classification, etc. Finally, a sub-meter accuracy of 3D digital model is obtained, which is sufficient for our case study (fictitious deployment scenario) but is also found relevant for high-frequency radio-planning tasks.

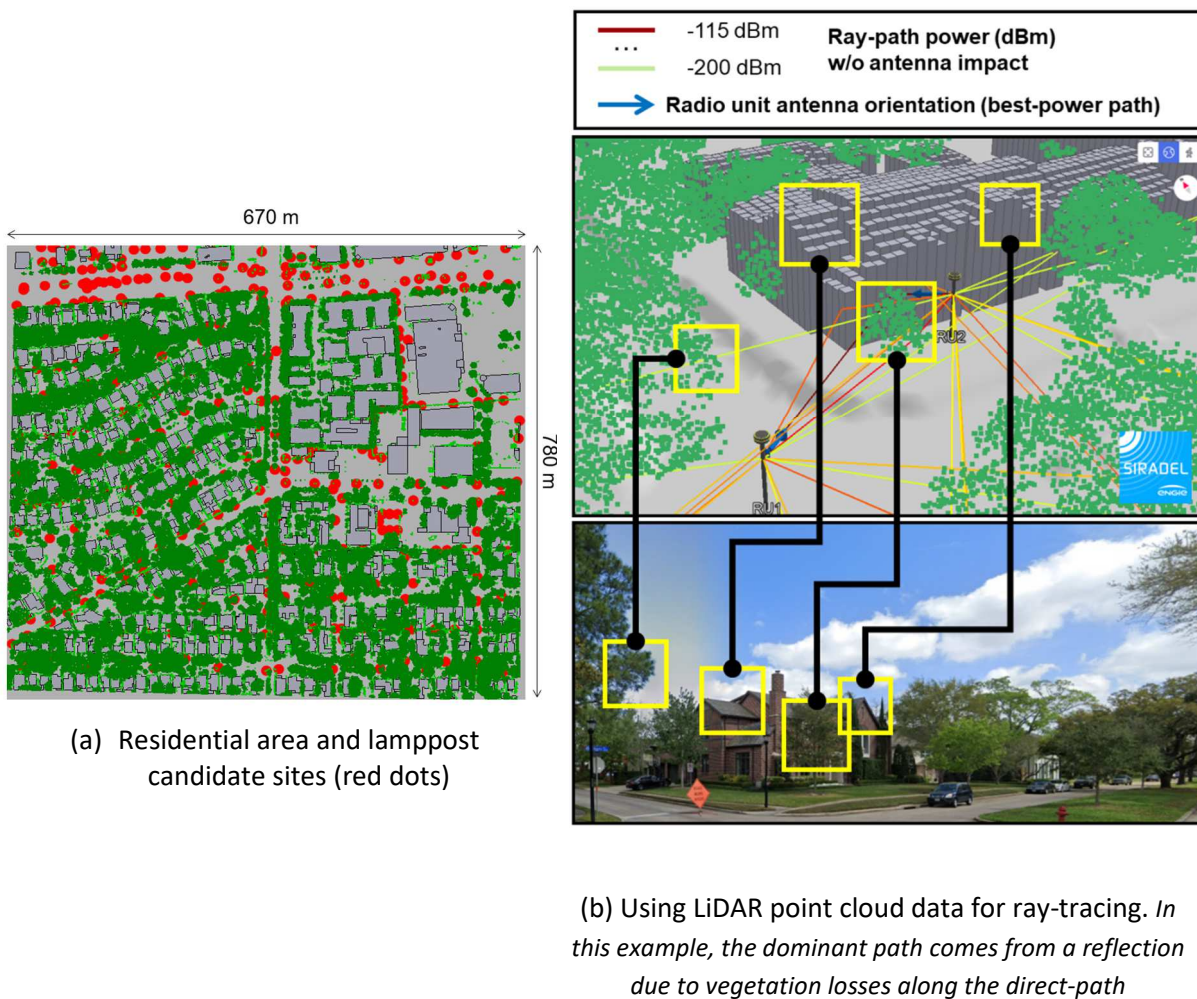


Figure 3 : LiDAR inputs and explorations.

2.1.2.3 System model

The link budget parameters for backhaul and access layers are given respectively in Table 1. BUs are supposed to have a directive high-gain antenna that may be perfectly aligned for a specific fixed radio link. The considered 32 dBi gain has been inspired by the beamforming hardware equipment demonstrated in [10]. The AP antenna is assumed to have lower gain because dynamic beam alignment is required, thus a larger beam is appropriate. The CPE is viewed as a simple low-cost device with limited performance i.e. low beamforming gain.

For simplification purposes, we have assumed that interferences could be neglected with beamforming antennas and we have considered a single-polarization system, with no spatial multiplexing. As discussed later, this rule disadvantages 5G in the forthcoming comparison as its capacity would have been significantly improved with multi-user multiplexing. However, it was preferred to have similar assumptions over all compared scenarios, and focus our analysis on factors that we know our tool can predict properly, i.e. impact of the propagation losses, phase noise and link budget.

We made the additional assumption that with beamforming antennas, interferences may be neglected.

The radio links at 150 GHz are supposed to suffer from medium-level phase noise [12] and therefore employs the BRAVE proposed polar-QAM modulation (P-QAM). Besides, the phase noise is neglected

at 3.5 GHz and 26 GHz; hence, a conventional QAM modulation scheme is considered at those frequencies.

The D-band spectrum is divided into several channels of width 1 GHz, with channel bonding possibilities, in order to satisfy the DAC/ADC constraints. The TDD with a DL/UL ratio of 3:1 is applied to all layers and frequencies.

The CPE coverage from the above-described system is computed by simulating the downlink received power and SNR at all pixels along the building facades. The SNR is mapped to an achievable user throughput; the mapping table has been derived from published link-level simulations [9] [13] and takes 36% overhead into account due to signaling and effective bandwidth usage. Then, a house is determined as eligible to FWA service if the throughput target in Table 2 is reached for at least one pixel along its façade.

The AP capacity is analyzed in a second step. As for a practical dimensioning exercise, it is assumed that only a portion of the eligible houses within the study area does subscribe to the ISP service. A subscription ratio of 50% has been set. And the average traffic load for each AP is estimated as follows:

$$TL_i = \frac{\gamma_s}{\gamma_{DL}} \cdot \sum_{k \in B_i} \frac{Th_c}{Th_k}$$

where

- TL_i : Average downlink traffic load for AP i , assuming a single allocated channel;
- B_i : Set of eligible customer buildings attached to AP i ;
- Th_k : Predicted peak downlink throughput to building k (Mbps);
- Th_c : Demanded downlink throughput by an average customer (Mbps);
- γ_s : Subscription ratio (50%);
- γ_{DL} : DL occupation ratio (75%).

In case of an access network that operates on a single channel (as considered at 3.5 GHz), the calculated traffic load must be kept below 1 (actually, we could have considered a margin on the traffic load, but this was neglected due to the many other margin already involved in the link budget). If above 1, the access network must be densified to improve the radio conditions or reduce the number of customer houses per cell.

In case several channels may be allocated to the AP (as allowed by channel bonding in D-band), the calculated traffic load is converted into a required number of bonded channels. This number is the inverse of the traffic load, rounded to the next higher integer. It is specifically calculated for each AP.

As for the access layer, the SNR and effective throughput is calculated on each backhaul link.

The predicted traffic on each AP is then supposed to be transported through the backhaul links up to the closest fiber PoP in terms of hops. The aggregated demand on each backhaul link is compared to the link's throughput. A traffic load is calculated to detect any bottleneck issue (at 28 GHz), or to evaluate the number of bonded channels needed to satisfy demand (at 150 GHz).

$$TL_m = \frac{(1 + \gamma_{BO})}{\gamma_{DL}} \cdot \sum_{i \in A_m} \frac{Th_i}{Th_m}$$

where

- TL_m : Average downlink traffic load for backhaul link m , assuming a single allocated channel;
- A_m : Set of APs using the backhaul link m ;
- Th_m : Predicted peak throughput on backhaul link m (Mbps);
- Th_i : Demanded downlink throughput from AP i (Mbps);

- γ_{DL} : DL occupation ratio (75%);
- γ_{BO} : Additional backhaul overhead due to the transport protocol and X2 layer (15%).

2.1.2.4 Scenarios

We simulated and compared different deployment scenarios. For all of them, the CPE device is supposed to be installed on the house external wall or window, with its antenna beam pointing towards the best AP. The average downlink demand by a CPE is 150 Mbps. The APs and DUs are positioned at existing lampposts or poles, or are co-sited with a PoP. The wireless backhaul is connected to four PoPs distributed into the 0.52 km² study area. The PoP capacity is assumed to be greater than FWA demand. Network devices have been set-up using the link budget and deployment parameters presented in Table 2. We implemented four different scenarios:

- 1) *Baseline scenario at 150 GHz*: the CPE has a low-cost large-beamwidth antenna with only 5 dBi gain; the APs and DUs are installed at height 4 m above ground. The transmit power at all radio devices is limited to 100 mW for practical considerations.
- 2) *Greater CPE gain*: same as the baseline scenario, except that CPE has greater performance with 12 dBi gain.
- 3) *Greater node height*: same as the baseline scenario, except that the APs and DUs are installed at height 6 m above ground.
- 4) *5G frequencies*: same deployment configuration as the baseline scenario, but
 - a. At lower frequencies: access at 3.5 GHz, and backhaul at 28 GHz;
 - b. With specific link budget parameters: greater transmit powers, and lower beamforming antenna gains;
 - c. With highly reduced signal bandwidths: typical 100 MHz channel bandwidth for the access at 3.5 GHz; maximum allowed channel bandwidth of 800 MHz for the backhaul at 26 GHz.

Although the detailed link budgets differ between the 150-GHz and 5G FWA networks, the maximum allowed path loss (MAPL) remain of a similar order (see MAPL rows in Table 1). Hence the main factor that explains the evolution of the network coverage between 5G and sub-THz frequencies is the radio propagation.

We also evaluated how the PoP spatial distribution affects the network performance. For this purpose, the baseline scenario has been duplicated into four sub-scenarios 1.1, 1.2, 1.3 and 1.4, with the different PoP schemes shown in Fig. 4. A specific network design was realized for each sub-scenario to assess how the PoP selection influences the size of the wireless infrastructure.

Remark the study is realized in a residential scenario with high vegetation density, which is quite a challenge for D-band propagation. This situation is actually well representative of the FWA networks currently deployed with 5G technology.

| Scenario | 1) Baseline 150 GHz | 2) Greater CPE gain | 3) Greater node height | 4) 5G frequencies |
|--------------------------------------|---------------------|---------------------|------------------------------|-------------------|
| Carrier | 150 GHz | | | 28 GHz |
| Channel bandwidth | 1 GHz | | | 0.8 GHz |
| Number of channels | Free | | | 1 |
| Tx power | 100 mW (20 dBm) | | | 1 kW (30 dBm) |
| Tx antenna gain * | 32 dBi | | | 25.5 dBi |
| Rx antenna gain * | 32 dBi | | | 25.5 dBi |
| Rx noise figure | 8 dB | | | 8 dB |
| Phase noise | Medium | | | Low |
| Implementation loss | 3 dB | | | 3 dB |
| Modulation scheme | Polar-QAM | | | QAM |
| SNR – Thrgt mapping | [6] | | | [12] |
| Target throughput per channel | ≥ 1024 Mbps | | | ≥ 1024 Mbps |
| Min. required SNR | 5.9 dB | | | 5.0 dB |
| Location coverage perc. | 99% | | | 99% |
| Error margin | 14.0 dB | | | 14.0 dB |
| MAPL ** | 135.6 dB | | | 135.5 dB |
| Carrier | 150 GHz | | | 3.5 GHz |
| Channel bandwidth | 1 GHz | | | 100 MHz |
| Number of channels | Free | | | 1 |
| AP Tx power | 100 mW (20 dBm) | | | 1 kW (30 dBm) |
| AP antenna gain * | 28 dBi | | | 20 dBi |
| CPE antenna gain * | 5 dBi | 12 dBi | 5 dBi | 5 dBi |
| CPE noise figure | 10 dB | | | 10 dB |
| Phase noise | Medium | | | Low |
| Implementation loss | 3 dB | | | 3 dB |
| Modulation scheme | Polar-QAM | | | QAM |
| SNR – Thrgt mapping | [6] | | | [12] |
| Target throughput per channel | ≥ 384 Mbps | | | ≥ 384 Mbps |
| Min. required SNR | -0.8 dB | | | 13.5 dB |
| Location coverage perc. | 95% | | | 95% |
| Error margin | 9.9 dB | | | 9.9 dB |
| MAPL ** | 112.9 dB | 119.9 dB | 112.9 dB | 112.6 dB |
| Rainfall rate | 12 mm/h | | | |
| Number of PoPs | | | 4 | |
| Nodes height | 4 m | 4 m | 6 m | 4 m |
| Node position | | | Lampposts | |
| DUs per node | | | Free | |
| Number of hops | | | Free | |
| CPE height | | | 3.5 m | |
| CPE position | | | Installed against the façade | |

* The maximum antenna gain includes the beamforming effect

** MAPL = Maximum allowed Path Loss

Table 1 : Radio parameters per scenario.

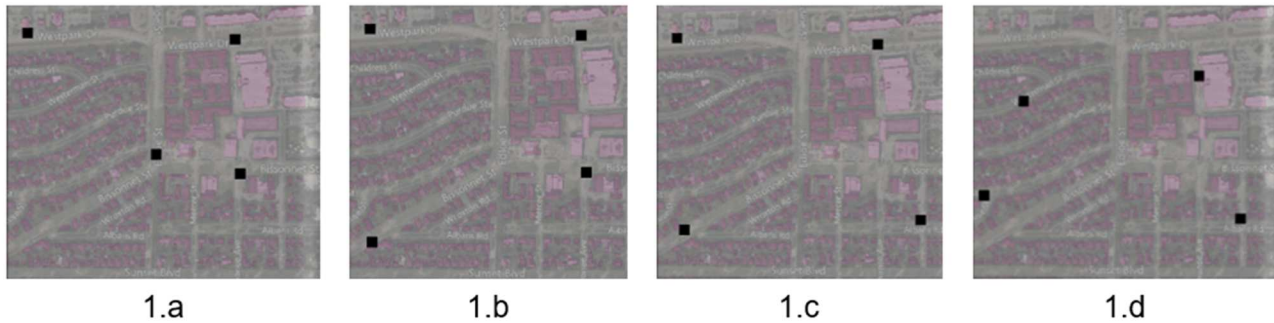


Figure 4 : Different PoP spatial distributions (black squares) tested with the baseline scenario.

2.1.2.5 Optimization

The AP and backhaul node positions are selected from an automated algorithm that aims at reaching the eligibility coverage target and the required capacity with minimum number of deployed antennas. We used a greedy algorithm that iteratively makes a decision. At each iteration it picks the best candidate AP site among those whose coverage overlaps with at least one AP site already selected.

Usual coverage targets are 80%, 90%, 95%, etc. But a preliminary study has shown how difficult it is for the baseline scenario to reach such a coverage level. The lack of appropriate pole candidates and/or the high obstruction losses prevents from reaching some of the remote densely vegetated areas. Only 13% of the backhaul links of length lower than 250 m are in line-of-sight (LoS); therefore, the possibilities for medium- or long-range backhaul links are limited. The number of required hops and relays does rapidly grow when searching for a quasi-full coverage.

By consequence, the case study was conducted with a more reasonable coverage target, i.e. 55%. This means that 55% houses must be eligible to FWA service. The selected APs and backhaul links have to support the throughput demand from the customers who are expected to subscribe the service, i.e. half of the eligible houses.

2.1.3 Simulation results

The resulting network design for the baseline 150 GHz scenario is made up of 34 FWA AP sites, 9 additional backhaul relay sites, and 39 point-to-point backhaul links (equivalent to 78 DUS) as illustrated in Fig. 5 and Fig. 6. On those figures, we show the downlink achievable throughput (per 1 GHz channel) at the CPE possible locations; this corresponds to the colored pixels along the building façades. Buildings surrounded by black pixels are not eligible. The colors associated to the APs (red dots) and backhaul links (solid lines) indicate the number of required channels to resp. serve the CPEs of a cell or transport the aggregated user data streams. Maximum 3 channels are needed for a AP; and maximum 5 channels for a backhaul link.



Figure 5 : Network design and performance for scenario 1 (baseline).



Figure 6 : Zoom on the network designed for scenario 1 (baseline).

Results for all four scenarios are summarized in Table 2 and Fig. 6. Obtained networks for scenarios 2 and 4 are illustrated by resp. Fig. 8 and Fig. 9. The improvement of the CPE gain from 5 dBi to 12 dBi allows to reduce the site numbers by 51% and number of radio devices (APs and DUs) by 49%. Remark any gain of 7 dB in the access link budget would give same result, i.e. an infrastructure with size divided by 2. Greater node's height (from 4 to 6 m) leads to a smaller infrastructure in terms of sites, but the overall benefit is not obvious. On one hand, the number of backhaul links is reduced by 8% as some propagation paths may travel above trees. But on the other hand, the number of APs has to be increased by 15% because the propagation from the AP to the façade CPEs (still at height 2.5 m) is slightly degraded due to additional vegetation losses. This study shows that the effect of the node's height is not homogeneous and cannot be easily anticipated; however, this also demonstrate there is an interest for smart radio-planning tools that would be able to optimize the height of each individual radio device.

Finally, the comparison between the baseline 150 GHz scenario and the deployment at 5G frequencies leads to interesting observations. The façade pixel colors in Fig. 9 clearly illustrate that 100% coverage is reached with the 3.5 GHz access network, even in areas with low AP density. Actually the deployment of 4 APs at the PoP position would even be sufficient to achieve a wide coverage (91%). The reason why the 3.5 GHz access network has been densified is that the capacity of each AP is strongly limited due to the 100 MHz bandwidth; therefore, the optimization algorithm has dimensioned an AP deployment (and the required transport infrastructure) such that the number of subscribers per cell is compatible with this capacity. In the end, the number of APs and backhaul links is multiplied by 2.5 compared to the baseline 150 GHz scenario. In reality, such a 5G infrastructure has no chance to be deployed due to the cost and the imbalance between coverage and capacity. The target average throughput per subscriber would be set at a much lower value. The access capacity could be also boosted thanks to multi-user multiplexing (from a massive MIMO system). Nevertheless, by assuming constant multiplexing capabilities and constant throughput target, the current study does illustrate how the ultra-large bandwidth available in D-band can more than compensate for the additional propagation losses, and therefore is a possible alternative to 5G frequencies in perspective of high data rate FWA networks.

| Scenario | Total #sites | Access | | | Backhaul | | | | Median #hops | Max #hops |
|------------------------|--------------|--------|------------------|---------------|--------------|------|------------------|---------------|--------------|-----------|
| | | #APs | Median #channels | Max #channels | #Relay sites | #DUs | Median #channels | Max #channels | | |
| 1) Baseline 150 GHz | 43 | 34 | 2 | 3 | 9 | 78 | 1 | 5 | 2 | 7 |
| 2) Greater CPE gain | 21 | 19 | 2 | 4 | 2 | 38 | 2 | 7 | 2 | 7 |
| 3) Greater node height | 40 | 39 | 1 | 3 | 1 | 72 | 1 | 5 | 2 | 8 |
| 4) 5G frequencies | 97 | 88 | 1 | 2 | 9 | 198 | 1 | 2 | 3 | 6 |

Table 2 : Per scenario results.

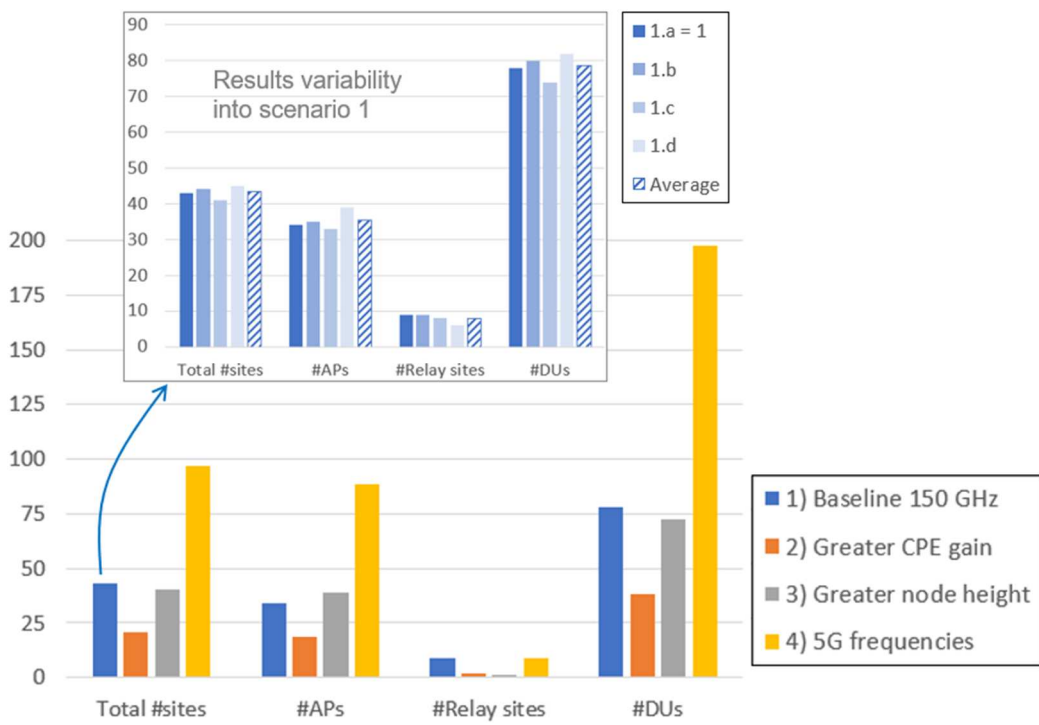


Figure 7 : Size of the designed network's infrastructure for scenarios 1 to 4; and analysis of the results variability due to the PoP spatial distribution in scenario 1.



Figure 8 : Network design and performance for scenario 2 (greater CPE gain).

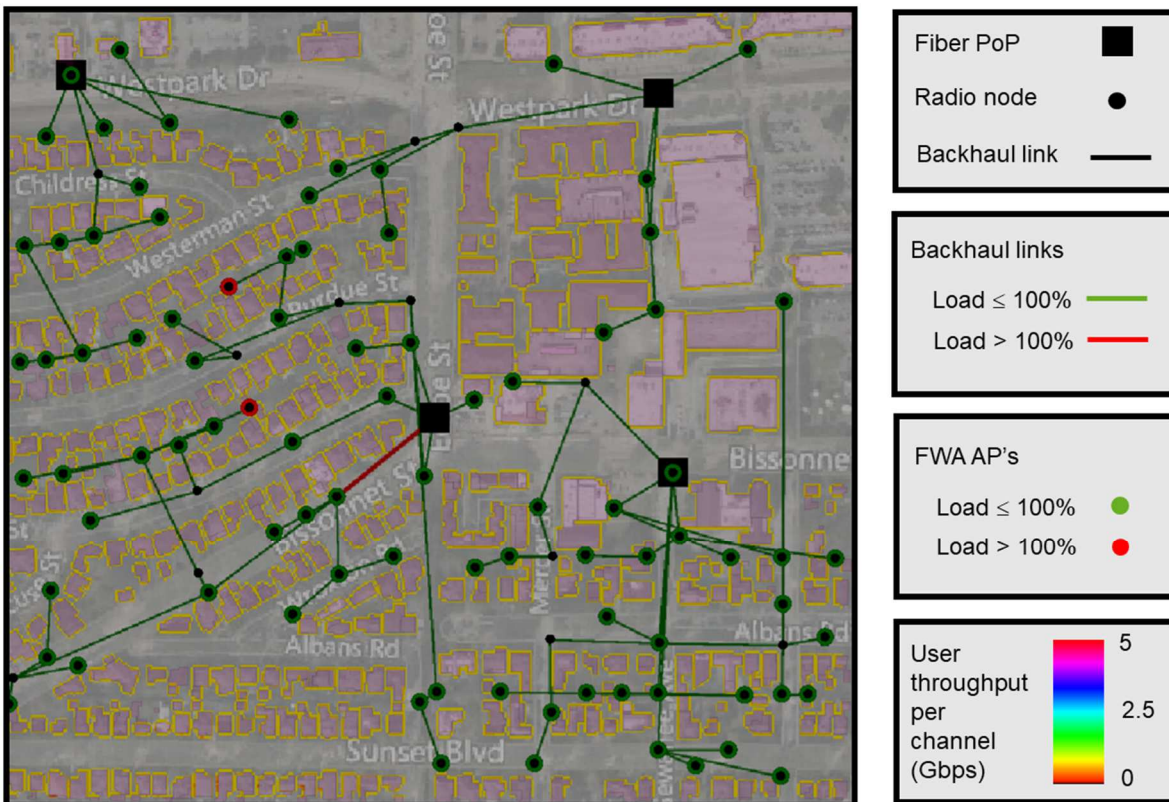


Figure 9 : Network design and performance for scenario 4 (5G frequencies).

Four different PoP distributions have been tested in sub-scenarios 1.a to 1.d. The impact on the network infrastructure is given in Table 3 and illustrated in Fig. 8. There is some variability but limited to 6% standard deviation regarding the number sites, APs or DUs. (Standard deviation percent is higher for the number of relays, but this may be caused by the smaller average value). We may draw two conclusions:

- Sensibility of the network size to the PoP distribution scheme is limited to a few percent standard deviation, therefore the chosen PoP distribution for scenarios 1 to 4 (= PoPs in scenario 1.a) is likely not changing the main observations made on CPE gain, node height or frequencies impact.
- The impact on the maximum number of hops might be important as pointed out in particular in scenario 1.d. Sensibility of the network size and of the backhaul KPIs seem strong enough to justify the introduction of automated PoP selection in the optimization algorithm. This might be considered in future research work.

| Scenario | Total #sites | Access | | | Backhaul | | | | Median #hops | Max #hops |
|----------|--------------|--------|------------------|---------------|--------------|------|------------------|---------------|--------------|-----------|
| | | #APs | Median #channels | Max #channels | #Relay sites | #Dus | Median #channels | Max #channels | | |
| 1.a) | 43 | 34 | 2 | 3 | 9 | 78 | 1 | 5 | 2 | 7 |
| 1.b) | 44 | 35 | 2 | 3 | 9 | 80 | 1 | 6 | 3 | 10 |
| 1.c) | 41 | 33 | 2 | 3 | 8 | 74 | 1 | 23 | 4 | 13 |
| 1.d) | 45 | 39 | 1 | 3 | 6 | 82 | 2 | 6 | 4 | 11 |
| Average | 43.3 | 35.3 | 1.8 | 3.0 | 8.0 | 78.5 | 1.3 | 10.0 | 3.3 | 10.3 |
| Std dev. | 3% | 6% | 25% | 0% | 15% | 4% | 35% | 75% | 26% | 21% |

Table 3 : Impact of the PoP spatial distribution.

2.1.4 Conclusion

This case study allowed us to quantify the size of the needed sub-THz infrastructure for a realistic FWA deployment scenario into a residential environment, which is a typical target of today's 5G FWA operators. Of course, the considered downlink throughput (150 Mbps average per subscriber) is significantly higher than experienced in 5G commercial networks, thanks to the huge available bandwidth (between 1 to 7 channels of 1 GHz have been allocated to the predicted sub-THz devices).

The comparison between various scenarios has highlighted the effect of the CPE antenna gain (infrastructure divided by 2 for an additional gain of 7 dB), the height of the radio nodes (complex), the frequency and bandwidth.

Finally, it has been demonstrated three important results:

1. A FWA network with higher data rates than possible today looks feasible based on 150 GHz devices, even if the transmit power is limited to 100 mW, but assuming antenna gains up to 32 dBi. This must of course be further validated and refined in the future, with real sub-THz radio measurements and effective equipment performance.
2. A full coverage target may be very costly at such high frequency. Thus, it looks like a better approach to design the D-band network for a reasonable coverage objective, and then complement with additional connections in a lower frequency band. The opposite procedure may also be implemented, where an existing full-coverage 5G network is upgraded with D-band devices to locally boost the capacity for the backhaul and/or access layer.
3. Smart radio-planning tools with capability to jointly optimize the access and backhaul layer can be appropriately applied to design a dense high-frequency FWA network, thanks to detailed geographical data and a dedicated optimization algorithm. Radio planning at those frequencies is a critical and complex task, therefore such a tool is thought to be mandatory for future sub-THz operators.

2.2 Scenario #2: Wireless backhaul in a large venue (shopping mall)

The presented case study is based on demonstrator #3 described in [5], using the backhaul network design functionalities and P-QAM modulation.

The considered scenario is a shopping-mall area with strong required capacity for mobile and fixed wireless connectivity.

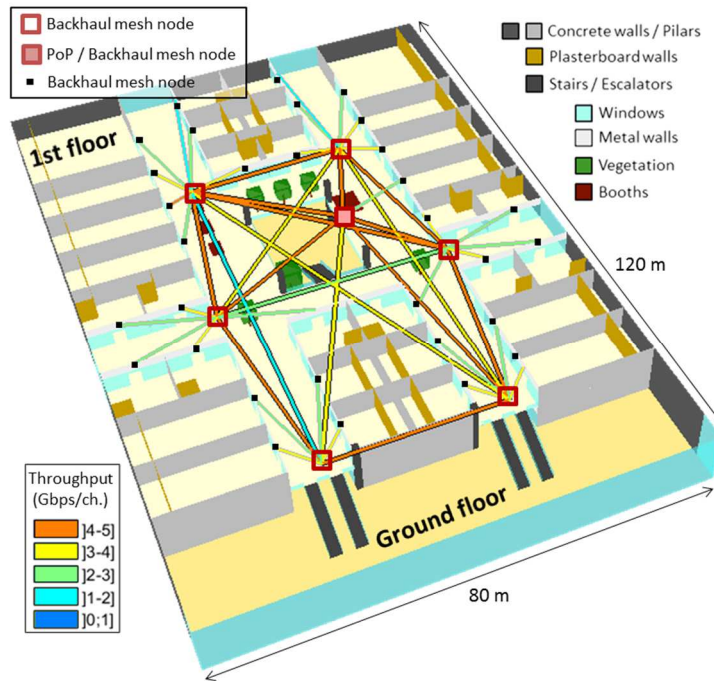


Figure 10: Backhaul deployment in the shopping mall scenario.

2.2.1 Introduction

The sub-THz transport network can be deployed as a complement to the optical fiber inside large venues, e.g., airports, railway stations, stadium, campus, or commercial halls. While the optical fiber is distributing strong capacity in the different blocks of the venue, the wireless mesh backhaul may be the final link to some fixed, portable or even mobile (e.g., flying) access points. If combined with efficient auto-alignment and dynamic routing algorithms, the sub-THz transport layer can adapt to changes e.g., related to densification, maintenance, event, or construction works.

The strong obstruction losses oblige the sub-THz hops to be deployed in a clear space, typically in large rooms or open areas, above most furniture and bodies. Fiber relays can be used to extend the network coverage to another room.

2.2.2 Models and assumptions

The evaluation study is carried out in a model of commercial hall. Figure 10 shows the two-floor 120m×80m building, which is composed of a large entrance area, large alleys with few obstacles (booths, vegetation, and pillars), and a succession of shops. Each floor is five meters high. A mesh sub-THz network has been designed to feed the wireless access points located at the first floor and entrance area. Two different kinds of access points are considered: those inside the shops, which require a sub-THz relay to be positioned on the outer surface of the shop window; and those connected to a portable/mobile sub-THz relay installed outside the shops.

The sub-THz backhaul network is composed of mesh nodes at height 4 meters, i.e. below the cables, pipes or lights installed below the roof, but above most ground obstacles; one of those nodes is directly connected to a fiber Point of Presence (PoP). The following kinds of radio link are evaluated: 1) node

to node; 2) node to the fixed shop relays at height 4 meters; 3) node to any portable/mobile relays at height 2 meters. The sub-THz system parameters are given in Table 4. The propagation model is enabling a maximum of 2 reflections and 1 diffraction along each ray path. Reflections on the ceiling or floor surfaces are not allowed as they are likely to be obstructed. Shop windows are assumed as opaque surfaces for considered frequency.

Table 4: Considered link budget in the shopping mall scenario.

| Parameter | Indoor node-to-node | Indoor node-to-relay (DL) |
|-----------------|---------------------|---------------------------|
| Frequency band | 150 GHz | |
| Signal BW | 1 GHz | |
| Tx power/ch. | 0.1 W | 0.1 W |
| Tx antenna | 25.0 dBi | |
| Rx antenna | 25.0 dBi | 8.0 dBi |
| Th. noise floor | -84.0 dBm | |
| Noise figure | 10.0 dB | |
| Rx sensibility | -98.2 dBm | -81.2 dBm |
| Implement. loss | 3.0 dB | |
| Rain | N/A | |
| Adj. factor | [−5;+5] dB | |

2.2.3 Simulation results

The obtained backhaul network is composed of 6 nodes.

The peak throughput on each radio link is predicted in two different ways: either the antennas are aligned on the direct-path or aligned on the strongest propagation path. Figure 10 shows the latest calculated throughput for all mesh connections and the best shop-relay connections. Every mesh node is linked to the PoP with maximum two hops having a peak throughput greater than 4 Gbps/channel. All shop-relays are attached to the mesh network with more than 2 Gbps/channel peak throughput.

Link diversity is a critical factor for reliability of such a network in order to optimize routing, to minimize interference, but also to combat temporary blockage on the best propagation path. In this study, the link diversity has been characterized by counting the average number of available connections per node. Figure 10 gives the average number of connections as a function of a target peak throughput, and for both kinds of alignment approaches. As an example, the average number of connections above 1 Gbps/channel at any node of the backhaul network is 5.1, when the system aligns on the strongest path. Some improvement is observed when comparing the strongest-path alignment to the direct-path alignment; however, the clear direct propagation path is often the dominant component.

The plot in Figure 11 (a) indicates how many different propagation paths can be used by the system (with automatic antenna alignment) to connect a node and reach a given peak throughput level. When aggregating all paths from all neighbor mesh nodes, the average number of potential paths that offer more than 1 Gbps/channel at a mesh node is 123, which might guarantee very good service availability.

Finally, the sensitivity of those results to the considered link budget is illustrated in Figure 11 (b), where the average number of connections is plotted as a function of an adjustment factor in range [-5;+5] dB. The shop-relays reliability is significantly affected by this adjustment factor. The average diversity at 2 Gbps/channel is 1.8 with initial settings; it goes to 3.6 when adding 5dB, and degrades to 1.2 when

removing 5 dB. Besides, thanks to many LoS links and strong reflections, the considered mesh network remains viable with 5dB degradation but still 3.4 connections per node.

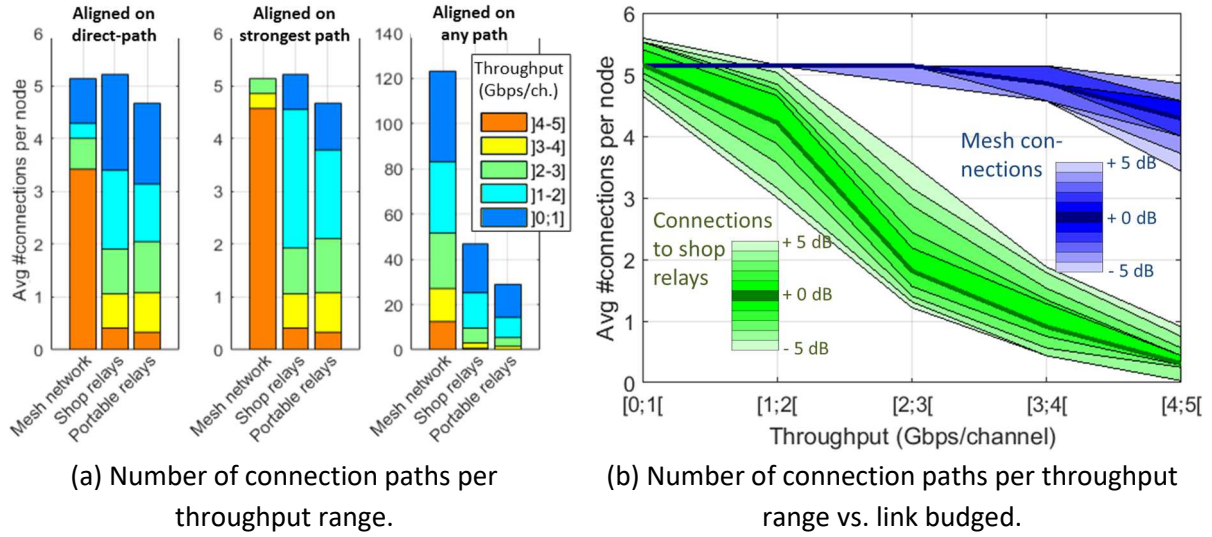


Figure 11: Wireless backhaul performance in the shopping mall scenario.

2.3 Scenario #3: Kiosk and enhanced WLAN in Office environment

Multiple-Input-Multiple-Output (MIMO) technology and mainly Spatial Multiplexing (SMX) is a key enabler for high data rate applications that was combined with high order QAM in recent standards for high data rate. MIMO systems caught significant attention because of their superiority in exploiting spatial resources, improving system capacity, and increasing the Spectral Efficiency (SE). However, increasing the order of QAM modulation in the sub-THz band is limited by the RF impairments (e.g., Phase Noise (PN), low output power, hardware non-linearity,...) [14] [15]. Thus, better exploitation of MIMO technology is required to enable a low power ultra-high data rate system in sub-THz bands while surviving with the Radio Frequency (RF) impairments and sub-THz limitations, and such schemes are presented in [16] [4].

Recalling that the spatial IM domain can provide high SE gain, mainly when it also exploits the multiplexing gain. For instance, Generalized Spatial Modulation (GSM) conveys the information bits in the index of the activated Transmit Antenna Combination (TAC) and in the N_a simultaneously transmitted symbols [17] (see more details in [16]). Note that GSM generalizes several existing schemes such as Space Shift Keying (SSK) [18](and its generalized version GSSK [19]) and also Spatial Modulation (SM) [20]. Since GSM suffers from some performance degradation in highly correlated channels that cannot be completely compensated [21], the Dual-Polarized-GSM (DP-GSM) is proposed to limit the spatial correlation effect while enhancing more the SE by exploiting the polarization IM dimension [22].

On the other side, a promising novel IM domain, named filter IM domain, is proposed in [23] to overcome the drawback of other systems and achieve a higher SE and EE. It is worth highlighting that the proposed filter IM domain generalizes different existing modulation schemes (e.g., OOK, PPM, QAM...) and also the time and frequency IM domains [23]. In addition, the proposed Filter Shape Index

Modulation scheme within this IM domain allowed to achieve high SE and EE in SISO [23] and MIMO [24] while providing different advantages highlighted in [4].

In this section, the different potential MIMO candidates for low-power ultra-high data systems are evaluated in sub-THz environment with PN impairments. Firstly, the study considers the different systems without channel coding, and the most promising candidates is evaluated at the end with channel coding.

The presented case study is based on demonstrator #2 described in [5].

2.3.1 Proposed S-EGSM system

In this subsection, a complete analysis is provided for SMX (spatial multiplexing) and GSM subjected to major sub-THz limitations and RF impairments. This performance analysis includes a comparison with SMX systems in terms of performance, robustness to PN, computational complexity, cost, Peak-to-Average Power Ratio (PAPR), link budget and power consumption. Consider a MIMO Spatial Multiplexing (SMX) system with N_t transmit antennas (TAs) and N_r receive antennas (RAs) where $N_r > N_t$. Different M -ary Amplitude-Phase Modulation (APM) symbols are transmitted simultaneously from the different TAs. GSM system conveys information bits in the signal domain as in SMX system, but additional bits are conveyed in the spatial domain by means of IM [25]. Such GSM system consists of N_t TAs where only N_a TAs are activated at each symbol period to transmit different M -ary APM symbols as depicted in Figure 12. Note that SMX is a special case of GSM system where all TAs are activated, and the spatial domain does not convey any information bits. The maximum-likelihood (ML) detector for SMX is able to detect all the N_t transmitted APM symbols by an exhaustive search over all possible transmit vectors. We are considering the ML detection for a fair comparison between the GSM and the SMX systems with optimal performance. Sub-THz bands suffer from many RF challenges, especially for low-cost implementation, and the main limitations are: low achievable transmit output power, non-linearity effect of the PA and its limited efficiency, phase noise of the LO that leads to significant degradation limits both the Bit-Error Rate (BER) performance and throughput rate. It is well known that practical oscillator can never generate a pure sinusoid and the PN increases with the carrier frequency. Thus, the sub-THz communication system should be analysed under this impairment since neglecting its impact is no more tolerable as in sub-GHz systems.

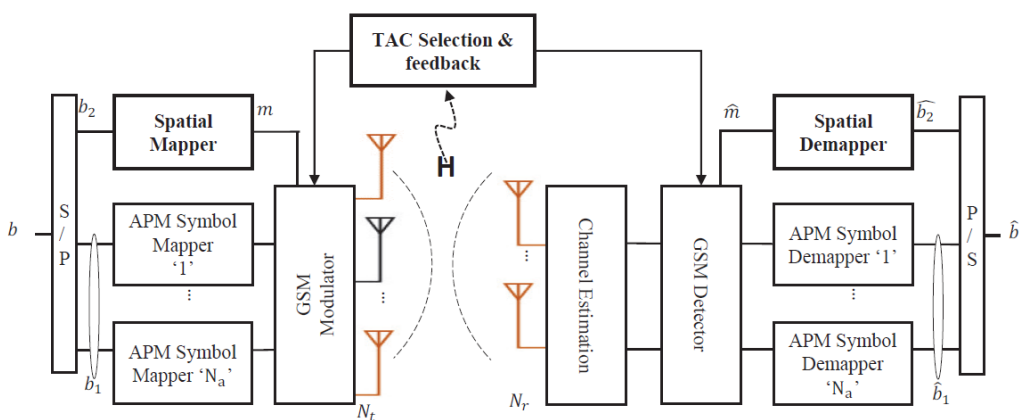


Figure 12: System model of S-Enhanced GSM (S-EGSM) [21].

The received baseband vector of an equivalent $N_r \times N_t$ MIMO system with phase noise can be expressed as:

$$\tilde{y} = \Phi_r H \Phi_t x + n$$

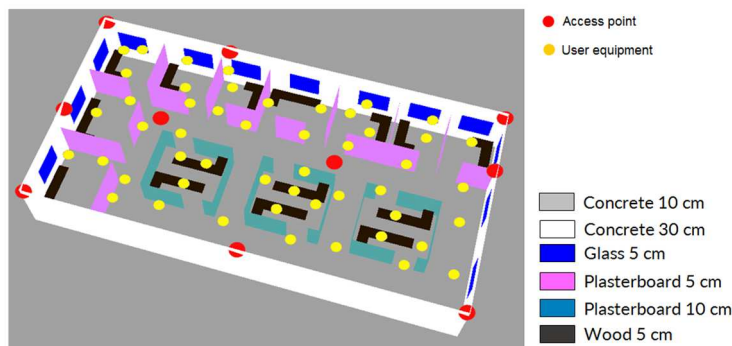
where Φ_t and Φ_r are the $N_t \times N_t$ and $N_r \times N_r$ diagonal matrices of phase noise from the transmitter and receiver oscillators respectively. These phase noise matrices can be represented as follows:

$$\Phi_t = \text{diag} \left(\left[e^{j\theta_1^{Tx}}, \dots, e^{j\theta_{N_t}^{Tx}} \right]^T \right)$$

$$\Phi_r = \text{diag} \left(\left[e^{j\theta_1^{Rx}}, \dots, e^{j\theta_{N_r}^{Rx}} \right]^T \right)$$

where θ_i^{Tx} and θ_j^{Rx} represent the PNs at the i^{th} Transmit Antenna (TA) and j^{th} Receive Antenna (RA) respectively that can be described in sub-THz band by a truncated Gaussian distribution $\mathcal{N}(0, \sigma_g^2)$ with zero-mean and variance σ_g^2 like SISO PN model described in [26]. In the Distributed Oscillator (DO) setup, $\theta_i^{Tx} \neq \theta_j^{Tx}$ and $\theta_i^{Rx} \neq \theta_j^{Rx}$ for all $i \neq j$.

A ray-based deterministic channel modelling for sub-THz Band (mainly between 90-200 GHz) is presented in [27]. The propagation channel model in [27] considers the material properties, gas attenuation and the impact of furniture that leads to more obstructions along the propagation paths and new scattered paths. In addition, it characterizes the main channel properties such as path loss and delay spread for LOS, NLOS with vegetation and NLOS cases for indoor in-office and outdoor in-street scenarios. In the following, we will focus on the downlink hotspot (or kiosk, scenario #5) indoor scenario where the Access Points (AP), acting as transmitters, and the user equipment (UE), acting as receivers without mobility, are equipped with N_t and N_r isotropic antennas respectively in the positions depicted in Figure 13. Therefore, the MIMO propagation channels are obtained using the simulator for ray-based deterministic channel modelling (see details on the office Sub-THz channel propagation in Chapter 1 of [16]). The MIMO channels are obtained with different array geometry such as Uniform-Linear-Array (ULA) and Uniform-Rectangular-Array (URA). Note that an antenna elements separation of 4λ , where λ is the wavelength, is considered to reduce the effect of spatial correlation, and thus enhance MIMO communication.



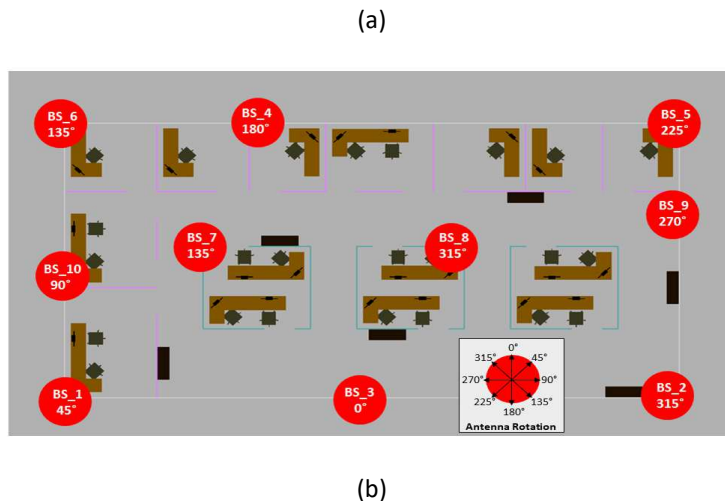


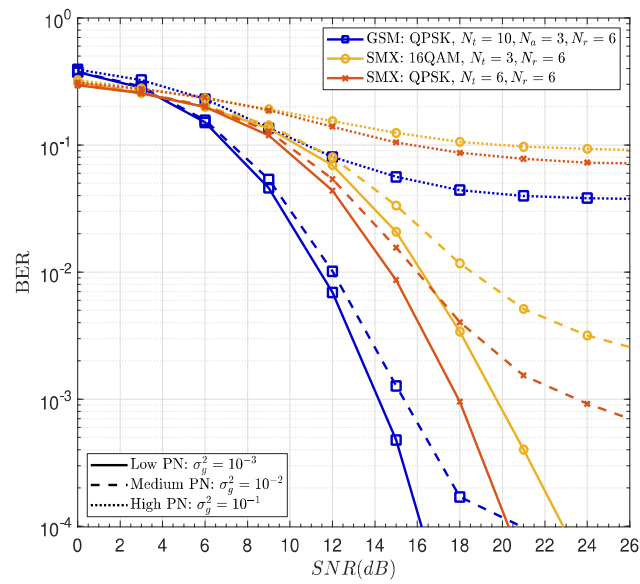
Figure 13: Indoor MIMO channel measurements [27] . (a) 3D physical positions of 10 APs marked in red circles and 50 UEs marked in yellow. (b) 2D positions of the 10 APs.

2.3.1.1 Performance under realistic MIMO sub-THz channel and PN impairment

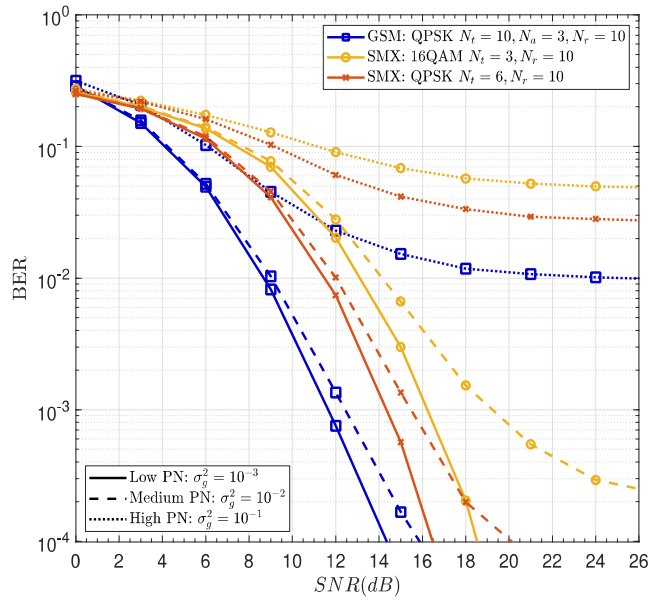
The performance of the MIMO SMX and S-EGSM proposed in [21] (GSM terminology is used hereafter) is studied in sub-THz environment with RF impairments. Firstly, we will show the impact of PN in Distributed Oscillator (DO) setup over MIMO sub-THz channels on both GSM and SMX systems for an indoor (office scenario) ultra-high data rate scenario. The system comparison is performed with different PN levels (low $\sigma_g^2 = 0.001$, medium $\sigma_g^2 = 0.01$, high $\sigma_g^2 = 0.1$) without applying any phase noise mitigation technique. In our comparison, we consider the sub-THz indoor MIMO channels with a separation distance between MS and AP going from 2 to 8m, i.e., an average distance of 5m. For a fair comparison, both systems GSM and SMX are compared under the same spectral efficiency, which requires either the same modulation schemes with SMX and GSM or the same number of activated TAs. We cannot conserve the same values for both variables because SMX needs to accommodate the virtual bits conveyed in GSM by increasing one of these parameters. The optimal ML detection is used along with the same number of RAs N_r . In the following, we will consider different systems with 12 bits per channel use (bpcu): QPSK-GSM with $N_t = 10$ and $N_a = 3$ QPSK-SMX with $N_t = 6$ and 16QAM-SMX with $N_t = 3$. Note that QPSK with GSM is considered among the existing conventional modulations since it showed a significant performance gain and has lower PAPR compared to other modulations (PAM, high order QAM or (D)PSK) [28].

Figure 14 shows clearly that QPSK-GSM outperforms SMX subjected to any PN level. For example, a gain of 4 dB is obtained using QPSK-GSM as compared to QPSK-SMX system, and which goes to 6.8 dB when compared to 16QAM-SMX with $N_r = 6$ at low PN as shown in Figure 14a. However, these values of gain are respectively reduced to 2 and 4.2 dB when $N_r = 10$ as shown in Figure 14b. Note that QPSK-SMX in sub-THz channels performs better than 16QAM-SMX for same spectral efficiency in all cases. Moreover, the performance gain of QPSK-GSM is much higher at medium PN when compared with QPSK-SMX, and it becomes more advantageous when compared to 16QAM-SMX, where we notice that the high M -ary QAM schemes are very sensitive to PN. Thus, GSM is more robust to PN since the amount of information being conveyed and contained in the phase of the complex symbols (QPSK or QAM) is less as compared to SMX of same SE, while a part of this information is conveyed through the virtual bits (less sensitive to the PN effect). Note that both systems, without phase noise mitigation

techniques, suffer from a high error floor when subjected to strong PN in sub-THz channels. The simulation results with Uniform-Rectangular-Array (URA) geometry are shown in Figure 15, where similar conclusion on the obtained gain can be drawn with the difference that all systems require a slightly larger SNR due to higher spatial correlation between antennas. Therefore, GSM can survive at low to medium PN in sub-THz channel, but more research is required to enhance GSM performance with strong PN channel. It is worth mentioning that the performance can be enhanced in PN channel by using PN robust modulations and powerful channel coding technique as highlighted at the end of this section.



(a)



(b)

Figure 14: BER performance of 12bpcu MIMO SMX and GSM systems subjected to different phase noise levels in DO setup. AP-MS mean distance is dmean = 5m. ULA array geometry with 4 λ antenna separation is used with (a) Nr = 6, (b) Nr = 10.

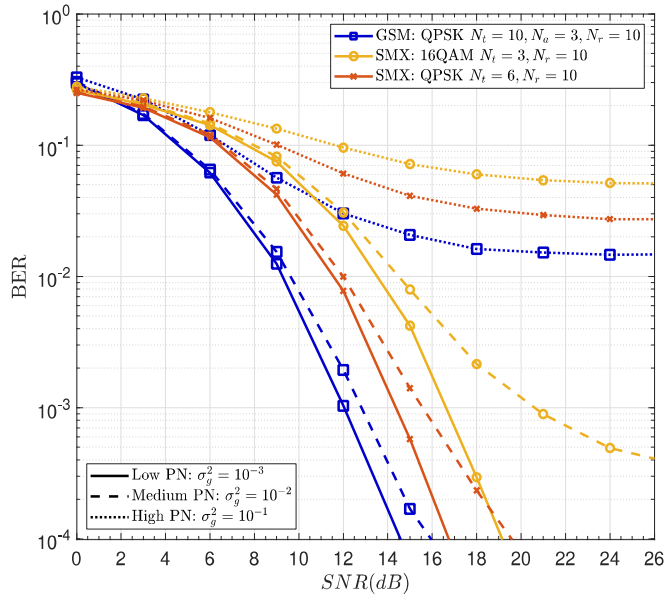


Figure 15: BER performance of 12bpcu MIMO SMX and GSM systems subjected to different phase noise levels in DO setup. AP-MS mean distance is dmean = 5m. URA array geometry with 4 λ antenna separation is used with Nr = 10.

2.3.1.2 ML Computational Complexity

In this subsection, SMX and GSM receivers are compared from the optimal detection complexity point of view. The ML complexity is measured by the number of real multiplications performed ; the hardware complexity of the addition is negligible compared to the multiplications. The number of Euclidean distances being calculated in the ML detector for SMX is $M^{N_t} = 2^{\mathcal{L}_{SMX}}$ while it is $N_{TAC}M^{N_a} = 2^{\mathcal{L}_{GSM}}$ for GSM. The total ML detector complexity for SMX and GSM in terms of real multiplications can be expressed as:

$$\begin{aligned} C_{SMX} &= 2^{\mathcal{L}_{SMX}+1}(2N_t + 1)N_r \\ C_{GSM} &= 2^{\mathcal{L}_{GSM}+1}(2N_a + 1)N_r. \end{aligned}$$

It is clear that GSM and SMX have same detector computational complexity when they have same system spectral efficiency $\mathcal{L}_{SMX} = \mathcal{L}_{GSM}$, same number of activated TAs and RAs but with higher modulation order in SMX system. However, SMX suffers from higher computational complexity when the number of activated TAs in SMX $N_t > N_a$ is increased to maintain the same efficiency and modulation order as GSM for a better robustness to PN using low modulation order. The complexity of SMX in both configurations compared to GSM with same spectral efficiency (12bpcu) is illustrated in Figure 16, where MIMO QPSK-SMX is 1.86 times more complex than QPSK-GSM.

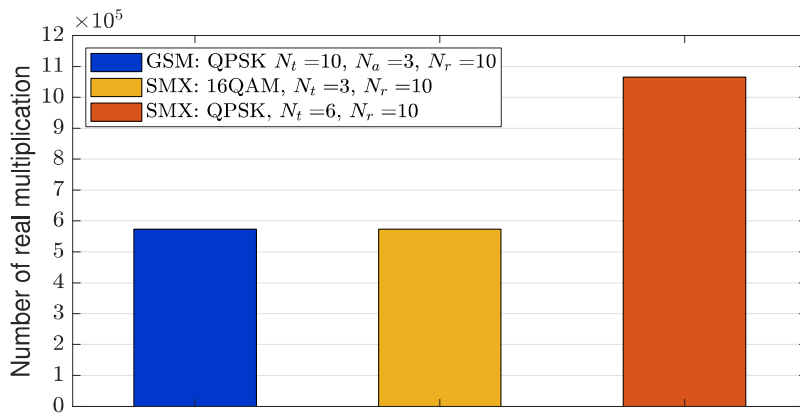


Figure 16: ML detector computational complexity for GSM and SMX with same spectral efficiency 12bpcu.

2.3.1.3 Discussion

In this sub-section, we will complete our analysis by considering other important factors for sub-THz communication. MIMO systems in sub-THz bands require using low order modulation schemes as QPSK for two reasons: 1) higher robustness to PN, and 2) the limited resolution of ultra-high speed low power ADCs to few bits (limited quantization levels). Thus, low order modulation schemes with GSM or other IM techniques are required to achieve a low-power ultra-high data rate system.

When using the same modulation schemes, GSM and SMX have the same PAPR only if an RF antenna switching is applied after the PA. However, this switching causes spectral regrowth due to pulse time-truncation at each symbol period and thus reduces the spectral efficiency of GSM. A possible solution is to have full-RF chain Tx architecture $N_{RF} \approx N_t$ that transmits the pulse tails when a TA is inactive. This solution leads to higher transmitter cost (for AP can be tolerated) and a higher PAPR compared to SMX since GSM PAPR highly depends on the modulation schemes and the number of inactive TAs.

Note that the PAPR affects the PA efficiency and thus the system power consumption. This drawback of GSM can be mitigated by simple PAPR reduction techniques [29]. As conclusion, the RF switching needed to be performed after the PA in order to maintain the same PAPR, induces a spectral efficiency decrease in the GSM transmitter which can be re-adjusted by using a full-RF architecture, i.e., more RF chains, along with PAPR reduction techniques compared to QPSK- SMX. This can be tolerated for the base stations APs, and it is more appropriate for ultra-high data rates system since the RF-switching is no more needed and the spectral efficiency gain by IM is conserved. However, the advantage of low-order APM with spectral-efficient IM proved in this study and the aforementioned GSM drawbacks motivated us to propose later on the filter IM domain detailed in [23] [24] and [4], and evaluated in Section 2.3.2 and Section 2.3.3.

2.3.1.4 Link Budget estimation

The link budget for SMX and full- RF GSM subjected to PN in indoor sub-THz channels for downlink ultra-high wireless data rates is presented. In this link budget estimation, the system configuration presented in Figure 14b with medium PN is used to estimate the required transmit power for achieving the needed SNR at un-coded BER= 10^{-4} . The link budget, the estimated total power consumption and the data rates using GSM and SMX are presented in Table 5 with different values of total system bandwidth. In Table 5 **Erreur ! Source du renvoi introuvable.**, the required transmit power P_t with

small distance communication is calculated from the required SNR according to the following parameters:

$$\begin{aligned}
 N_{Thermal} &= 10\log_{10}(k \cdot T \cdot W) + 30 & \text{dBm} \\
 N_{Floor} &= N_{Figure} + N_{Thermal} & \text{dBm} \\
 Rx_{Level} &= SNR + N_{Floor} & \text{dBm} \\
 fspl &= 20\log_{10}\left(\frac{4\pi d f_c}{c}\right) & \text{dB} \\
 EIRP &= fspl - G_r + Rx_{Level} & \text{dBm} \\
 P_t &= EIRP - G_t & \text{dBm}
 \end{aligned}$$

where k , T , W , N_{Figure} , $fspl$, f_c , c , G_r/G_t and $EIRP$ are Boltzmann constant, the temperature in kelvin, the channel bandwidth, the noise figure, the free space path loss, the carrier frequency, the speed of light in vacuum ($c = 3 \times 10^8 m/s$), receive/transmit antenna gain, and the effective isotropic radiated power respectively. Furthermore, the power consumption is deduced based on the power amplifier (PA) efficiency which is affected by the PAPR.

Table 5: Link budget of SMX and GSM systems with optimal ML detection over sub-THz channels and subjected to medium PN.

| Link Budget | GSM | SMX |
|---|------------------------|-----------------------|
| Carrier frequency (GHz) | 150.00 | |
| Distance (m) | 2 to 8 | |
| Channel Bandwidth W (GHz) | 0.50 | |
| Spectral Efficiency (bpcu) | 12 | |
| Pulse Shaping: Rolloff | Root Raise cosine: 0.2 | |
| Spectral efficiency (b/s/Hz) | 10 | |
| Data Rates per Channel (Gbps) | up to 6 | |
| Required Transmit Power P_t (dBm) | -1.96 to 10.08 | 2.04 to 14.08 |
| Transmit antenna gain G_t (dBi) | 10.00 | |
| EIRP (dB) | 8.04 to 20.08 | 12.04 to 24.08 |
| f_{spL} (dB) | 81.98 to 94.02 | |
| Receive antenna gain G_r (dBi) | 10.00 | |
| Received power $R_{x,level}$ (dBm) | -63.94 | -59.94 |
| Thermal noise (PSD) (dBm/Hz) | -174.00 | |
| Noise figure N_F (dBm) | 7.00 | |
| Thermal noise N_T (dBm) | -86.94 | |
| Noise floor N_{floor} | -79.94 | |
| SNR with medium PN (dB) | 16.00 | 20.00 |
| Average PAPR (dB) | 7.66 | 6.18 |
| PA efficiency | 0.32 | 0.38 |
| Power consumption (dBm/channel) | 2.99 to 15.03 | 6.24 to 18.28 |
| 12.5 GHz channel bounding (25 channels) | | |
| Data Rates (Gbps) | ~125 | |
| Total Power consumption (dBm) | 16.97 to 29.01 | 20.22 to 32.26 |
| 48 GHz channel bounding and aggregation (96 channels) | | |
| Data Rates (Gbps) | ~480 | |
| Total Power consumption (dBm) | 22.81 to 34.85 | 26.06 to 38.10 |

It is clear from Table 5 that GSM has a lower power consumption compared to SMX even when using full-RF GSM that suffers from higher PAPR and thus lower PA efficiency and while using the optimal ML detection. Note that the required Effective Isotropic Radiated Power (EIRP) for both systems to reach AP-MS distance up to 8m is less than the maximum allowed EIRP in regulations. In addition, the required transmit power for GSM is achievable using the existing electronic technology, while for SMX system it is 14.08 dBm for 8m AP-MS distance which is more than the currently available output power at sub-THz band.

In our example, PAPR after pulse shaping of QPSK-GSM is 1-2 dB higher compared to QPSK-SMX, but GSM keeps a lower power consumption due to its lower SNR requirement for the same BER. For clarification, GSM requires 3.25 dB less than SMX system, that means less than half of the required power with SMX system. Moreover, the total power consumption and data rates are estimated with different total system bandwidths that are available in the band between 90 GHz and 175 GHz. SMX and GSM systems can reach up to 125 Gigabits per second (Gbps) and 480 Gbps (~0.5 Tbps) when the considered total system bandwidth, after channel aggregation and bounding, is 12.5 GHz and 48 GHz respectively with 0.2 pulse shaping rolloff factor. Note that if the residual PN before detection is in a medium level, the presented system QPSK-GSM can be considered as an appropriate solution for indoor ultra-high wireless data rates system in the sub-THz while having an acceptable AP power consumption.

Therefore, GSM and SMX is compared from different perspectives subjected to realistic sub-THz impairments in an indoor environment. The simulations result reveal that MIMO GSM outperforms SMX for all PN levels in the sub-THz channels using ULA or URA array geometry with non-coherent detection. The performance gap increases with the increase in PN, where GSM outperforms SMX in terms of BER even when both systems use same modulation order. Among SMX systems, QPSK-SMX achieves better performance than 16QAM-SMX at the cost of higher detection complexity. The performance of higher order QAM-SMX is primarily limited due to higher sensitivity to PN. In addition, GSM system with non-coherent detection achieves good performance in the presence of low and medium PN, and a PN mitigation is required for strong PN case. Finally, compared to SMX system, the GSM system with low modulation order offers better performance, lower complexity, lower power consumption (less than half compared to SMX) and higher robustness to PN and few-bits ADC resolution requirement, which make it a potential candidate for ultra-high data rates in sub-THz bands. However, full-RF GSM may suffer from higher transmitter cost and PAPR but it overcomes the ultra-fast RF switching issue and the spectral efficiency degradation. Moreover, we would like to highlight that low order modulation schemes are required to allow related systems to survive with sub-THz technological limitations, which imposes the use of spectral efficient IM techniques in order to achieve ultra-high data rates.

In the hereafter subsection, the GSM and SMX system are compared to the novel FSIM scheme from different perspectives and analyzed using sub-THz wireless channel (Scenario #5).

2.3.2 Proposed Generalized MIMO system with FSIM scheme

It is worth mentioning that GSM system with power-efficient modulation (e.g. QPSK) is a promising candidate for the sub-THz system even with a medium PN level when the optimal detection is considered [15], [28]. However, it has some performance degradation with highly correlated channels like those in sub-THz bands that can be reduced by an efficient legitimate TAC set selection and spatial bit-mapping [21].

A novel domain for IM named “Filter domain” is proposed in [23]. This new dimension generalizes many existing modulations (OOK, PPM, Nyquist and Faster-than-Nyquist system with conventional modulations) and SISO-IM domains (e.g., time and frequency IM domains). The frequency IM domain can be seen as a special case of the filter IM domain because the activation/deactivation of a frequency band or a subcarrier is just an application of a bandpass/zero filter. Similarly, the time IM domain counterpart and many other existing modulation schemes can also be considered as a special case of the filter IM domain, as discussed in [23]. The filter IM domain allows us to achieve a high SE gain in SISO since it can be configured to fully use all the available time and frequency resources. A Filter Shape IM (FSIM) was also proposed in [23], where the information bits are emitted through APM symbol and index of a transmit filter that can be changed at the symbol rate. At the transmitter side, a filter bank with N different pulse shaping filters is used to explore the indexation gain that leads to $\log_2 N$ as SE enhancement in SISO-FSIM.

A generalized SMX system is proposed motivated by the different advantages of FSIM scheme and its generalizations for various existing IM schemes [24]. Thus, this system includes different existing schemes as special cases (e.g., SMX with conventional APM, MIMO-OFDM-IM [30], and SMX with any time/frequency IM), since filter IM domain can be easily configured to change the emitted signal [23]. The transmission of different FSIM symbols from the TAs allows achieving a higher SE and EE gain. In other words, any small SE enhancement by FSIM in SISO has a tremendous impact when it is extended to MIMO system, where the overall SE gain by SMX FSIM compared to SMX QAM is $N_t \log_2 N$ for $N_t \leq N_r$.

In addition, a simple receiver for SMX-FSIM is presented in this subsection, where a sample level equalization is performed, and followed by a parallel Matched Filter (MF) based detector. The proposed parallel detection for SMX-FSIM provides good performance with prominent complexity reduction compared to the joint Maximum Likelihood (ML)-based detector (for more details see [24] and [4]).

The proposed SMX-FSIM system conveys information bits in the signal and filter IM domains. The VBs are encapsulated by the different filter shapes indices that are used for pulse shaping of the N_t simultaneously transmitted APM symbols. It is worth mentioning that the transmit spatial IM (e.g., GSM system) conveys all the VBs by a single index (index of activated TAC), and its misdetection leads to bit errors in most of the VBs and also in the real bits of all transmitted APM symbols (i.e., N_a APM symbols in GSM will be most probably mis-detected when an error occurs in the TAC index detection). However, the decentralization of VBs encapsulation in SMX-FSIM avoids the highlighted single point of failure in GSM system.

2.3.2.1 System model

In the design of the novel FSIM based MIMO transceiver and its analysis, we considered most of the sub-THz and's peculiarities. In particular, the following points technological limitations, RF impairments, and sub-THz channel characteristics are considered in the waveform and system design phase:

- Low transmit output power with limited achievable SNR. Thus, the new sub-THz waveform should be energy efficient to maintain good performance.
- Important RF impairments such as carrier frequency offset (CFO) and phase noise of the oscillator that increase at higher frequencies [26]. The CFO can be estimated and cancelled, but the PN's dominant term in a wide sub-THz band that cannot be completely compensated is the random Gaussian process. This random term of the PN has the highest impact on performance degradation [31]. Thus, a waveform robust to PN is required to maintain a good performance with the residual PN.
- A low data converters resolution (quantization levels) is preferred to avoid the high cost and power of the ultra-high sampling rate data converters (ADC/DAC) with high resolution.

Therefore, in our approach to design the proposed novel MIMO transceiver, we insist on using a power-efficient single carrier modulation with low order modulation to provide better robustness for sub-THz bands and survive with these limitations. However, to reach ultra-high data rates in the order of Terabits per second, a spectral efficient IM technique is required even with the large available bandwidth, and thus we exploited our novel Index Modulation domain “Filter IM domain”. The proposed system will enhance the SE by exploiting all available time, frequency, and spatial resources in contrast to most IM domains. Moreover, the proposed SMX-FSIM transceiver will also enhance the EE because the VBs, in general, can be detected at lower SNR.

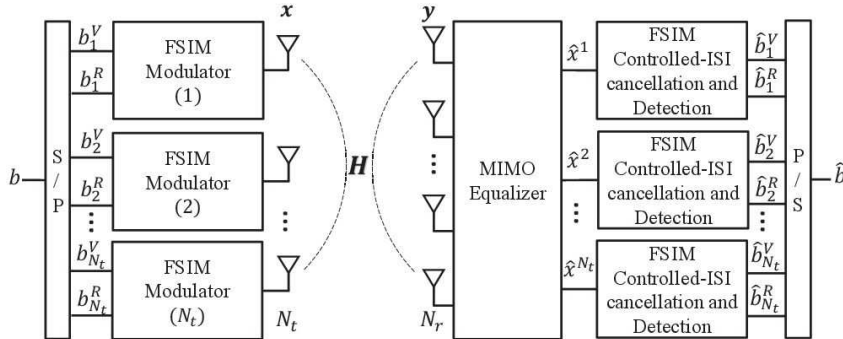


Figure 17: System model of SMX-FSIM transceiver $N_t \times N_r$ described in [4].

Figure 17 consider a $N_t \times N_r$ MIMO-SMX system ($N_t \leq N_r$), where N_t and N_r are the number of transmit and receive antennas respectively. Here, the FSIM scheme that conveys information bits by the index of the different filter shapes and the APM symbols is considered to achieve high SE and EE gain. Note that this system SMX-FSIM in the filter IM domain allows to use all available resources in contrast to other IM domains (time, frequency, antennas, etc.).

The filter bank for each FSIM modulator shown in Figure 17 includes N different filter shapes where N is a power of 2 and it's described in [24]. Without loss of generality, we consider that SMX-FSIM uses the same filter bank and APM for all TAs. Subsequently, the total number of bits per SMX-FSIM symbol SESMX-FSIM can be expressed as:

$$\mathcal{L}_{SMX-FSIM} = N_t(\log_2 N + \log_2 M) = N_t \log_2 N + \mathcal{L}_{SMX-QAM}$$

where $\mathcal{L}_{SMX-QAM} = N_t \log_2 M$ is the number of transmitted bits of a conventional MIMO-SMX system with N_t TAs and M -ary APM. It is clear that the SE gain increases linearly with the number of TAs, and it is $N_t \log_2 N$ higher than that of the conventional MIMO-SMX system with the same M -ary APM. For more details on the MIMO FSIM system model check Deliverable 2.1-addendum at [4] and [24].

After considering the sub-THz aspects in the design phase of the proposed SMX-FSIM system, we studied in this section the proposed transceiver in MIMO sub-THz channels generated from a ray-based deterministic channel model by our BRAVE partner. In addition, we evaluated the system performance of the proposed system and other sub-THz candidates with RF impairments. Finally, different sub-THz system are compared from different perspectives to deduce the most promising candidate.

2.3.2.2 Spectral Efficiency Analysis: SMX-FSIM vs existing MIMO techniques

In this section, the spectral efficiency of different MIMO techniques with different number of TAs N_t and modulation order M is analyzed. This comparison considers the conventional SMX with linear APM (QAM, PSK), and several transmit spatial modulations with/without APM that uses the TA(s) indices to convey additional information bits. The SE of these systems are summarized in Table 6 while assuming $N_r \geq N_t$, Figure 18 and Figure 19 compare their SEs as function of number of TAs with $M = 4$ and $M = 16$ respectively. For clarification, the Extended SSK (ExSSK) and Variable N_a GSM (VGSM) (shown in Table 6) allow a variable number of active TAs to increase the SE. For the same reason, a separate indexation for the in-phase and quadrature components is considered in Bi-SSK and Quadrature SM. It is clear that the highest SE is achieved by the conventional SMX-APM, GSM, and the proposed SMX-FSIM system due to the important multiplexing gain with/without IM, more details in [24].

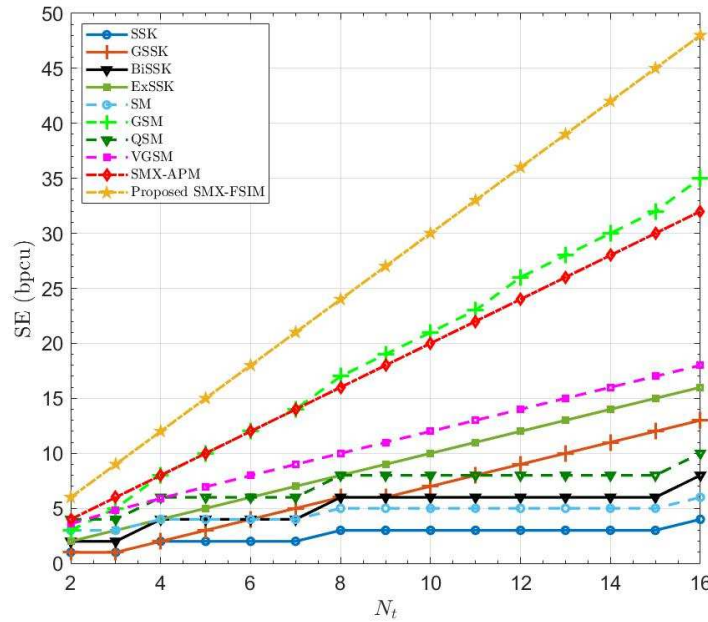


Figure 18: Maximum SE for different MIMO techniques: M=4 for systems with APM, $N_a = [1, \dots, N_t - 1]$ for fixed N_a schemes, and N=2 for FSIM [24] and references therein .

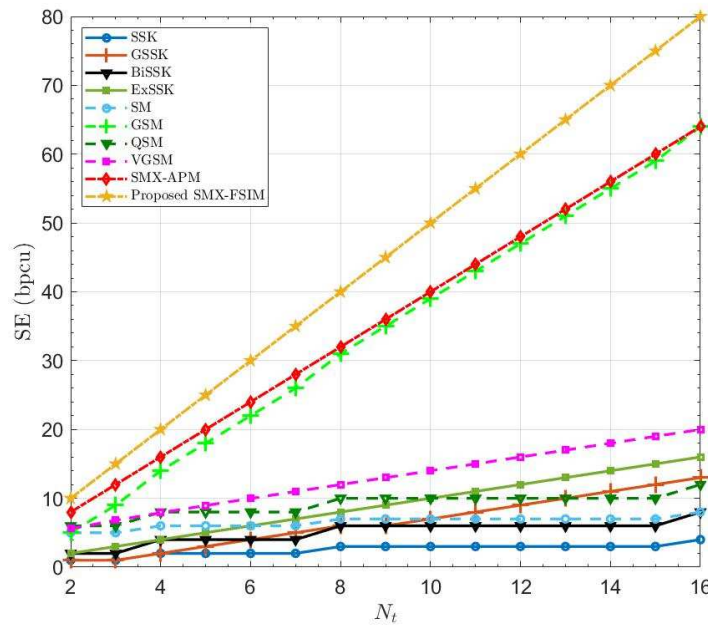


Figure 19: Maximum SE for different MIMO techniques: M=16 for systems with APM, $N_a = [1, \dots, N_t - 1]$ for fixed N_a schemes, and N=2 for FSIM [24] and references therein.

Table 6: Spectral efficiency of different $N_t \times N_r$ MIMO techniques [24] and references therein.

| | System Name | Spectral Efficiency \mathcal{L} (bpcu) | N_a number of activated TA(s) |
|---------------------|-------------|---|---------------------------------|
| SMX | SMX-APM | $N_t \log_2 M$ | N_t |
| | SMX-FSIM | $N_t \log_2 M + N_t \log_2 N$ | N_t |
| | SSK | $\lfloor \log_2 N_t \rfloor$ | 1 |
| | GSSK | $\lfloor \log_2 C_{N_t}^{N_a} \rfloor$ | N_a |
| | Bi-SSK | $2 \lfloor \log_2 N_t \rfloor$ | $N_a = 1$ for IQ: {1, 2} |
| | ExSSK | N_t | {0, ..., N_t } |
| | SM | $\log_2 M + \lfloor \log_2 N_t \rfloor$ | 1 |
| | GSM | $N_a \log_2 M + \lfloor \log_2 C_{N_t}^{N_a} \rfloor$ | N_a |
| | QSM | $\log_2 M + 2 \lfloor \log_2 N_t \rfloor$ | $N_a = 1$ for IQ: {1, 2} |
| Transmit Spatial IM | VGSM | $\approx \log_2 M + \log_2(2^{N_t} - 1)$ | {1, ..., N_t } |

2.3.2.3 Comparison of SMX-FSIM, conventional SMX and GSM in sub-THz environment

The best candidates in terms of SE highlighted in previous subsection are evaluated from different perspectives while considering sub-THz band challenges and limitations. Note that SMX-QAM and GSM system are investigated in sub-THz environment shown in Figure 13, and the results show that using lower modulation order M is more efficient especially in sub-THz with RF impairments and limitations such as higher robustness to PN, lower transmit power and less ADC resolution requirements. For this reason, the proposed SMX-FSIM system using QPSK is compared to their equivalent GSM and SMX schemes with the same SE.

2.3.2.3.1 Performance in sub-THz channel with RF impairments

In this sub-section, these candidates' performance is evaluated under indoor sub-THz channels and subjected to PN impairment.

The sub-THz MIMO channels are generated using ray-based deterministic channel model. For instance, different channel realizations are generated using a ray-based deterministic channel model for sub-THz Band (mainly between 90-200 GHz). In this subsection we focused on the downlink hotspot (or kiosk) indoor scenario operating at 150 GHz where the Access Points (APs), acting as transmitters, and the User Equipment (UEs), acting as receivers, are equipped with N_t and N_r isotropic antennas respectively. The setup environment is described in Figure 13, where 10 APs mounted on the ceiling with fixed positions and 50 UEs at random positions are used to generate different channel realizations as shown in Figure 13. In our simulations, the distance between the AP and UE is up to 8 meters (m), and its average is 5 m. The MIMO channels are obtained with Uniform-Linear-antenna Array (ULA).

For a wideband system like our case in sub-THz, the PN impairment can be modeled by Gaussian distribution with zero mean and σ_g^2 variance which is the dominant term of the PN that affects the wideband system performance , and in the following different PN levels are considered: low $\sigma_g^2 = 10^{-3}$, medium $\sigma_g^2 = 10^{-2}$, and high $\sigma_g^2 = 10^{-1}$.

For a fair comparison, the SMX FSIM, SMX QAM, and GSM systems are configured to achieve the same SE of 12 bpcu with the same number of RAs, and same modulation scheme QPSK or the same number

of TAs, and without PN mitigation (non-coherent detection). The configuration of these systems is summarized in Table 7 where we can observe the different systems of the same SE either have same M modulation order or same N_t , and they use the full-RF transmitter architecture. Note that a pulse-shaping filter is considered with all MIMO systems before transmission with the same parameters shown in Table 8, and a low complexity receiver based on ZF equalizer is adopted with all systems to allow practical implementation of downlink scenario where the UE has complexity and energy constraints

The non-coherent SMX 2-FSIM-QPSK system with low and medium PN levels achieves the best performance compared to its competitor systems as depicted in Figure 20 and Figure 21. For instance, SMX 2-FSIM-QPSK has a 3.9 dB and 18 dB gain compared to SMX-8QAM with same number of TAs and SMX QPSK (same modulation) respectively. Similarly, SMX 2-FSIM-QPSK has 9.8 dB gain compared to GSM-QPSK with $N_t = 9$ and $N_a = 3$, while GSM-QPSK with $N_t = 6$ and $N_a = 5$ suffers from important error propagation that leads to error floor. The GSM system in general is more prone to error since the misdetection of the activated TAC does not cause only virtual bit errors but it propagates to the detection of all transmitted APM symbols in the same MIMO vector due to the attempt of APM symbols detection on non-activated TAs.

Table 7 System configuration for sub-THz candidates with 12 bpcu.

| System | N_t | N_r | M | N_a | N |
|----------|-------|-------|-----|-------|-----|
| SMX-FSIM | 4 | 10 | 4 | 4 | 2 |
| SMX-QAM | 4 | 10 | 8 | 4 | 1 |
| SMX-QAM | 6 | 10 | 4 | 6 | 1 |
| GSM | 6 | 10 | 4 | 5 | 1 |
| GSM | 9 | 10 | 4 | 3 | 1 |

Table 8 Simulation Parameters for MIMO SMX-FSIM and SMX-QAM

| Parameters | Value |
|---|--------------------------|
| N_t for SMX-8QAM, SMX 2-FSIM-QPSK | [4, 8, 10] |
| N_t for SMX-QPSK | [6, 12, 15] |
| N_r | [8, 12, 16] |
| η | 10 |
| Oversampling factor: λ | 8 |
| Filter's length: L | 81 |
| Pulse shaping filter for Conventional Transceiver | Root Raised Cosine (RRC) |
| Number of channel realizations | 500 |
| Total Number of symbols | 5×10^6 |

This drawback of GSM clearly appears when $N_t = 6$ and $N_a = 5$ in both figures, while the other GSM configuration performs better since it is well known that GSM performance is enhanced when transmitting most of the information bits by means of IM. However, the SMX FSIM system overcomes GSM drawback of error propagation to all APM symbols by the decentralization of virtual bits transmission to N_t groups of virtual bits, and thus a misdetection of filter index can affect only the subsequent single APM symbol detection and not the all the transmitted APM symbols like in GSM. Furthermore, the filter index misdetection does not cause necessarily an APM symbol error since the transmitted APM symbol is not completely lost in contrast to GSM that drops the APM symbols on non-activated TAs.

A similar conclusion can be drawn at medium PN level ($\sigma_g^2 = 10^{-2}$) from Figure 21. Besides, it is worth mentioning that SMX FISM with linear receiver is the only system among SMX-QAM and GSM

able to operate at this PN level without an error floor. However, all these system configurations suffer from an error floor when subjected to very high PN level ($\sigma_g^2 = 10^{-1}$). But it is worth mentioning that a low PN oscillator at sub-THz frequencies is recently designed in [32], and thus the design of a system with a robustness up-to medium PN level is affordable for most scenarios.

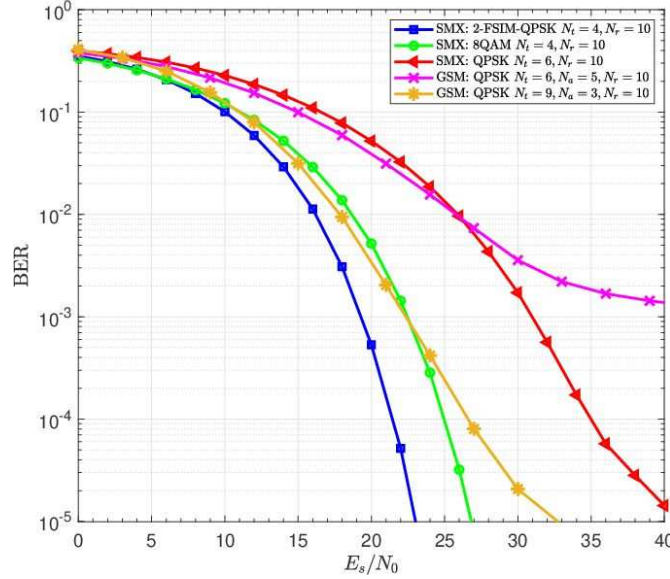


Figure 20: Un-coded BER performance of the proposed non-coherent SMX FSIM compared to SMX-QAM and GSM in sub-THz channel with low PN ($\sigma_g^2 = 10^{-3}$). The SE for all systems is 12 bcpu.

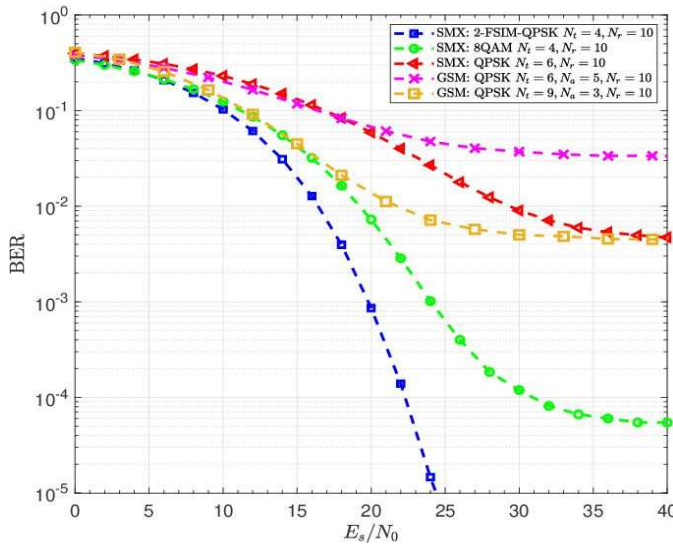


Figure 21: Un-coded BER performance of the proposed non-coherent SMX FSIM compared to SMX-QAM and GSM in sub-THz channel with medium PN $\sigma_g^2 = 10^{-2}$. The SE for all systems is 12 bcpu.

2.3.2.3.2 Complexity analysis

In this section, we characterize these systems in terms of the computational complexity of the optimal ML and the low complexity ZF based equalizer/detector. Their average complexity per symbol is expressed in terms of Real Multiplications (RMs) and summarized in Table 9. Note that each Complex

Multiplication (CM) consists of 4 RMs, and it can be computed using 3 RMs if one term is known in advance. The computational complexity of the ZF matrix for the $N_r \times N_t$ channel H is expressed in terms of RMs as follows:

$$\mathcal{C}_{W_{ZF}} = 4 \left(\frac{2N_t^3 + 3N_t^2 - 5N_t}{6} + 2N_r N_t^2 \right),$$

where the first term is for the square matrix $H^H H$ inversion and the second term represents the needed multiplications to deduce the pseudo inverse of H. However, the ZF matrix calculation can be computed once when the channel is static for the duration of N_s symbols. Note that the ZF equalization for SMX-APM and GSM can be performed after matched filtering and down-sampling, while that for SMX-FSIM should be done for the whole received signal (all samples: $N_s \lambda + L - 1$) prior to the filter index detection, and then perform the matched filtering using the detected filter. Hence, the sample level equalization for FSIM is approximately λ times larger than that of symbol level equalization.

The complexity of SMX-FSIM receiver lies in the equalization, ISI estimation and cancellation block, and the matched filter detector. The matched filter on each TA performs N convolutions with a filter of length L known in advance, then the middle sample is used for detection after sampling. Thus, this middle sample is computed by L CMs when the signals of the convolution are completely overlapped. For the filter index and APM symbol detection, $N + M$ Euclidean Distances (EDs) are computed where ED consists of 2 RMs. Thus, the matched filter complexity is expressed as:

$$\mathcal{C}_{MF} = 2NL + 2N + 2M$$

Table 9: Average Computational complexity in terms of real multiplications for SMX-FSIM, SMX-APM, AND GSM equalizers/detectors.

| System | ZF equalizer/detector complexity | ML complexity |
|-----------------|---|---|
| SMX-FISM | $\left(\frac{N_s \lambda + L - 1}{N_s}\right) 4N_t N_r + N_t (\mathcal{C}_{MF} + \mathcal{C}_{ISI\ cancellation}) + \mathcal{C}_{W_{ZF}}/N_s$ | $2^{\mathcal{L}_{SMX-FSIM}+1} (2N_t + 1)LN_r$ |
| SMX-APM | $4N_t N_r + 2MN_t + \mathcal{C}_{W_{ZF}}/N_s$ | $2^{\mathcal{L}_{SMX}+1} (2N_t + 1)N_r$ |
| GSM | $4N_a N_r + 2MN_a + \mathcal{C}_{W_{ZF}}/N_s$ | $2^{\mathcal{L}_{GSM}+1} (2N_a + 1)N_r$ |

The ISI estimation and cancellation block (that contains a MF detector for tentative decisions, and the Tx filter output regeneration that multiplies the estimated tentative APM symbol with the filter (L CMs= $3L$ RMs). Similarly, the feedback of the previously detected symbol contains L multiplication of complex number by real value $2L$ RMs. Afterward, an overlap and add is performed to deduce the estimated ISI, then it is subtracted from the input signal where these steps contain only additions/subtractions. Therefore, the total complexity of the ISI estimation and cancellation block is:

$$\mathcal{C}_{ISI\ cancellation} = \mathcal{C}_{MF} + 4L.$$

The ZF based equalizer/detector provides a prominent complexity reduction for all systems compared to the ML counterpart, and SMX-FSIM suffers from higher receiver complexity which is proportional to

the filter length L as shown in Table 9. However, it is clear from the results in derivable D2.1-addendum [4], that the performance of SMX-QAM and GSM with their linear detection are not satisfactory as SMX-FSIM and the formers have a high error floor with medium PN level ($\sigma_g = 10^{-2}$). Therefore, the additional complexity of SMX-FSIM linear receiver, compared to SMX-APM and GSM, comes with a tremendous system performance and robustness to PN that are critical factor for sub-THz system with RF impairments and limited SNR.

It is worth mentioning that the SMX-FSIM transmitter has a low complexity because the filtering operation for each symbol is a merely simple multiplication, and the OLA block is composed of adders only that means FSIM transmitter does not introduce an additional noticeable computational complexity compared to other systems.

2.3.2.3.3 Hardware cost and design issues

The hardware cost depends on the number of used RF-chains that contains the most expensive hardware components. In [4], it is highlighted that the full-RF transmit architecture is required with transmit spatial IM schemes to avoid SE degradation. Therefore, the number of RF-chains at Tx side is same as number of TAs N_t with all schemes, and thus it is clear from Table 7 and Figure 18 and Figure 19 using any M -ary modulation scheme that SMX-FSIM system with only 2 filter shapes requires the minimum number of TAs N_t (and thus RF-chains) to achieve any SE. Therefore, SMX-FSIM allows to have the minimum possible cost for the transceiver hardware. Note that GSM receiver with some configurations can have lower cost by using smaller number of RF-chains equal to N_a , but this condition ($N_r = N_a < N_t$) can highly degrades the system performance with low complexity detectors.

It is worth mentioning that the full-RF transmitter architecture with GSM eliminates the high-speed RF switching challenge at the price of higher cost. The practical implementation of these MIMO schemes requires careful antenna array design to have low spatial correlation, and especially for GSM system since the misdetection of the activated Transmit Antenna Combination (TAC) leads also to APM symbols error and thus highly degrades GSM overall performance.

2.3.2.3.4 PAPR, Link Budget and Power consumption

Based on a MIMO SC transceiver with pulse shaping, the corresponding Complementary Cumulative Distribution Functions (CCDFs) of the PAPR of SMX-FSIM, SMX-QAM and GSM systems are shown in Figure 22. The PAPR for all these schemes is evaluated over one TA, since all TAs for each system have similar PAPR when using same M -ary scheme for different TAs and TAs activation is equiprobable in GSM. SMX-FSIM use the non-Nyquist filter shapes designed for filter IM domain, while the pulse shaping for SMX-QAM and GSM system is performed with root raised cosine filter.

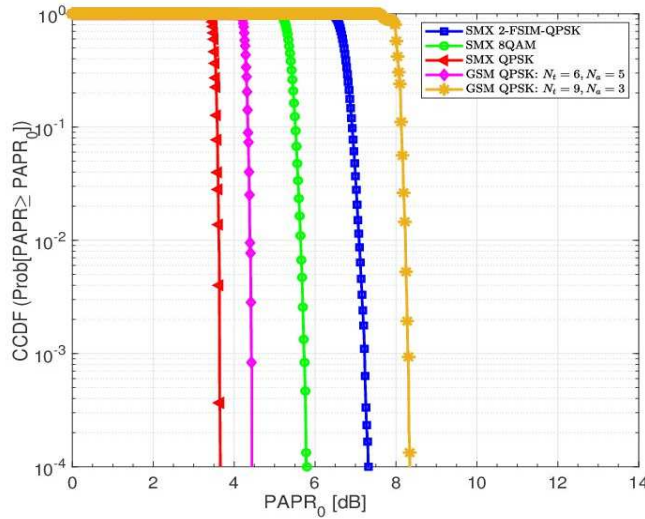


Figure 22: Comparison of CCDF of PAPR for the SMX FSIM, the SMX QAM and the GSM systems with pulse shaping having SE=12 bpcu. SMX FSIM uses the filter shapes presented in [23], while SMX QAM and GSM use RRC filter.

The CCDF that represents the probability of having a PAPR higher than a $PAPR_0$ threshold depicted in Figure 22 shows clearly that SMX QPSK have the lowest PAPR 3.65 dB at CCDF of 10^{-4} , and the PAPR increases to 5.8 dB SMX 8QAM due to the higher M -ary scheme (8QAM), and to 4.4 dB (resp. 8.3 dB) with GSM using $N_t = 6, N_a = 5$ (resp. $N_t = 9, N_a = 3$). It is clear that the PAPR of GSM increases when the ratio $\frac{N_a}{N_t}$ decreases due to the lower average power caused by zero symbol transmission when the TA is inactive. Concerning SMX-FSIM, its PAPR is 7.3 dB due to the used filter shapes that are designed to have low filter's correlation and limited ISI without any PAPR constraint. The higher PAPR reduces the Power Amplifier (PA) efficiency, and thus it affects the system power consumption. In the following, the link budget for these systems is calculated from the required SNR to achieve uncoded BER = 10^{-4} .

Table 10: Link budget and power consumption of un-coded SMX-FSIM, SMX-QAM and GSM systems with ZF based detection over sub-THz channels subjected to low PN

| System Parameters | SMX FSIM | SMX 8QAM | SMX QPSK | GSM ($N_t = 9, N_a = 3$) |
|-------------------------------------|-----------------------|----------------------|-----------------------|----------------------------|
| Carrier frequency (GHz) | | | 150.00 | |
| Distance (m) | | | 2 to 8 | |
| Channel Bandwidth W (GHz) | | | 0.50 | |
| Required Transmit Power P_t (dBm) | -5.46 to 6.59 | -1.96 to 10.09 | 8.04 to 20.09 | 0.04 to 12.09 |
| Transmit antenna gain G_t (dBi) | | | 10.00 | |
| EIRP (dB) | 4.54 to 16.59 | 8.04 to 20.09 | 18.04 to 30.09 | 10.04 to 22.09 |
| f_{spl} (dB) | | | 81.98 to 94.03 | |
| Receive antenna gain G_r (dBi) | | | 10.00 | |
| Received power Rx_{level} (dBm) | -67.44 | -63.94 | -53.94 | -61.14 |
| Thermal noise (PSD) (dBm/Hz) | | | -174.00 | |
| Noise figure N_{Figure} (dBm) | | | 7.00 | |
| Thermal noise $N_{Thermal}$ (dBm) | | | -86.94 | |
| Noise floor N_{floor} | | | -79.94 | |
| Required SNR with low PN (dB) | 12.5 | 16 | 26 | 18 |
| PAPR (dB) at CCDF = 10^{-4} | 7.3 | 5.8 | 3.65 | 8.3 |
| PA efficiency | 0.34 | 0.4 | 0.52 | 0.31 |
| Power consumption (dBm) | -0.77 to 11.27 | 2.02 to 14.06 | 10.88 to 22.93 | 5.13 to 17.17 |

The link budget for the different systems in indoor scenarios (Kiosk, enhanced throughput WLAN, etc.) with a distance up to 8 m is depicted in Table 10, where the GSM system with $N_t = 6$, $N_a = 5$ is omitted due to the high error floor. It is clear that SMX FSIM requires the lowest transmit power to guarantee un-coded $\text{BER} = 10^{-4}$ due to its better system performance. This low transmit power requirement is an important advantage for sub-THz bands, since the output transmit power is very limited at high frequencies with current technology. The required transmit power and the higher EIRP make SMX QPSK and GSM with linear ZF based detector impractical in current technology in contrast to their results with ML detection discussed in [15].

In addition, it is worth mentioning that SMX-FSIM maintains its superiority in the power consumption even without channel coding despite the PAPR increase by the used filters due to the important performance SNR gain. For instance, SMX-FSIM with linear receiver provides a 2.79 dBm power gain compared to SMX 8QAM and more than 10 dBm compared to SMX-QPSK as shown in Table 10. It is worth mentioning that acquiring a wider total bandwidth in sub-THz bands by channel aggregation/bonding, adopting a higher number of filter shapes, and/or a large-scale MIMO with SMX-FSIM allows achieving a low-power wireless Tbps system.

Therefore, SMX-FSIM requires less SNR to reach the desired performance even without channel coding, and the proposed system requires the minimum number of transmit antennas to achieve any SE, as shown in Figure 18 and Figure 19 that limit the transceiver cost and power consumption related to RF chains and to achieve the desired performance so a higher EE is provided. Hence, SMX-FSIM requires less parallel modulator and RF chains than the most spectral-efficient existing MIMO systems, which means lower hardware cost and power consumption even with PN impairment. This cost and power consumption of SMX-FSIM remains the minimum compared to the other candidates, even when considering a massive MIMO system exploiting beamforming gain to compensate the sub-THz/THz losses.

Note that when considering a higher PN level, all systems with linear ZF based detector suffer from an error floor except SMX-FSIM as shown in Figure 21, and the latter consumes only 1.5 dB more than its power consumption at the low PN level in contrast to all others without any channel coding.

2.3.2.4 Summary about the sub-THz candidate system

The proposed SMX-FSIM system is shown to achieve the highest SE gain among the existing MIMO systems with/without IM even with 2 filter shapes and low order modulation. For instance, the achieved gain with SMX FSIM system is $N_t \log_2 N$ higher than that of SMX QAM using the same modulation order and the number of antennas. It is also important to mention that SMX FSIM fully utilizes all time, frequency, and spatial resources in contrast to spatial IM (e.g., GSM,...) that activates a certain number of antennas and requires a full-RF transmitter architecture. In the current study, we are focusing on an ultra-high data rates system for indoor scenarios with power and complexity constraints for the UE receiver, like downlink kiosk application and enhanced throughput WLAN. For this reason, we developed the proposed SMX FSIM system with a linear receiver based on ZF equalizer and parallel MF detectors that allow us to maintain a low and feasible receiver complexity. Compared to the equivalent SMX QAM system of the same SE using either the same modulation order or the same number of TAs, the results reveal that SMX FSIM with a linear receiver and only two non-optimal filter shapes outperforms these equivalent systems. In order to complete our study and propose a new ultra-high data rate system in the sub-THz environment, a complete analysis in the sub-THz indoor environment with RF impairments is provided for the proposed system SMX FSIM, and the other candidates (SMX QAM and GSM).

Finally, it is clear that SMX-FSIM with a linear receiver has better performance and robustness to phase noise, lower transceiver cost, higher SE/EE gain, and lower power consumption compared to its competitor candidates. Therefore, this analysis and discussion summarized in Table 11 promotes SMX-FSIM with a linear receiver as a very competitive candidate for low-power wireless ultra-high data rates system in sub-THz bands. Consequently, the coded SMX-FSIM is proposed and studied in the next sub-section.

Table 11: Summary of different MIMO techniques for low power wireless ultra-high data rates systems in sub-THz bands [24].

| MIMO systems with power-efficient low order APMs and linear based receivers | | | |
|---|---|--------------------------|---|
| Parameter | SMX-FSIM | SMX-QAM | GSM using full-RF Tx architecture |
| Spectral Efficiency (see Figs. 7-8) | $N_t(\log_2 M + \log_2 N)$ High | $N_t \log_2 M$ Medium | $N_a \log_2 M + \log_2 C_{N_t}^{N_a}$ where $N_a \leq N_t$ Medium |
| Robustness to PN (see Figs. 10-11) | High | Low to Medium | Low (High with ML[4]) |
| PAPR (see Fig 12) | Medium | Low | Low to High (depend on M, N_a and N_t) |
| Energy Efficiency (see Table V) | High | Medium | Medium |
| Linear Detector Complexity (see Table IV) | Medium to High (depend on filter length) | Medium | Low |
| Cost based on number of RF chains (see sub-Section IV-C-3) | Low | Low to Medium | High |
| Flexibility (Reconfigurable System) | High | Low | High |

2.3.3 Proposed coded FSIM

2.3.3.1 LLR Derivation

In this section, we consider a coded FSIM scheme to investigate the effect of channel coding on the overall performance in different channels and scenarios. To undergo various channel coding technique as LDPC for example, LLR values are needed at the receiver to decode.

A few changes to the FSIM system model in [23] are needed. The target is to replace Matched filter Detector with LLR detection as first step. First, the LLR derivation for this technique is derived. The exact LLR for a bit b is defined as:

$$L(b) = \log \left(\frac{\Pr(b = 0 | \hat{s})}{\Pr(b = 1 | \hat{s})} \right)$$

Consider I is the set of filter indices, define $I_{k,\beta}$ as the subset of filter indices in which the k -th bit of each element is β (0,1) and S is the set of possible APM symbols, define $S_{k,\beta}$ as the symbol subset in which the k -th bit is β . So, the posteriori probabilities of the k -th virtual bit $b_{I,k}$ for the filter index can be calculated as:

$$p(b_{I,k} = \beta | \hat{s}) \propto \sum_{f \in I_{k,\beta}} \sum_{c \in S} p(\hat{s} | s = c.f), \beta = 0,1$$

Similarly, the posteriori probabilities of the k-th real bit of a symbol:

$$p(b_{S,k} = \beta | \hat{s}) \propto \sum_{f \in I} \sum_{c \in S_{k,\beta}} p(\hat{s} | s = c.f), \beta = 0,1$$

So, the LLR values of both is:

$$L(b_{I,k}) = \ln \left(\frac{\Pr(b_{I,k} = 0 | \hat{s})}{\Pr(b_{I,k} = 1 | \hat{s})} \right) \quad L(b_{S,k}) = \ln \left(\frac{\Pr(b_{S,k} = 0 | \hat{s})}{\Pr(b_{S,k} = 1 | \hat{s})} \right)$$

It's important to note that LLR detectors for existing modulations takes one sample for each symbol that leads in AWGN to complex normal distribution, whereas In FSIM case, LLR takes L samples for each symbol that results in complex multivariate normal distribution. Its definition is that a random vector is said to be L-variate normally distributed if every linear combination of its L components has a univariate normal distribution. Therefore, to apply this distribution in our case we have the following joint PDF:

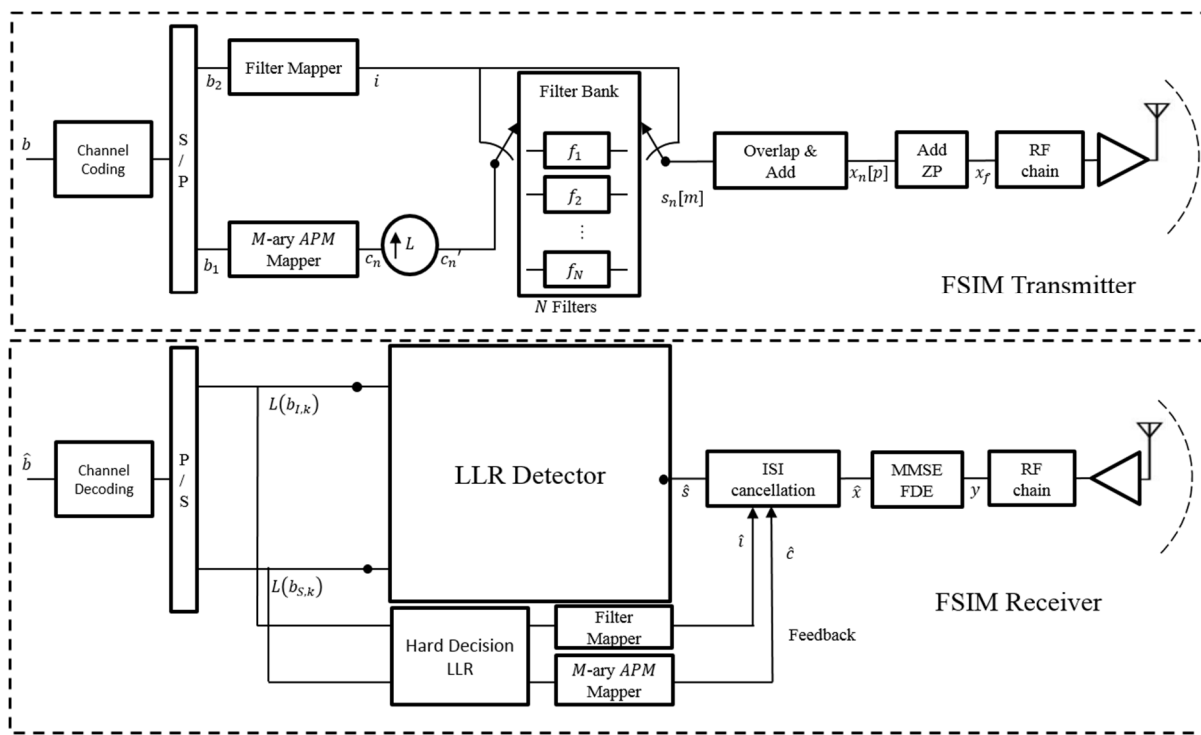
$$f_z(z) = \frac{1}{\pi^L \det(\Gamma)} e^{-(z-\mu)^H \Gamma^{-1} (z-\mu)}$$

Knowing that $\mu = c.f$, $\Gamma = \sigma^2 I_L$ and $z = \hat{s}$. Note that f is the filter shape, c is the complex symbol and I_L : $L \times L$ identity matrix. Since the L samples are independent and uncorrelated, their joint pdf $f_z(z)$ can be expressed as a product of their marginal PDF that follows a complex Gaussian distribution with mean μ_i and same variance σ^2 , we get this simplified from:

$$f_z(z) = \prod_{i=1}^L \frac{1}{\pi \sigma^2} e^{-\frac{|z_i - \mu_i|^2}{\sigma^2}}$$

2.3.3.2 System Model

Using the derivation in the previous section, the new system model for the coded FSIM scheme is shown in Figure 23.



L : Filter Length in samples $L = \eta \cdot \lambda + 1$.

η : Number of symbols in a filter period

λ : Number of samples per symbol

T_f : Filter period

Figure 23: Coded FSIM System Model

The matched filter detector is replaced with an LLR detector based on the derived equations which outputs the LLR values to be used for channel decoding, while they are also used by a hard decision LLR block and afterwards mapped to filter and APM symbols that are fed back into the ISI cancellation block.

2.3.3.3 Performance assessment of coded-FSIM

In this section, the coded FSIM results are presented and compared to various scenarios as regular FSIM with matched filter and the equivalent QAM scheme. Its performance is also assessed with different channel scenarios as AWGN and short range D2D as sectored antenna model in different phase noise levels and coding rates.

2.3.3.3.1 Comparison of LDPC Coded FSIM to QAM in AWGN channel with phase noise

The coded FSIM setup is initially compared to FSIM with matched filter along with the QAM scheme with the same spectral efficiency which is 8-QAM ($SE = 3$ bpcu), knowing that we are using FSIM with two filters $N = 2$ and QPSK having a spectral efficiency $SE = 3$ bpcu. We assume, for simulation the short length LDPC code of size 16200 bits with sparse parity-check matrices from ETSI DVB-S2 standard. The result for this comparison is shown in Figure 24 in terms of BER. It is noticed that an LDPC coded FSIM has a significant gain of around 5 dB over its uncoded version with MF and also a significant gain over the coded 8-QAM of around 3.24 dB after considering the energy of useful bits only.

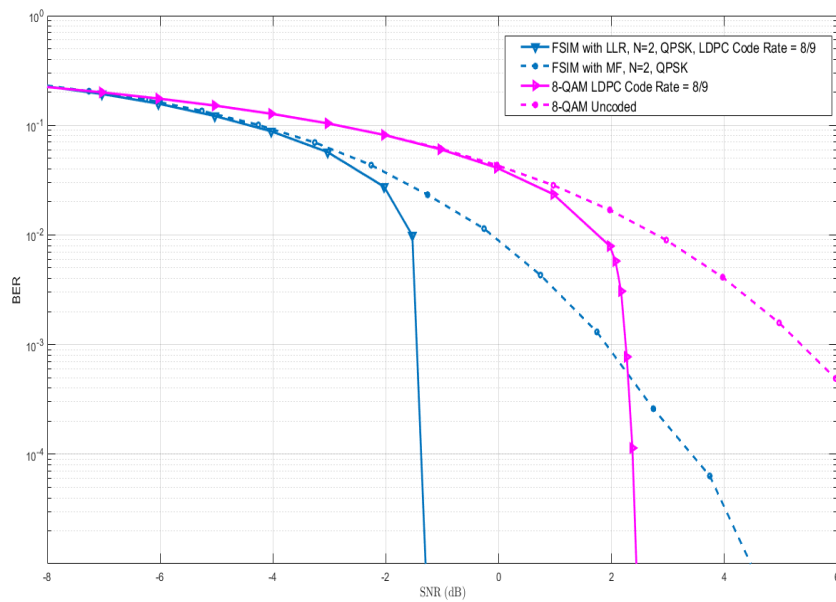


Figure 24: BER performance of FSIM vs. 8-QAM for uncoded and LDPC coded schemes with code rate R = 8/9

The following assessment is based on a coded FSIM system with two filters and QPSK modulation with LDPC code rates $R = [\frac{3}{5}, \frac{8}{9}]$. It is assessed on two phase noise levels: none and medium level. The stated configurations are each compared to the uncoded version on FSIM with the same parameters and channel conditions. As shown in Figure 25, we notice there is no significant effect on the BER performance of coded FSIM due to medium phase noise. While it also shows the benefits of higher coding rate in terms of BER. Note that SNR (dB) is used as an axis, but for results in terms of useful energy per bit, the coding rate and oversampling factor should be considered.

The proposed coded-FSIM system is also evaluated using a realistic sub-THz channel model in D2D scenario in Section 2.5.2.

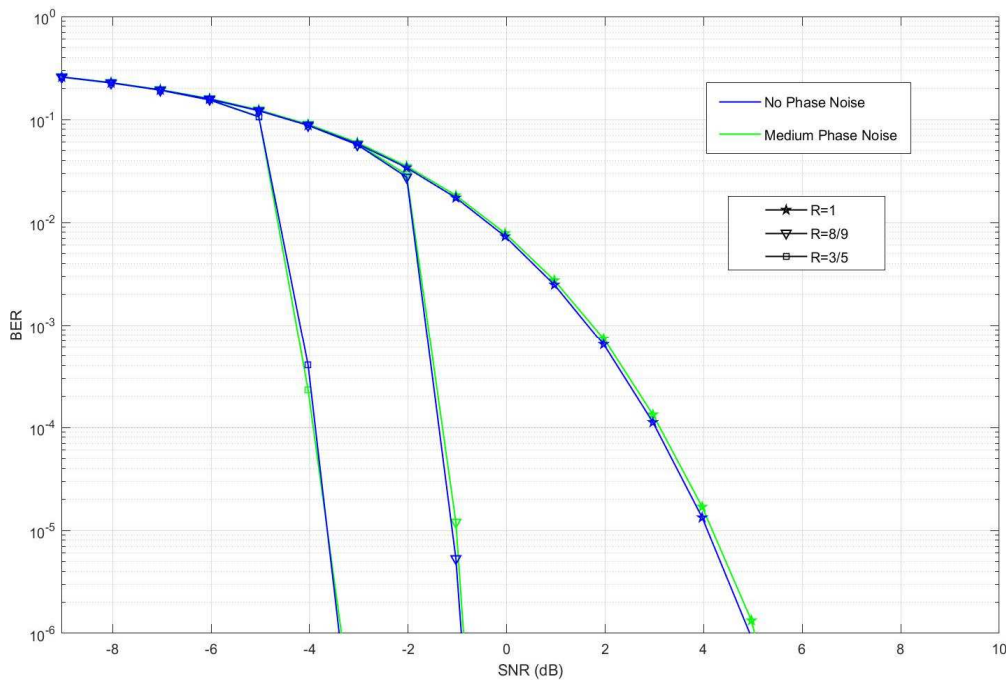


Figure 25: BER performance of Uncoded vs. Coded FSIM with rates: [8/9,3/5] over AWGN channel with two different phase noise levels (none, medium)

2.3.4 Conclusion

In this section, the different MIMO candidate system for low-power ultra-high data rate system (MIMO SMX-QAM, GSM, MIMO FSIM) are evaluated and analysed from different perspectives. It is worth recalling that the latter MIMO FSIM system generalizes different existing Nyquist and Faster-than-Nyquist systems, many existing modulations (e.g., OOK, PPM, QAM, etc.) and IM domains, thanks to the filter IM domain that generalizes many existing modulation and time/frequency IM domains. The results summarized in

Table 11 and the different analyses reveal that SMX FSIM has better performance, higher robustness to PN, lower transceiver cost, higher SE/EE gain and less power consumption. However, these advantages come with a slight receiver complexity increase which is in order of L times higher than other candidates, and this complexity can be reduced by proper design of filter bank with shorter filter length L while respecting FSIM scheme filter requirements (this linear complexity increase is recently minimized, and more details will appear in our future publication). Finally, it is worth mentioning that SMX FSIM in sub-THz channel indoor hotspot or enhanced WLAN scenarios requires much a low SNR even without channel coding under medium phase noise level which is crucial for sub-THz systems with limited transmit output power, and it is the only scheme among the GSM and SMX-QAM candidates that can operate in a medium PN level with linear low complexity receiver.

Moreover, the most promising candidate MIMO FSIM is studied also with channel coding to prove its superiority compared to equivalent system of same SE, and it was shown that 8x8 MIMO-FSIM using only 2 filter shapes and low-order modulation as QPSK with LDPC code and a linear low complexity receiver is able to reach an ultra-high data rate in order of Terabits per second at low SNR with a limited

transmit power even with medium PN level ($\sigma_g^2 = 10^{-2}$). All the results and analysis promote the generalized MIMO-FSIM as a very promising candidate for low-power ultra-high data rates system.

2.4 Scenario #4: Hotspot access network

The presented case study is based on demonstrator #3 described in [5], using the access network design functionalities, as well as the P-QAM, OOK and FSIM modulations.

The considered scenario is a small hotspot area with strong required capacity.

2.4.1 Introduction

The main objective of this case study is to assess the applicability of the low-complexity OOK modulation to a 300-GHz hotspot scenario, and then, to compare the OOK performance to the higher-complexity P-QAM and FSIM modulations.

SISO systems are considered.

The hotspot scenario is located in part of a shopping mall (scenario #3 in [5]), however it could have been similarly installed in a railway station, an airport, or a campus.

In this case study, we are interested in following questions:

- How many sub-THz access points are required to cover the hotspot area with OOK modulation?
- What throughput can be delivered by OOK modulation in such a scenario?
- How many aggregated channels can make OOK equivalent to P-QAM?
- How much additional throughput is offered by FSIM compared to P-QAM?

2.4.2 Models and assumptions

The hotspot area consists of four long tables, with people seated throughout to benefit from very high speed wireless access. The main broadband applications are high-resolution video streaming, file download/upload, and video gaming. This hotspot area is positioned into a large open space of a shopping mall, with some pillars in its close vicinity, and glass partitions at a distance of 7 meters. The hotspot situation is shown by Figure 26.

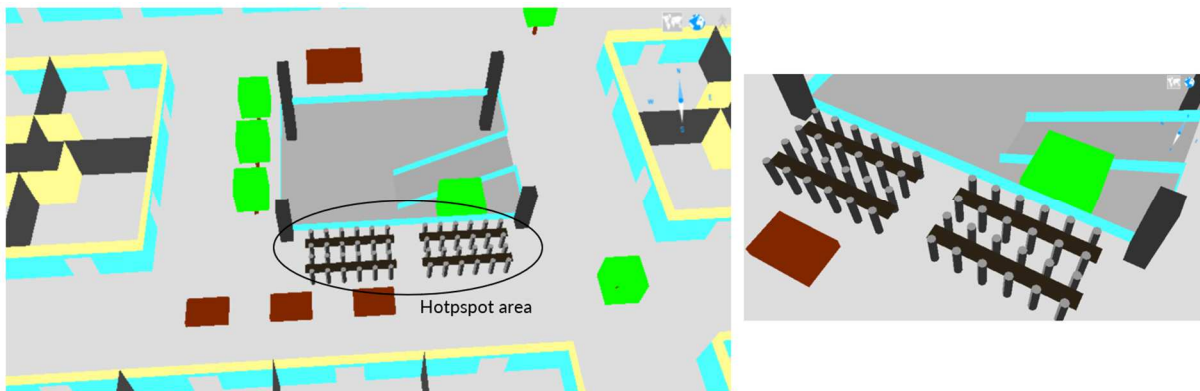


Figure 26 : Hotspot situation.

The width of the simulated hotspot area is $17.75 \text{ m} \times 5.75 \text{ m}$.

The other key distances are illustrated by Fig. 18; the sub-THz access point is supposed to be installed at 4 m above the ground; all people are represented with same height i.e. 1.70 m; and the user equipment (UE) is placed on the table or in the hands of the user, at height 1 m. In this situation, the minimum distance between AP and UE antennas is 3 m, which corresponds to 91.5 dB free-space path-loss at 300 GHz.

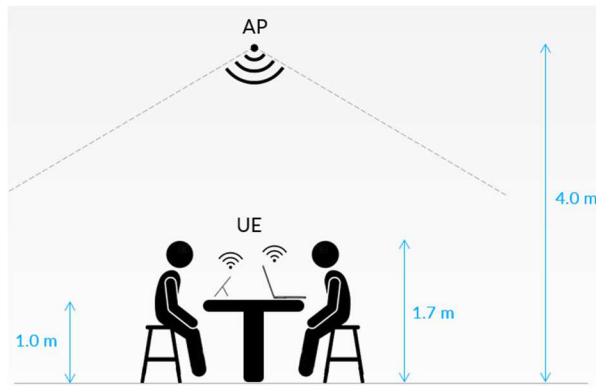


Figure 27 : Hotspot setup.

The downlink link budget and other simulated parameters are given in Table 12. The central frequency is 300 GHz; the channel bandwidth is 2 GHz; and the considered downlink transmit power is 100 mW per channel. Two different link budgets are compared, with respectively 5 dBi and 0 dBi gain at the UE antenna. The OOK, P-QAM and FSIM modulations are compared based on same scenario parameters, except for the SNR–SE mapping and the number of activated channels. Note also that the achieved spectral efficiency of OOK and P-QAM modulations has been computed with target Block Error Rate $\text{BLER} = 10^{-2}$, while the spectral efficiency of the FSIM modulation is obtained from Bit Error Rate $\text{BER} = 10^{-6}$.

Table 12 : Simulation parameters for the downlink hotspot scenario.

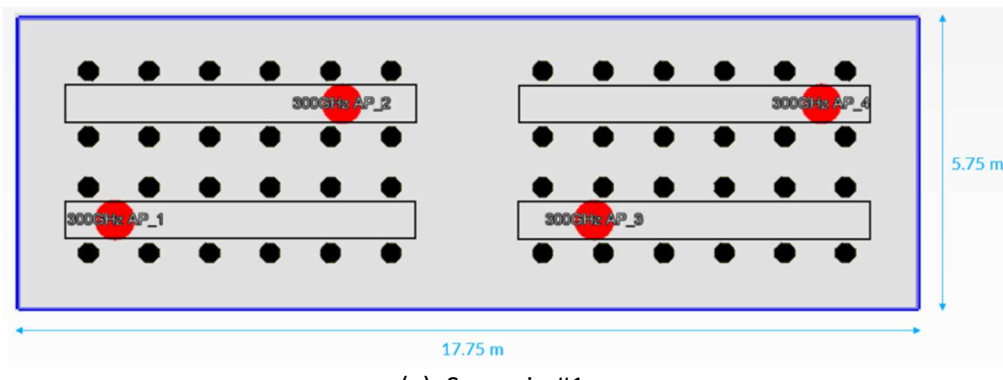
| Scenario | OOK #1 | P-QAM #1 | FSIM #1 | OOK #2 | P-QAM #2 | FSIM #2 |
|----------------------------|-----------------------------|----------|-----------------|---------|----------|-----------------|
| Carrier | 300 GHz | | | | | |
| Channel bandwidth | 2 GHz | | | | | |
| Number of channels | ≥ 1 | 1 | 1 | ≥ 1 | 1 | 1 |
| Tx power | 100 mW (20 dBm) per channel | | | | | |
| Tx/AP antenna gain | 14 dBi | | | | | |
| Rx /UE antenna gain | 5 dBi | | | 10 dBi | | |
| Rx/UE noise figure | 10 dB | | | | | |
| Phase noise | N/A | Medium | Medium | N/A | Medium | Medium |
| Margin | 10 dB | | | | | |
| Modulation scheme | OOK | P-QAM | FSIM | OOK | P-QAM | FSIM |
| SNR – Thrgt mapping | [9] | [4] | Section 2.3.3.3 | [9] | [4] | Section 2.3.3.3 |
| Min. required SNR | 0.98 dB | -0.81 dB | -5.03 dB | 0.98 dB | -0.81 dB | -5.03 dB |
| Coverage target | 95% | | | | | |
| MAPL * | 98.7 dB | 100.4 dB | 104.7 dB | 93.7 dB | 95.4 dB | 99.7 dB |
| Max range | 6.8 m | 8.3 m | 13.6 m | 3.8 m | 4.7 m | 7.6 m |

* MAPL = Maximum allowed Path Loss

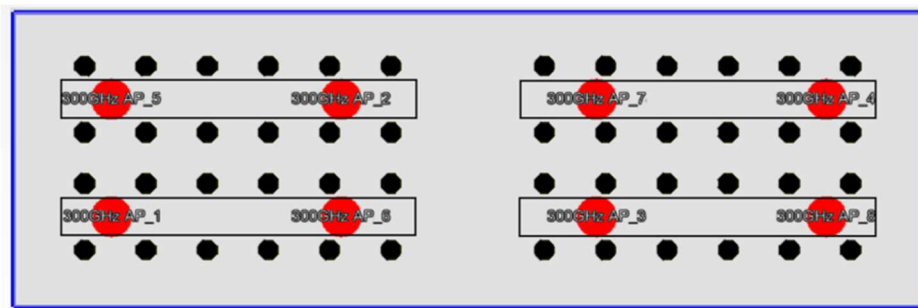
The received power and resulting SNR are calculated from the VolcanoFlex ray-tracing, with maximum two reflections and 1 diffraction allowed along a ray-path. The human bodies are represented by hexagonal parallelepipeds; they are considered as opaque (i.e. no transmission) however rays may be diffracted at the top or sides. We did not compute any reflection or scattering due to the human bodies due to the lack of knowledge regarding such interactions at 300 GHz.

2.4.3 Simulation results

The scenario #1 (with 5 dBi receive antenna gain) does require the installation of four access points, while up to eight access points are needed in scenario #2 (with 0 dBi receive antenna gain), whatever the modulation scheme. See Figure 28.



(a) Scenario #1



(b) Scenario #2

Figure 28 : Access point deployments for the hotspot scenarios #1 and #2.

The resulting coverage is illustrated by heatmaps in Figure 29. The target connectivity is achieved everywhere above the table and in most of the hotspot area. Limited performance or even lack of connectivity is observed in areas obstructed by the human bodies; here the P-QAM and FSIM modulations does slightly outperform the OOK modulation because of a lower receiver sensibility.

Even if the same coverage target is achieved for both scenarios #1 and #2, we may notice a significant throughput difference in the close AP line-of-sight areas, where the better link budget of scenario #1 leads to greater throughputs. At the contrary, the coverage from denser scenario #2 may be viewed as more uniform.

The scales at the right of the heatmaps (Figure 29) give the correspondence between colours and throughputs for respectively OOK / 1 channel, OOK / 2 aggregated channels, P-QAM / 1 channel, and FSIM / 1 channel. A first important conclusion is that, whatever the deployed solution, the sub-THz hotspot system provides more than 0.5 Gbps everywhere along the table, where most devices are supposed to be located. Therefore, if the sub-THz link budget given in Table 12 (or equivalent) can be realized, the considered hotspot scenario is a feasible target. As a second conclusion, we observe that OOK with two channels provides almost same connectivity as the P-QAM modulation. Actually, the exact multiplicative factor between the required P-QAM bandwidth and OOK bandwidth is around 2.2. The lowest performance of the low-complexity OOK system can be easily counterbalanced by using more aggregated channels (remember the available spectrum is large) and twice (or $\times 2.2$) the total transmit power.

One limitation resides in the very poor performance or absence of connectivity in the shadowed areas, in particular behind human bodies. Specific mechanisms have to be enabled if a seamless coverage is expected, like dual-connectivity with a sub-6GHz frequency, antenna diversity at the user device, or higher AP density (together with coordinated multi-points i.e. COMP, distributed MIMO, or fast handover procedure).

As shown in the color scale, the FSIM modulation significantly outperforms the P-QAM modulation in terms of throughput. Also, due to a significantly better sensitivity, it could have provided same coverage with about half deployed APs.

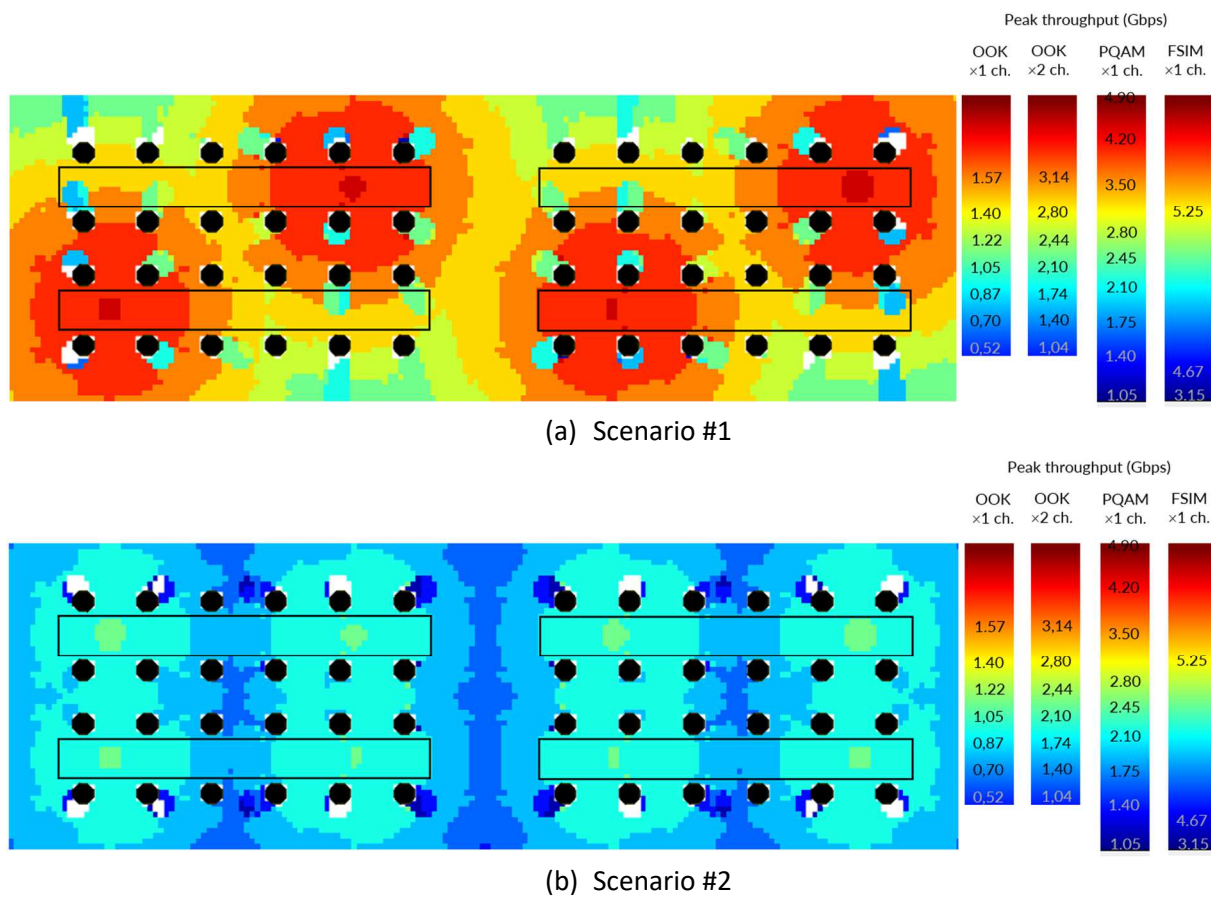


Figure 29 : Coverage heatmaps from the hotspot scenarios #1 and #2.

2.5 Scenario #5: Short-range D2D

In this section, we assess the performance of two schemes to address the KPIs of short range D2D scenario. On the one hand, a very low complexity non-coherent transceivers with energy detection is studied (based on demonstrator #1 [1]). On the other hand, we analyse the opportunity to consider coded coherent MIMO-FSIM for D2D (based on demonstrator #2 [1]).

2.5.1 Non coherent OOK transceiver with energy detection

2.5.1.1 System model

We consider in this section a communication system with N_t transmit antennas and N_r receive antennas. The propagation channel is described by two $N_r \times N_t$ matrices: H and Θ (the propagation gain and phase shift of the channel for signals transmitted). The transceiver uses envelope modulation at the transmitter and energy detection at the receiver as depicted in Figure 30. The aim of this work is to demonstrate the capability of a non-coherent MIMO using energy detectors in sub-THz bands to transfer Gbps. First, the design of the receiver detection algorithm was addressed. We derived a detector with Gaussian approximation corresponding to the studied nonlinear MIMO channel. Second, the communication performance is assessed through numerical simulations for uncoded and coded systems. We consider a realistic scenario modelling an indoor wireless link in D-band with directive antennas and strongly correlated line-of-sight channels.

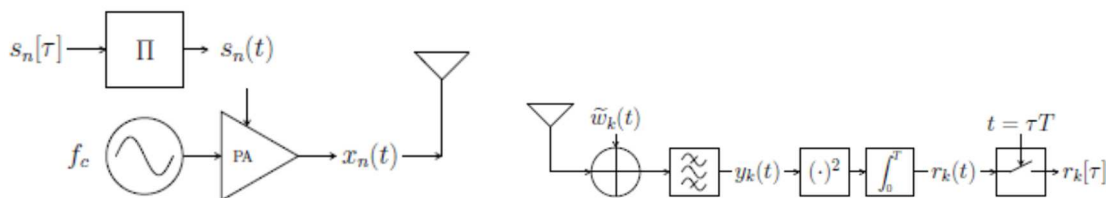


Figure 30 – Block diagram of the transmitter and receiver.

2.5.1.1 Performance assessments

We present the results of numerical simulations, conducted to assess the performance of MIMO systems using energy detectors in sub-THz bands. This task is addressed in two steps. First, we present a simplified performance analysis based on an analytical model, namely the sectored antenna model. Second, we consider the real radiation pattern of transmit and receive antennas and also the integration of a channel coding scheme. Thereby, the performance analysis is enhanced thanks to the system-level perspective and more realistic modelling.

2.5.1.1.1 MIMO case without spatial interference

To compare the different detectors, we first investigate MIMO systems without spatial interference. The channels are perfectly spatially multiplexed, i.e. H is diagonal. This case enables us to evaluate the performance of various detectors. To complete the scenario description, the modulation scheme used by the transceiver is On-Off Keying (OOK). Thereon, presents the results of numerical simulations for any systems with $N_t = N_r$. The performance of the detectors is expressed in terms of bit-error-rate (BER) as a function of the SNR.

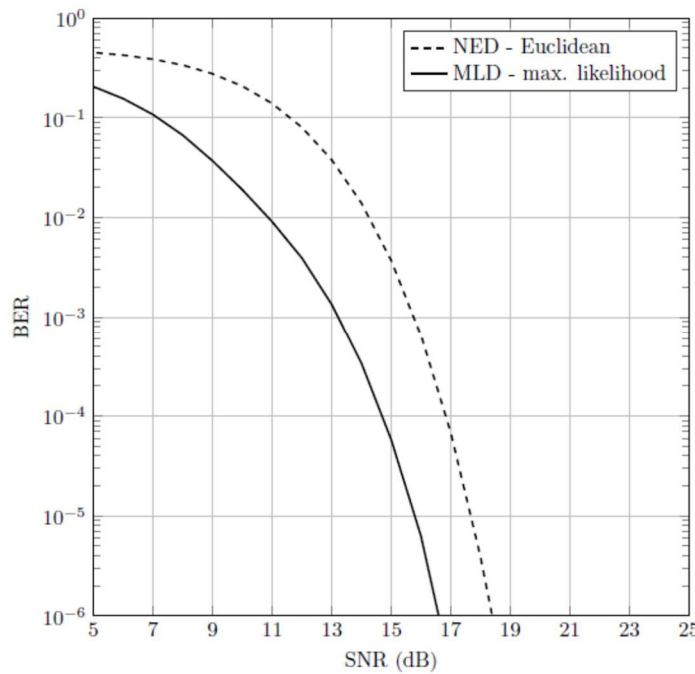


Figure 31 – Receivers performance for systems without spatial interference

The Gaussian approximation Maximum Likelihood Detector (MLD) outperforms the Naive Energy Detector (NED) based on the optimum decision rule defined by the standard Euclidean distance minimization (without knowledge of the noise statistic). The MLD capitalizes on the knowledge of the channel and therefore exhibits a detection gain.

2.5.1.1.2 Sectored antenna model

In this paragraph, we introduce a realistic sub-THz scenario. The targeted application is a fixed indoor high data rate wireless link in the D-band. Table 13 outlines the main simulation parameters for this scenario while Figure 32 illustrates its geometry. An $N_t \times N_r$ MIMO system is considered with uniform linear arrays of antennas whose disposition is depicted in Figure 32.

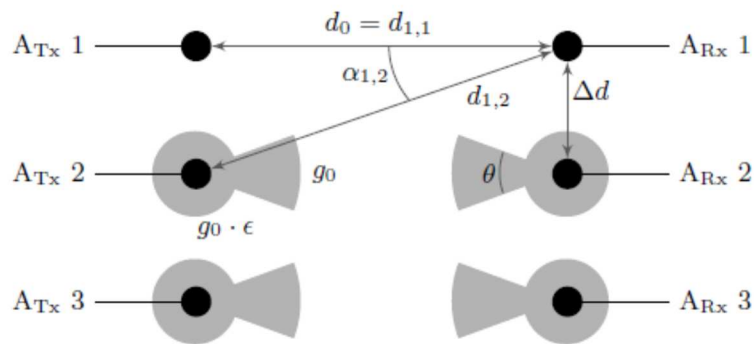


Figure 32 – Disposition of the antennas in the scenario

Table 13 : D2D simulation parameters.

| Parameters | Notation | Values |
|------------------------|--------------|-------------|
| Carrier frequency | f_c | 145 GHz |
| Bandwidth | $B = 2/T$ | 2 GHz |
| Thermal noise | N_0 | -174 dBm/Hz |
| Noise figure | N_f | 10 dB |
| Antenna gain | g_0 | 32 dBi |
| Beam width | θ | 3 ° |
| Side lobe level | ϵ | -20 dB |
| Distance Tx - Rx | d_0 | 10 m |
| Antenna transmit power | $P_{A_{Tx}}$ | - |

The specification of the antenna is extracted from [33] which describes the design of a high-gain antenna for the D-band with transmit-arrays and Printed Circuit Board (PCB) technology. The propagation gain may be evaluated from the budget link given by the Friis' transmission equation. We assume the commonly used sectored antenna model. The fixed antenna directivity gain is then defined by

$$g(\theta, \alpha) = g_0 \text{ if } |\alpha| < \frac{\theta}{2}, \epsilon \times g_0 \text{ otherwise}$$

upon the beam width θ , the beam offset angle to the main lobe α , the side lobe level ϵ and the antenna gain g_0 . The considered scenario is symmetric and the beam of the k th transmit antenna is aligned with the k -th receive one. k . Eventually, the channel matrix H may be evaluated. The maximum propagation gain is achieved for any channel $k \rightarrow k$. For an antenna transmit power $P_{A_{Tx}} = -30$ dBm, we have a SNR of 16.23dB. The interference terms (off-diagonal elements) in matrix H are approximately -0.01 dB, if $|\alpha| < \frac{\theta}{2}$ and -40.02 dB, otherwise. It should be mentioned that the differences in path loss between channels are close to zero (< 0.02 dB for $N = 8$) when $N_t = 8$. Subsequently, the interference level between two channels only results from the sector of the antennas. Under the condition $\Delta d \geq d_0 \tan\left(\frac{\theta}{2}\right)$, the antennas are almost perfectly spatially multiplexed as the interference follows from side lobes of the antennas, and hence, is very low (< -40 dB). This corresponds closely to an ideal case and the performance of the transceivers for any N equals the one described by the MIMO case without spatial interference. Nevertheless, the latter condition entails a large spatial occupation, the width of the receiver and the transmitter, since in our case $\Delta d > 26$ cm. Considering a uniform linear array of 8 antennas, we have the antenna array size is 1.8 m. We thus consider in the case where one antenna beam enlightens several receive antennas to reduce Δd and hence the spatial occupation.

We therefore, consider the condition $\Delta d \geq \frac{2}{\kappa+1} d_0 \tan\left(\frac{\theta}{2}\right)$, defined upon parameter $\kappa \in \{1, 3, \dots, 2N-1\}$. From a physical aspect, this condition expresses the case where one transmit antenna beam enlightens up to κ receive antennas. By way of illustration, the channel propagation gain matrix for $\kappa = 3$ could be accurately approximated by

$$H = \begin{bmatrix} 1 & 1 & \rho & \dots & \rho \\ 1 & 1 & 1 & \ddots & \vdots \\ \rho & 1 & 1 & \ddots & \rho \\ \vdots & \ddots & \ddots & \ddots & 1 \\ \rho & \dots & \rho & 1 & 1 \end{bmatrix}.$$

This matrix is defined by two parameters: κ denoting the number of diagonals whose elements are 1 and ρ modelling the residual interference due to side lobes of the antennas with $\rho^2 = -40$ dB. Let us now evaluate the influence of κ on communications through numerical simulations. In these simulations, the propagation gain and phase shift matrices are not approximated and are exactly computed from the scenario description and simulation parameters. The results of numerical simulations are depicted in Figure 33. The BER performance is outlined for $N = 8$ and different values of κ . The properties exhibited also hold for different values of N .

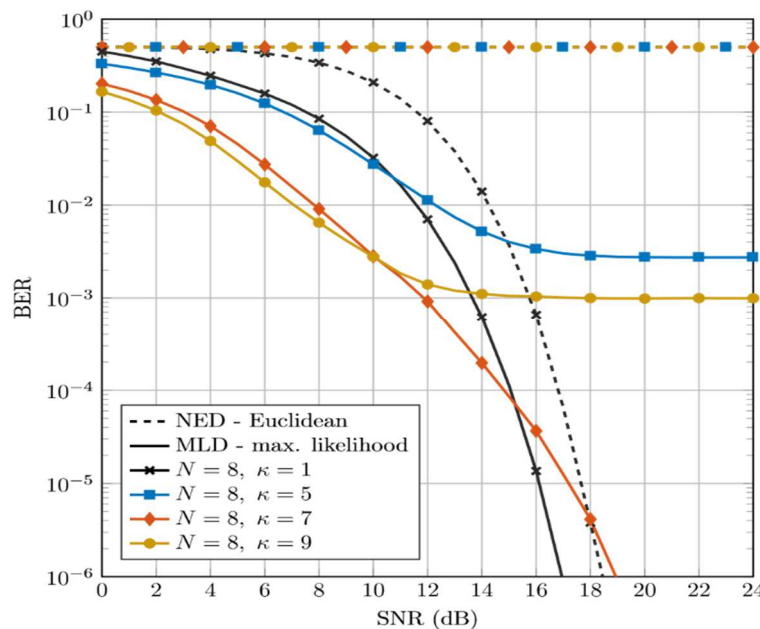


Figure 33 – Influence of κ on performance for $N = 8$

First, it must be noted that the MLD is essential to communicate on correlated channels with spatial interference since the NED presents a BER of $1/2$ for any $\kappa > 1$. Further, it is shown that setting $\kappa = 1$ is optimal, yet $\kappa = N - 1$ is an interesting choice to achieve low error rate communications with a reduced spatial occupation. Simulation results also show that, in the moderate SNR regime, transceivers with high values of κ may demonstrate lower BER than the optimal case $\kappa = 1$. With channel coding, such property may be beneficial for configurations with κ large. If the BER is low enough, the waterfall feature of the decoding algorithm may be exhibited at a lower SNR.

2.5.1.1.3 Real antenna radiation pattern

Previously, we have based the performance analysis upon the commonly used sectored antenna model. The sectored model is relevant for its simple analytic expression. However, the accuracy of the analysis can be improved by considering the real antenna gain pattern measured and published in [33].

Figure 34 depicts the real antenna gain pattern and the sectored model. The assessment of communication performance with the real antenna gain, in comparison to the sectored model, is also presented in Figure 34 for $N_t = 8$ using the Maximum Likelihood Detector with Gaussian Approximation MLD-GA and a neural network detector (NND).

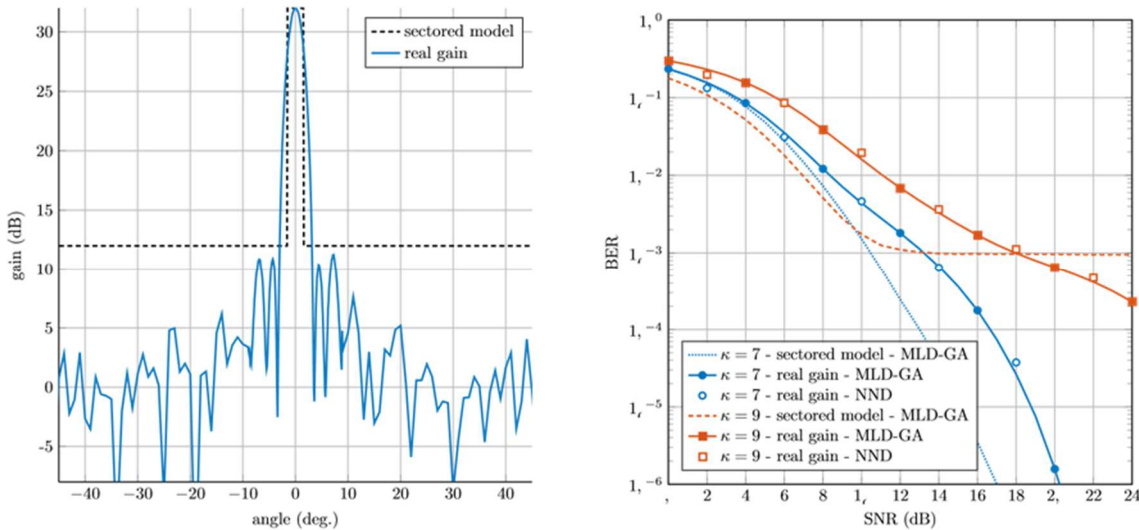


Figure 34 – Antenna gain measured and performance comparison

It can be observed that the BER performance of system configurations with strong interference is deteriorated when the real antenna gain is considered. Nevertheless, and conversely to the sectored model, no error floor is observed with the real antenna pattern, see the configuration $N_t=8$, $\kappa=9$. In addition, it should be emphasized that the MLD-GA and the NND demonstrate similar demodulation performance when considering the real antenna gain. We conclude from these results that the sectored antenna gain model is an efficient but optimistic model to describe practical systems. In the following, any further performance analysis is based on the real radiation pattern of the antenna gain.

2.5.1.1.4 Integration of channel coding

It is interesting to consider the integration of a Forwarded Error Correction (FEC) scheme to achieve channel coding gain and low error rates. However, implementing the FEC, and in particular its decoder, may entail a significant complexity and power consumption. To achieve a low-complexity low-power transceiver, we propose here to use a BCH code. The considered FEC scheme is a BCH code with a packet size of 63 bits, a coding rate ranging from 0.1 to 1 and a decoder based on hard decisions. It should be mentioned that the key features of this code are a low-complexity implementation and a low-power consumption – interested readers may refer to [34]. In addition, with regard to the short packet size, this code has a low-latency decoder. These features appear to be highly relevant for the scenario investigated in this study. The considered transceiver architecture with the integration of channel coding is presented in Figure 35.

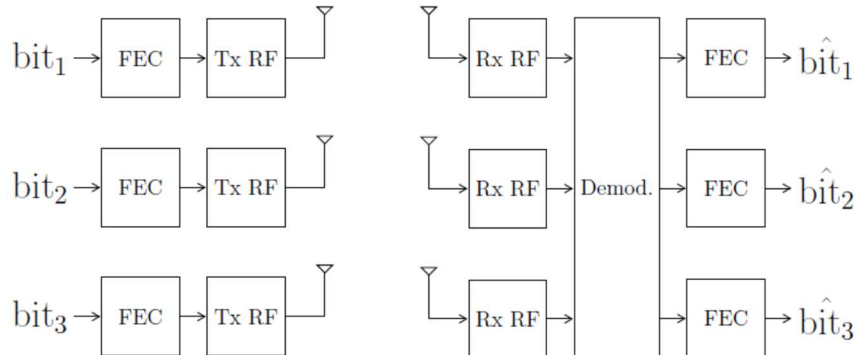


Figure 35 – System architecture integrating a FEC scheme

Multiple FEC schemes are used and the coding rate can be adapted to the channel quality of the receive antenna. The channel presents significant differences in terms of quality depending on the receive antenna. Receive antennas in the middle of the Uniform Linear Array (ULA) are subject to stronger interference than the ones on the extremities. For this reason, adapting the coding rate to the receive antenna enables us to capitalize on the latter property to further enhance the demodulation performance. The system architecture in Figure 35 is particularly interesting as it also maintains a high degree of parallelism. Conversely, using a unique FEC is not an efficient solution to define a parallel implementation and to optimize the coding rate to the transmit-receive antennas.

Figure 36 presents the achievable rates as function of E_b/N_0 for systems with a BCH code such that the BER is below 10^{-6} . The BCH code is implemented with a coding rate ranging from 0.4 to 1 and a channel decoder based on the hard decisions produced by the MLD. Numerical results have been obtained through the Monte-Carlo simulations with the real antenna gain pattern. First, it should be remarked that integrating a FEC scheme enables to achieve valuable channel coding gains. Second, it can be remarked that the adaption of the coding rate to the antenna leads to performance gains in comparison to setting a fixed coding rate for all antennas. In particular, we can see that for $N_t = 4$ and $N_t = 6$ the performance gains are larger than 2 dB.

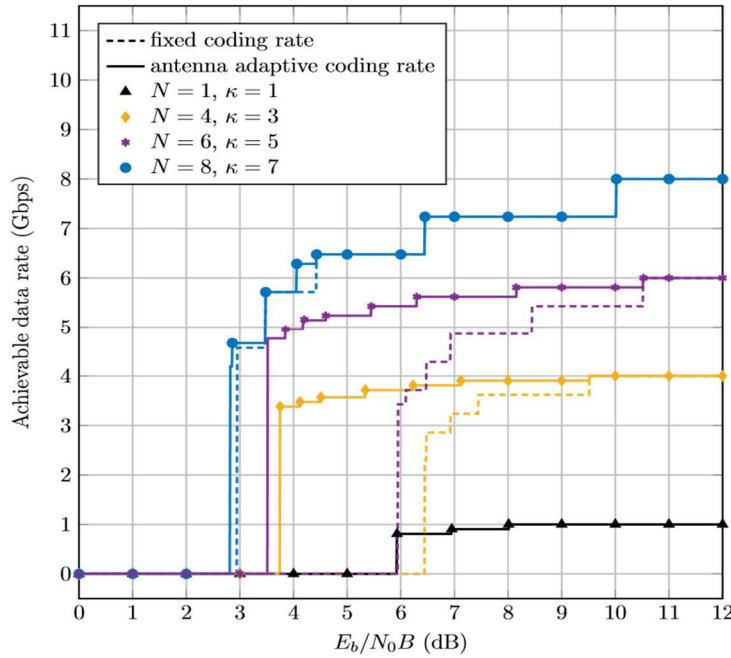


Figure 36 –Achievable data rate with a BCH code and the real antenna gain

To present the results of Figure 36 differently, we propose in Table 14 a synthesis of the system performance and parameters for different number of antennas. For all system configurations, the bandwidth is $B = 2$ GHz, the distance Tx-Rx is $d_0 = 10$ m, and the coding rate of the BCH is 0.9. Though the system performance is evaluated with the MLD. Further, a channel bonding scheme, aggregating several sub-bands, could increase the throughput and allow to benefit from the large spectrum available in sub-THz bands. It can be concluded that MIMO systems using energy detection receivers may achieve high-rate communications in sub-THz bands with low-power and low-complexity RF architectures. Performance of coded systems could be further improved by considering longer packet length, soft-decision channel decoding, or capacity-achieving codes – e.g. a polar code – yet at the detriment of a complexity increase.

Table 14 : Synthesis of the main system parameters and key performance indicators.

| | | | | | |
|-------------------------------|-----------------|-------------|-----------|-----------|-----------|
| Carrier frequency | f_c | 145 GHz | | | |
| Bandwidth | B | 2 GHz | | | |
| Propagation distance | d_0 | 10 m | | | |
| Antenna gain | g_0 | 32 dBi | | | |
| Number of antennas | N | 1 | 4 | 6 | 8 |
| Throughput | $N/T \cdot 0.9$ | 0.9 Gbps | 3.6 Gbps | 5.4 Gbps | 7.2 Gbps |
| Power by antenna | $P_{A_{Tx}}$ | -31.8 dBm | -31.2 dBm | -30.4 dBm | -32.3 dBm |
| Width of the ULA | ℓ | 5 cm | 44 cm | 50 cm | 55 cm |
| Inter-antenna distance | Δd | \emptyset | 13 cm | 9 cm | 7 cm |

2.5.1.2 Conclusion

This field of research has gained interest with regard to the future deployment of spectral-efficient links in the mm-Wave bands. Though the design paradigms are considerably different since we target low-complexity implementations, some design issues are shared. Using coherent or non-coherent transceivers, in both cases the use of ULA of antennas is considered and geometric approaches are developed. Moreover, the system performance is directly linked to the antenna separation in any cases. In LoS environments with sparse channels, multiplexing and detecting several signal streams with MIMO systems is challenging due to the correlation among channels. And with regards to the previous deliverable, phase impairments entail severe consequences on the design of coherent LoS MIMO systems. Oscillator instabilities render difficult the implementation of beamforming but also of precoding and detection. For these reasons, the design of coherent LoS MIMO systems in sub-THz frequencies could be relevant to further increase the spectral efficiency, still numerous design problematics are yet to be addressed in addition to state-of-the-art techniques and existing literature. Increasing the communication throughput is one of the main challenges of using non-coherent transceivers in sub-THz bands. In this work, we have shown that spatial multiplexing is an efficient method to implement large communication throughputs with low-complexity sub-THz systems.

2.5.2 Coded coherent MIMO SMX-FSIM for D2D

The system model for MIMO SMX-FSIM is well detailed in [4] and [24] while its coded version is presented in Section 2.3.3.2. After the different advantages highlighted in hotspot and enhanced WLAN in section 2.3.2, the SISO/MIMO FSIM scheme is also considered for D2D scenario.

2.5.2.1 Coded FSIM performance assessments

For the D2D scenario, a sectored antenna model is considered as described in Section 2.5.1.1.2. This scenario is also studied with the proposed FSIM scheme over none and medium phase noise levels with LDPC coding of rates = [3/5, 8/9] and compared to its uncoded version.

For the first simulation shown in Figure 37, a 4x4 MIMO-FSIM system is considered with $\kappa = 3$. It is noticed that for an uncoded FSIM, the phase noise has a higher effect on the BER as the medium PN curve diverges from the no PN. While on the other side, it is clear that LDPC coding diminishes the effect of phase noise that has small effect on FSIM compared to other schemes as shown in Figure 21.

As for the second simulation shown in Figure 38, a 6x6 MIMO-FSIM system is considered with $\kappa = 5$. Here the conclusion of the previous simulation result is clearer and more confirmed. As the uncoded results diverge and the medium PN case reaching an error floor, the coded FSIM with both used coding rates has a BER of similar behavior for both PN cases with a small advantage for no PN case.

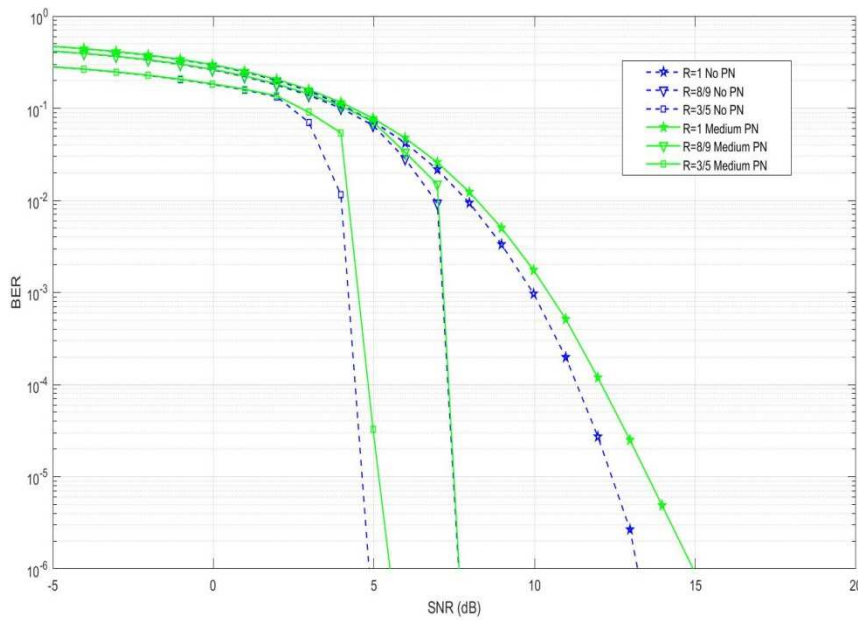


Figure 37: BER performance of coded FSIM vs Uncoded FSIM using $K=3$ $N_t=4$ $R=1,8/9,3/5$

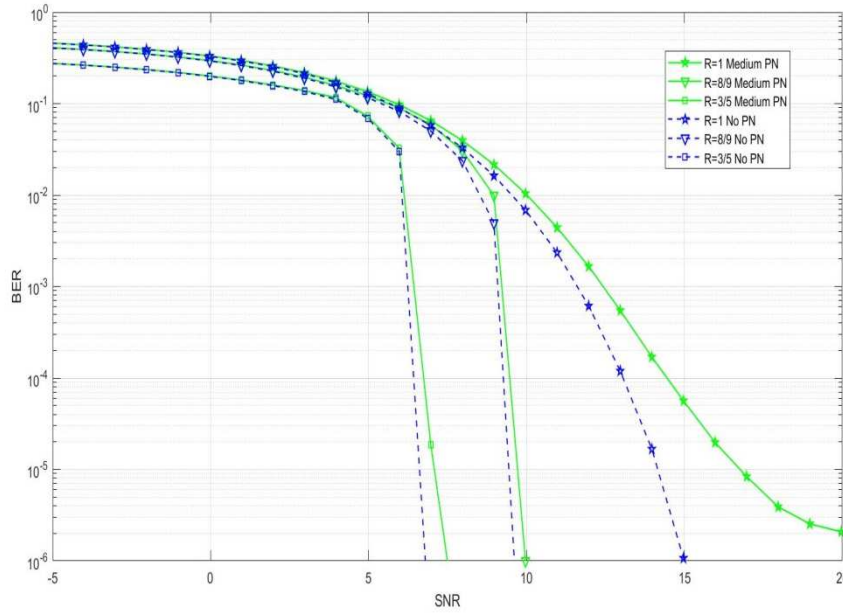


Figure 38: BER performance of coded FSIM vs Uncoded FSIM using $K=5$ $N_t=6$ $R=1,8/9,3/5$

A set of various configurations for the D2D scenario as different number of antennas as: 1x1, 4x4, 6x6, and 8x8; Also considering uncoded and coded systems with rates of 2/5, 3/5, and 8/9, along with none and medium phase noise. Recalling that low order modulation as QPSK is preferred due to its robustness to phase noise and low PAPR that allows operating the PA at higher efficiency as highlighted in previous sub-section.

From this set of configurations, the achievable spectral efficiency is deduced for each given SNR as depicted in Figure 39. The highest spectral efficiency with 8x8 MIMO-FSIM using N=2 and QPSK is 24 bpcu meaning that with a bandwidth of 2 GHz it leads up to 48 Gbps throughput with a low SNR requirement even with PN. For instance, this system with channel bounding of 12.5 GHz leads to a rate in order of 266 Gbps with medium PN level up to 300 Gbps without PN, while the channel aggregation of the 48 GHz bandwidth in sub-THz bands leads to 1.024 Terabits per second (Tbps) with medium PN and up to 1.152 Tbps without PN.

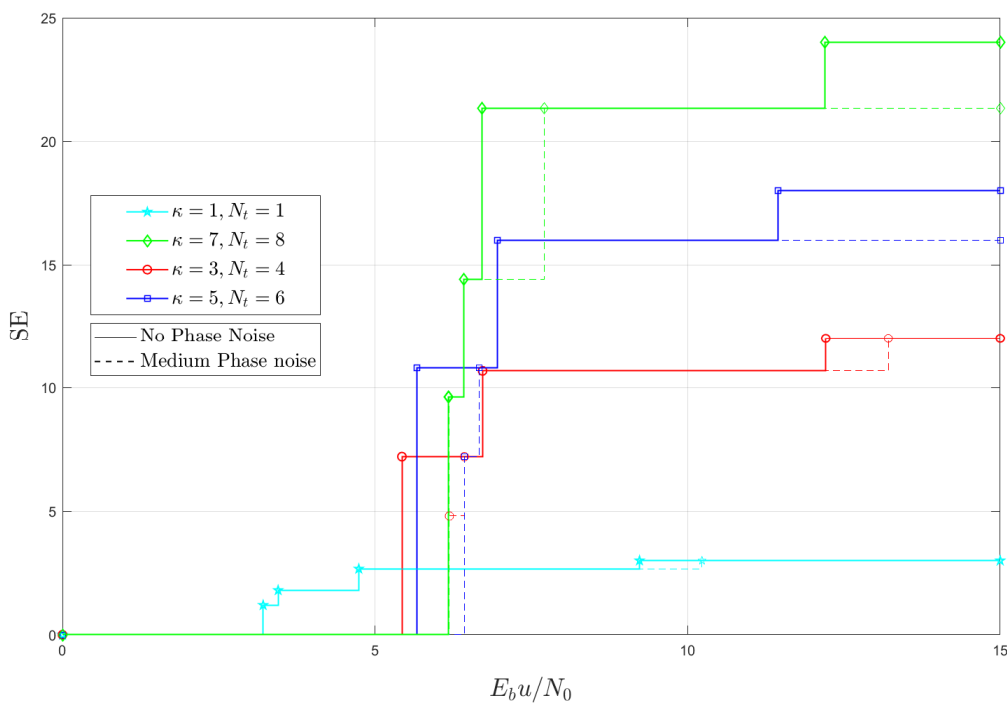


Figure 39: Achievable Spectral efficiency for D2D scenario with/without phase noise based on $BER = 10^{-6}$.

2.5.2.2 Link budget for coded FSIM

After highlighting the achievable throughput with the proposed SMX-FSIM system using different bandwidth, it is necessary to estimate the link budget and the required transmit power. The link budget of FSIM using 2 filter shapes and QPSK along with LDPC channel coding with a rate of 8/9 is evaluated with different number of transmitter/receiver antennas in D2D scenario subjected to medium phase noise. The estimation is done based on four different antenna configurations: 1, 4, 6, and 8 while using same number of antennas at transmitter and receiver side. The link budget and required transmit power shown in Table 15 is calculated from the required SNR to guarantee a BER below 10^{-6} and while using same parameters like in Table 13 and Table 14. It is shown that the scheme needs low SNR levels to operate based on starting from a SISO transmission having a maximum throughput of 5.33 Gbps, and up to 42.67 Gbps when using 8x8 MIMO with a bandwidth of 2GHz while conserving a very low required transmit power per antenna even for medium phase noise environment. Finally, it is worth highlighting that OOK is a very suitable for extremely low-complexity receivers especially when there

is a very strong phase noise impairment, but the coded FSIM is very advantageous when a quadrature-based transceiver is affordable for the considered application because FSIM allows to reach much higher spectral efficiency and therefore higher throughput with a low transceiver complexity, cost and very limited transmit power like MIMO-OOK. In addition, it is clear that SMX-FSIM allows to minimize the transceiver cost related to number of RF chains and antennas to achieve any spectral efficiency as shown in Figure 18 and Figure 19.

Table 15: Link budget for the proposed SISO/MIMO FSIM scheme in D2D scenario with medium phase noise level.

| Number of antennas | 1 | 4 | 6 | 8 |
|-----------------------------------|---------------|---------------|---------------|---------------|
| Maximum SE (bpcu) | 2.67 | 10.67 | 16.00 | 21.33 |
| Maximum throughput (Gbps) | 5.33 | 21.33 | 32.00 | 42.67 |
| Required SNR (dB) | -0.03 | 7.97 | 9.97 | 11.97 |
| Rx Noise Figure (NF) | | 10.00 | | |
| Thermal Noise (Nthermal) | | -80.92 | | |
| Noise floor | | -70.92 | | |
| Rx Signal Level (RSL) | -70.95 | -62.95 | -60.95 | -58.95 |
| Rx Antenna Gain (Gr) | | 32 | | |
| Free space path loss (fspl) | | 95.67 | | |
| Required Tx EIRP | -7.27 | 0.73 | 2.73 | 4.73 |
| Tx Antenna Gain (Gt) | | 32 | | |
| Required Transmit Power Pt | -39.27 | -31.27 | -29.27 | -27.27 |

2.5.2.3 Conclusion

All the results prove that FSIM scheme is a very promising solution for low-power ultra-high data rates due to several advantages like high SE/EE, robustness to phase noise level, and low cost. To conclude, it is worth mentioning that the proposed reconfigurable FSIM system allows to deal with different end-user's requirements, where the MIMO FSIM transmitter can be reconfigured: as OOK if needed to communicate with an extremely low complexity receiver devices; as FSIM with APM modulation for higher wireless data rates at a low transceiver cost and an affordable complexity for most user equipment.

3 Conclusion

These cases study allowed us to quantify the potential of the sub-THz spectrum in six scenarios. It has been demonstrated 6 important results:

1. A FWA network with higher data rates than possible today looks feasible based on 150 GHz devices, even if the transmit power is limited to 100 mW, but assuming antenna gains up to 32 dBi. A full coverage target may be very costly at such high frequency. Thus it looks like a better approach to design the D-band network for a reasonable coverage objective, and then complement with additional connections in a lower frequency band.
2. Wireless backhauling is obviously a promising application for sub-THz frequencies in order to feed dense access networks in suburban, urban or large venue environments with capacities greater than 1 Gbps per node. Nevertheless, the propagation constraints oblige for careful network design and development of accurate radio-planning solutions to minimize the number of nodes and hops to be deployed.
3. The different analyses reveal that index modulation and SMX FSIM, in the sub-THz context, offer very good performance, low transceiver cost, high SE/EE gain and low power consumption. The most promising candidate MIMO FSIM demonstrated its superiority compared to equivalent system of same SE; it was shown that 8x8 MIMO-FSIM using only 2 filter shapes and low-order modulation as QPSK with LDPC code and a linear low complexity receiver is able to reach an ultra-high data rate in order of Tbps at low SNR; this coded system has a negligible degradation even with medium PN level. The reconfigurable FSIM scheme is also particularly interesting for D2D scenario.
4. The use of very low-cost transceiver based on LDPC coded OOK and energy detector at 300GHz are of particular interest to cover a small hotspot area and for delivering 1+Gbps. While considering coherent MIMO FSIM system allows delivering 10+ Gbps up to Tbps while achieving better SE/EE results at a lower number of RF chains. However, these advantages of MIMO FSIM come with an affordable linear increase in computational complexity.
5. Last, we demonstrated the feasibility of coherent and non-coherent MIMO in a strongly correlated channel for very short-range D2D applications. Despite the inherent correlated nature of the radio channel, the design of a joint antenna detector leads to very good performance and low power consumption to achieve 1+Gbps per channel.

All these results show that sub-THz technologies are relevant candidates for the next generation of wireless networks. However, the road is long and some technologies still need to be improved. Part of them include large gain antenna with beamsteering capabilities, high power amplifier design with high power efficiency, digital processor to manage very high throughput and last but not least cost-effective solutions.

4 References

- [1] Y. Corre, G. Gougeon, J.-B. Doré, S. Bicaïs, B. Miscopein, E. Faussurier, M. Saad, J. Palicot and F. Bader, "Sub-THz spectrum as enabler for 6G wireless communications up to 1 Tbit/s," *6G Wireless Summit*, 2019.
- [2] M. Saad, C. F. Bader, J. Palicot, Y. Corre, G. Gougeon and J.-B. Doré, BRAVE deliverable D1.0: Beyond-5G wireless Tbps Scenarios and Requirements, 2018.
- [3] BRAVE, deliverable D2.1; Propagation channel model and RF impairments definition and waveform design, Nov. 2020.
- [4] M. Saad and F. Bader, "D2.1-addendum: Waveform Design for low-power ultra-high data rate systems," BRAVE Technical deliverable D2.1-addendum, 2021.
- [5] BRAVE, deliverable D3.0; Interface specification, June 2020..
- [6] N. Rajatheva, White paper on broadband connectivity in 6G, June 2020..
- [7] Y. Corre, M. Z. Aslam, S. Bicaïs, J-B. Doré, G. Gougeon, "Assessment of sub-THz Mesh Backhaul Capabilities from Realistic Modelling at the PHY Layer," *14th European Conference on Antennas and Propagation (EuCAP)*, 2020.
- [8] Y. Corre, M. Z. Aslam, "Simulated Propagation Properties for Future Outdoor sub-THz Networks," *IEEE PIMRC 2020, Workshop on "Enabling Technologies for THz Communications*, 2020.
- [9] J.-B. Doré, G. Goudeon, Y. Corre, S. Bicaïs, "Optimized Single-Carrier Transceiver For Future Sub-TeraHertz Applications," *ICASSP 2020*, 2020.
- [10] B. Marques, "Automated Joint Access and Backhaul Planning for 5G Millimeter-Wave Small Cell Networks," *IEEE WPMC 2020*, 2020.
- [11] BRAVE, deliverable D2.0; Propagation channel model and RF impairments definition, Feb. 2019.
- [12] J.-B. Doré, S. Bicaïs, "Design of Digital Communications for Strong Phase Noise Channels," *IEEE Open Journal of Vehicular Technology*, 2020.
- [13] M. W. M. R. J. C. Ikuno, "System Level Simulation of LTE Networks," *IEEE 71st Vehicular Technology Conference*, 2010.
- [14] M. Saad, F. Bader, J. Palicot, A. C. Al Ghouwayel and H. Hijazi, "Single Carrier with Index Modulation for Low Power Terabit Systems," in *2019 IEEE Wireless Communications and Networking Conference (WCNC)*, Marrakech, Morocco, 2019.

- [15] M. Saad, A. C. Ghouwayel, H. Hijazi, F. Bader and J. Palicot, "MIMO techniques for wireless Terabits systems under sub-THz channel," *IEEE International Conference on Communications Workshops*, pp. 1-6, 2020.
- [16] M. Saad, N. Bouhlel, C. F. Bader, S. Bicais, J.-B. Doré, Y. Corre and M. Z. Aslam, "D2.1: Design, Propagation channel model and RF impairments definition and waveform," BRAVE Technical deliverable D2.1, 2020.
- [17] J. T. Wang, S. Y. Jia and J. Song, "Generalised spatial modulation detection scheme," *IEEE Transactions on Wireless Communications*, vol. 11, no. 4, pp. 1605–1615,, 2012.
- [18] J. Jeganathan, A. Ghrayeb, L. Szczecinski and A. Ceron, "Space shift keying modulation for MIMO channels," *IEEE Transactions on Wireless Communications*, vol. 8, no. 7, p. 3692–3703, 2009.
- [19] J. Jeganathan, A. Ghrayeb and L. Szczecinski, "Generalized space shift keying modulation for MIMO channels," *IEEE 19th International Symposium on Personal, Indoor and Mobile Radio Communications*, p. 1–5, 2008.
- [20] R. Y. Mesleh, H. Haas, S. Sinanovic, C. W. Ahn and S. Yun, "Spatial Modulation," *IEEE Transactions on Vehicular Technology*, vol. 57, no. 4, p. 2228–2241, Jul. 2008.
- [21] M. Saad, F. C. Lteif, A. C. A. Ghouwayel, H. Hijazi, J. Palicot and F. Bader, "Generalized spatial modulation in highly correlated channels," *IEEE 30th International Symposium on Personal, Indoor and Mobile Radio Communications (PIMRC Workshops)*, p. 1–6, 2019.
- [22] N. Bouhlel, M. Saad and F. Bader, "Sub-Terahertz Wireless System using Dual-Polarized Generalized Spatial Modulation with RF Impairments," *IEEE Journal on Selected Areas in Communications*, vol. 39, no. 6, pp. 1636-1650, Jun. 2021.
- [23] M. Saad, J. Palicot, F. Bader, A. C. A. Ghouwayel and H. Hijazi, "A Novel Index Modulation Dimension based on Filter Domain: Filter Shapes Index Modulation," *IEEE Transactions on Communications*, 2020.
- [24] M. Saad, N. A. Akkad, H. Hijazi, A. C. Al Ghouwayel, F. Bader and J. Palicot, "Novel MIMO Technique for Wireless Terabits Systems in sub-THz Band," *IEEE Open Journal of Vehicular Technology*, vol. 2, pp. 125-139, Jan. 2021.
- [25] J. Wang, S. Jia and J. Song, "Generalised Spatial Modulation System with Multiple Active Transmit Antennas and Low Complexity Detection Scheme," *IEEE Trans. Wireless Commun*, vol. 11, no. 4, pp. 1605-1615, 2012.
- [26] S. Bicais and J.-B. Dore, "Phase Noise Model Selection for Sub-THz Communications," *IEEE Global Communications Conference*, 2019.
- [27] G. Gougeon, Y. Corre and M. Aslam, "Ray-based Deterministic Channel Modelling for sub-THz Band," *IEEE International Symposium on Personal Indoor and Mobile Radio Communications (PIMRC)*, 2019.

- [28] M. Saad, F. Bader, A. C. A. Ghouwayel, H. Hijazi, N. Bouhel and J. Palicot, "Generalized spatial modulation for wireless Terabits systems under sub-THz channel with RF impairments," *IEEE International Conference on Acoustics, Speech and Signal Processing (ICASSP)*, p. 5135–5139, 2020.
- [29] M. Tanahashi and H. Ochiai, "Symbol Insertion: A Low-Complexity Joint Peak Power Reduction and Forward Error Correction for Single-Carrier Systems," *IEEE Transactions on Communications*, vol. 58, no. 11, pp. 3244–3253, November 2010.
- [30] E. Basar, "Multiple-input multiple-output OFDM with index modulation," *IEEE Signal Processing Letters*, vol. 22, no. 12, p. 2259–2263, 2015.
- [31] M. R. Khanzadi, D. Kuylensierna, A. Panahi, T. Eriksson and H. Zirath, "Calculation of the performance of communication systems from measured oscillator phase noise," *IEEE Transactions on Circuits and Systems I: Regular Papers*, vol. 61, no. 5, p. 1553–1565, 2014.
- [32] S. Li, D. Fritzsche, C. Carta and F. Ellinger, "A 200-GHz sub-harmonic injection-locked oscillator with 0-dBm output power and 3.5 DC-to-RF- efficiency," in *Proc. IEEE Radio Freq. Integr. Circuits Symp.*, Jun. 2018.
- [33] F. F. Manzillo, A. Clemente and J. L. Gonzalez-Jimenez, "High-gain D-band Transmitarrays in Standard PCB Technology for Beyond-5G Communications," *IEEE Transactions on Antennas and Propagation*, vol. 68, no. 1, pp. 587–592, Jan. 2020.
- [34] C. Fougstedt, K. Szczerba and P. Larsson-Edefors, "Low-Power Low-Latency BCH Decoders for Energy-Efficient Optical Interconnects," *Journal of Lightwave Technology*, vol. 35, no. 23, p. 5201–5207, 2017.
- [35] L. He, J. Wang and J. Song, "Extended spatial modulation scheme with low complexity detection algorithms," *International Wireless Communications and Mobile Computing Conference (IWCMC)*, p. 582–587, Aug. 2014.
- [36] M. Nakao, T. Ishihara and S. Sugiura, "Single-carrier frequency domain equalization with index modulation," *IEEE Communications Letters*, vol. 21, no. 2, p. 298–301, Feb. 2017.
- [37] T. Ishihara and S. Sugiura, "Faster-than-nyquist signaling with index modulation," *IEEE Wireless Communications Letters*, vol. 6, no. 5, p. 630–633, Oct. 2017.
- [38] D. Tsonev, S. Sinanovic and H. Haas, "Enhanced subcarrier index modulation (SIM) OFDM," *IEEE GLOBECOM Workshops (GCC Wkshps)*, p. 728–732, 2011.
- [39] R. Fan, Y. J. Yu and Y. L. Guan, "Generalization of orthogonal frequency division multiplexing with index modulation," *IEEE Transactions on Wireless Communications*, vol. 14, no. 10, p. 5350–5359, October 2015.
- [40] E. Basar, U. Aygolu, E. Panayirci and H. V. Poor, "Orthogonal frequency division multiplexing with index modulation," *IEEE Transactions on Signal Processing*, vol. 61, no. 22, p. 5536–5549, 2013.

- [41] M. Nakao and S. Sugiura, "Spectrally efficient frequency division multiplexing with index-modulated non-orthogonal subcarriers," *IEEE Wireless Communications Letters*, vol. 8, no. 1, p. 233–236, 2019.

5 Appendices

5.1 Appendix A: Open Data

Some datasets that were simulated during BRAVE investigations have been uploaded to an open repository that is freely accessible on BRAVE website. This data is thought to be useful for research and engineering teams aiming at realistic PHY-layer simulations at sub-THz frequencies.

5.1.1 Point-to-point backhaul performance data

The data uploaded on the open repository is a set of multipath channel samples predicted at 150 GHz by the SIRADEL ray-tracing (VolcanoUrban) on the urban scenario described in Appendix B. A group of 134 lampposts in this area is considered as virtual sub-THz device positions. All possible lamppost-to-lamppost links with range lower than 200 meters are computed, leading to a total of 1873 predicted links to be used for a statistical analysis of received power, SNR, peak throughput depending on link length and type of obstruction (LoS, NLoS, OLoS). A 25 dBi antenna gain at both terminals is considered and aligned towards the strongest ray path of the link.

Data are stored in a MATLAB file including a sparse 134x134 cell matrix in which each row/column correspond to a lamppost. Cells are empty if the associated link has a length greater than 200 meters, or if the reciprocal link is already reported in appropriate cell. Each cell contains the following data:

- Lampposts coordinates;
- Link length;
- Type of obstruction;
- Ray path characteristics (angle of departure, angle of arrival, delay, strength);
- Received power;
- SNR
- Peak throughput obtained with the P-QAM modulation under medium phase noise

A PDF document accompanies the MATLAB data file to further describe the scenario and give all information necessary for their exploitation.

5.1.2 MIMO channel samples for kiosk scenario

The data uploaded on the open repository is a set of MIMO channel samples that were predicted at 150 GHz by the SIRADEL ray-tracing (VolcanoFlex).

The sub-THz kiosk aims at downloading huge data rates; thus, we consider here the kiosk antenna as the “transmitter” and the user equipment as the “receivers”. The simulated scenario is composed of a fixed kiosk transmitter located in a wide indoor avenue in a shopping mall. More precisely, the kiosk transmitter is in the middle of a large patio, facing an intersection between two avenues; the transmitter vicinity may be considered as “open”, as shown in Figure 40. The simulated receivers are distributed over the surface of half a disk in front of the kiosk transmitter with radius 10 m. Figure 41 (right) illustrates the various receiver positions that have been predicted, with a specific antenna orientation at each position i.e. towards the kiosk. All receiver positions are in line-of-sight (LoS).

The transmitter and receivers have each an antenna array of rectangular shape, composed of dual-polar antenna elements (either V/H or +/-45° linear polarizations at the transmitter, and V/H polarizations at the receiver). The size of the transmit antenna array is (16 x 8) x 2 polarizations. The size of the receive antenna array is (8 x 8) x 2 polarizations.

The channel properties are simulated for a central frequency of 150 GHz, and a channel bandwidth of 2 GHz divided into 20 sub-carriers.

The channel H matrix between the transmitter and all receivers is saved into a MATLAB file. For each receiver, the H matrix is formed of $128 \times 64 \times 20 = 163\,840$ complex coefficients. One coefficient corresponds to the propagation channel gain between one transmit antenna element and one receive antenna element for a specific sub-carrier.

Note that if someone wants to get the H matrix for smaller antenna array, e.g. for a 8 x 8 MIMO system, and for a single frequency, then a relevant sub-matrix can easily be extracted from the full predicted matrix.

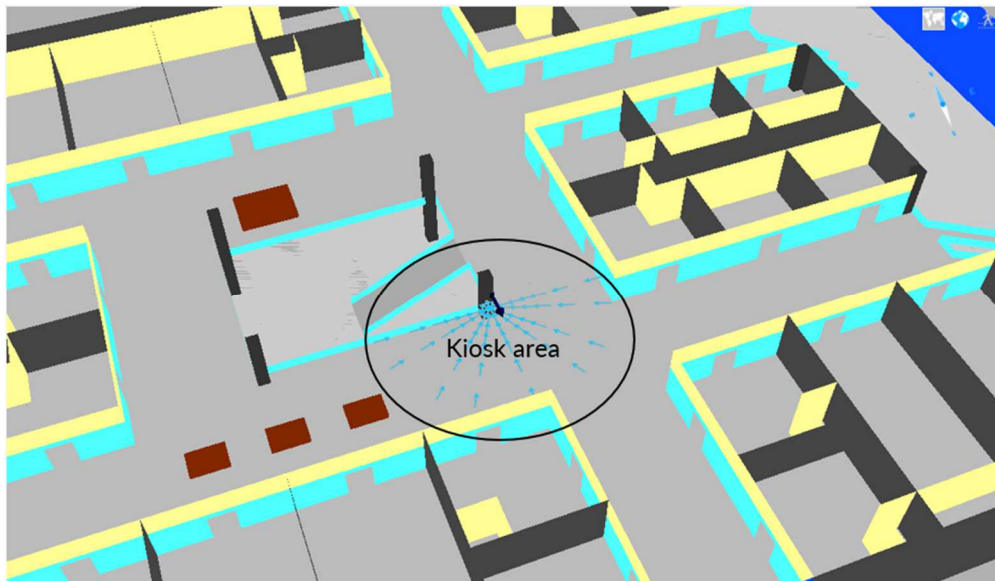


Figure 40 : Kiosk environment.

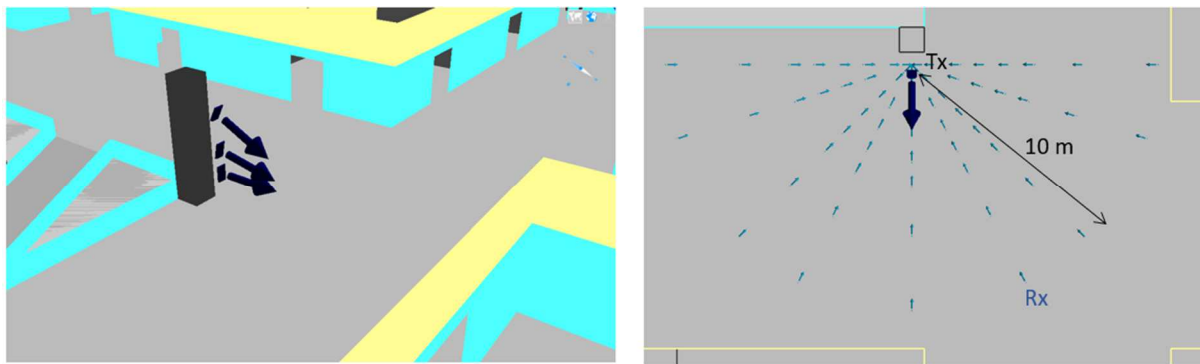


Figure 41 : Side view - three different considered transmitter heights and orientations (left); Top view – position and orientation of the receiver antennas (right).

Table 16 gives some additional details on the transmitter properties. Actually, we simulated twelve different transmitter situations, with an omni-directional or directional radiation pattern (at the antenna element), three different heights (see Fig. 18), and two polarization states (V/H or $+/-45^\circ$).

The receiver detailed properties are given in Table 17.

The predicted ray-paths in Figure 42 : Examples of prediction ray-paths. Figure 42 show that the LoS direct-path is dominant. However, there are some significant reflections on the ground, ceiling, pillar and surrounding walls that contribute to the channel diversity, thus leads to fading variations along the H matrix in both spatial and frequency dimensions. As expected, those variations reduce when changing the transmit omni-directional antenna for a directional pattern.

| Property | Details |
|----------------------------------|--|
| Location | <ul style="list-style-type: none"> Facing a large open area (intersection between corridors) A pillar (made of concrete) is located 50 cm behind the antenna The pillar width is 1 m No other object in the vicinity of the Tx antenna |
| Height | Three simulated heights: 1.5 m, 2.5 m and 4 m above ground The ceiling height is 5 m |
| Tx frequency | 150 GHz |
| Signal bandwidth | 2 GHz |
| Tx power | 0 dBm |
| Antenna array | Dual-polar elements distributed over a 16×8 rectangular array 16 columns \times 8 rows \times 2 polars \rightarrow 128 radiating elements Separation: $\lambda/2$ ($= 0.1$ cm) Polarization: either V/H or $\pm 45^\circ$ |
| Antenna orientation | Pointing towards the center of the considered reception area Downtilt = 0° , 11.3° and 26.5° at resp. height 1.5 m, 2.5 m and 4 m |
| Antenna radiation pattern | Pattern of each radiating element <ul style="list-style-type: none"> Either isotropic (0 dBi gain) Or directive (90° beamwidth, 0 dBi max gain) |

Table 16 : Parameters of the kiosk transmitter.

| Property | Details |
|----------------------------------|---|
| Location | 64 positions distributed within the LoS area facing the kiosk transmitters <ul style="list-style-type: none"> Distances 0.5 m, 1 m / Every 45° Distances 1 m, 2 m, 3 m, 4 m, 5 m, 7 m, 10 m / Every 30° |
| Height | 1.5 m above ground |
| Rx losses | 0 dB |
| Antenna array | Dual-polar elements distributed over a 8×8 rectangular array 8 columns \times 8 rows \times 2 polars \rightarrow 64 radiating elements Separation: $\lambda/2$ ($= 0.1$ cm) Polarization: either V/H |
| Antenna orientation | Horizontal pointing towards the kiosk antenna Downtilt = 0° |
| Antenna radiation pattern | Pattern of each radiating element: isotropic (0 dBi gain) |

Table 17 : Parameters of the kiosk receiver.

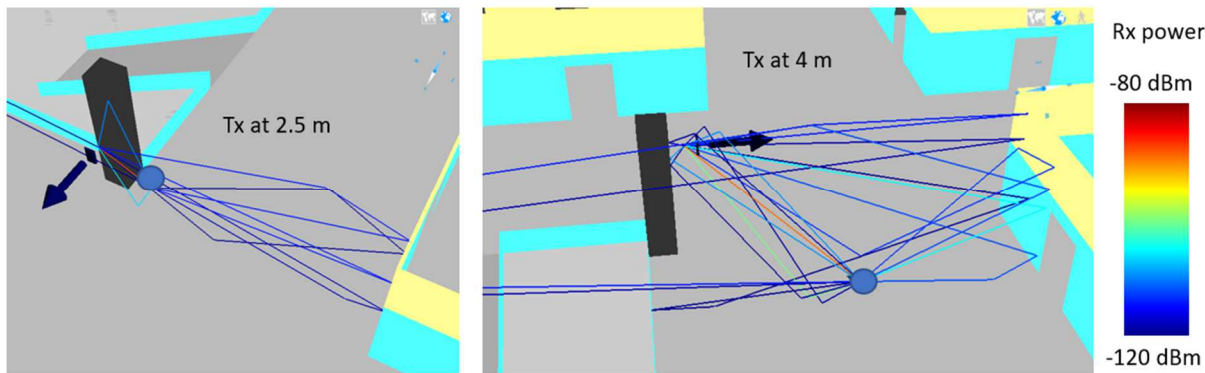


Figure 42 : Examples of prediction ray-paths.

Finally, Table 18 gives the list of MATLAB MIMO channel sample files that are available on the open repository. “BS” stands for “base station”, which is equivalent to the “transmitter” in this scenario.

A PDF document accompanies the MATLAB data files to further describe the scenario and give all information necessary for their exploitation.

| File name | Tx height | Tx radiating element | Tx polarization |
|--|-----------|----------------------|-----------------|
| BS 1-5m - Iso pm45 16x8 - Iso VH 8x8.zip | 1.5 m | Isotropic | V/H |
| BS 2-5m - Iso pm45 16x8 - Iso VH 8x8.zip | 2.5 m | Isotropic | V/H |
| BS 4m - Iso pm45 16x8 - Iso VH 8x8.zip | 4.0 m | Isotropic | V/H |
| BS 1-5m - Iso pm45 16x8 - Iso VH 8x8.zip | 1.5 m | Isotropic | $\pm 45^\circ$ |
| BS 2-5m - Iso pm45 16x8 - Iso VH 8x8.zip | 2.5 m | Isotropic | $\pm 45^\circ$ |
| BS 4m - Iso pm45 16x8 - Iso VH 8x8.zip | 4.0 m | Isotropic | $\pm 45^\circ$ |
| BS 1-5m - Dir pm45 16x8 - Iso VH 8x8.zip | 1.5 m | Directive | V/H |
| BS 2-5m - Dir pm45 16x8 - Iso VH 8x8.zip | 2.5 m | Directive | V/H |
| BS 4m - Dir pm45 16x8 - Iso VH 8x8.zip | 4.0 m | Directive | V/H |
| BS 1-5m - Dir pm45 16x8 - Iso VH 8x8.zip | 1.5 m | Directive | $\pm 45^\circ$ |
| BS 2-5m - Dir pm45 16x8 - Iso VH 8x8.zip | 2.5 m | Directive | $\pm 45^\circ$ |
| BS 4m - Dir pm45 16x8 - Iso VH 8x8.zip | 4.0 m | Directive | $\pm 45^\circ$ |

Table 18 : List of MIMO channel sample files.

5.2 Appendix B: Urban backhaul link analysis

This study was realized based on demonstrator #3 for characterization of mesh outdoor backhaul links that would use the P-QAM modulation at 150 GHz. Real lampposts in an urban area are considered as backhaul node candidates; then the performance of all possible links of range less than 200 meters

long is simulated and inserted into a statistical analysis. This was a preliminary case study before the backhaul network design reported in section 2.1 (however the mesh principle has been allowed).

5.2.1 System parameters and Scenario

The in-street backhaul scenario is run in a dense-urban densely-vegetated environment, San José downtown, California. The digital geographical data is composed of 3D vector buildings and a point cloud LiDAR data where trees and main street furniture e.g. lampposts are classified. A subset of 134 lampposts in this area is used as virtual sub-THz device positions. Antennas are localized at 8 meters above the ground. All possible lamppost-to-lamppost links with range lower than 200 meters are computed at frequency 150 GHz, leading to a total of 1873 predicted links.

The multiple propagation paths and their received power (or SNR) are computed by Volcano ray-tracing.

Mapping between SNR levels and spectral efficiency is derived from the previously described P-QAM modulation scheme and following assumptions. A perfectly synchronized single-carrier modulation is considered. The channel phase shift is perfectly estimated and corrected. A Forward Error Correction (FEC) scheme based on the 5G-NR LDPC with an input packet size of 1500 bytes is considered with a coding rate ranging from 0.3 to 0.9. The performance of the physical layer was first assessed to determine the best set of parameters: coding rate, modulation order and modulation shape given the SNR, the PN level and the targeted packet error rate of 10^{-2} . Resulting spectral efficiency with medium PN level goes from 0.6 bps/Hz at -0.8 dB SNR, to 7.2 bps/Hz at 29.7 dB SNR.

Table 19 : System parameters.

| Parameter | Value |
|-----------------------|---------------------------------|
| Frequency band | 150 GHz |
| Channel BW | 1 GHz |
| Tx power/ch. | 1 W |
| Tx antenna | 25.0 dBi |
| Rx antenna | 25.0 dBi |
| Th. noise floor | -84.0 dBm |
| Noise figure | 10 dB |
| Rx sensibility | -98.2 dBm |
| Implementation loss | 3.0 dB |
| Default rainfall rate | 12.5 mm/h |
| Default PN level | Medium ($\sigma^2 = 10^{-2}$) |
| Adj. factor | [-5;+5] dB |

The system is operating in the 150 GHz band, with a bandwidth of possibly several tenths of GHz, divided in 1-GHz channels. The effective bandwidth of the signal is 800MHz with a 20% overhead due to the control plane. The maximum reachable throughput is then 4.6 Gbps/channel. Parameters regarding the transmit power, antenna, and link budget are given in Table 19 for each simulated scenario. The adjustment factor in the last row of the table is used as a varying parameter to evaluate the sensibility of the simulated system to any change or uncertainty in the link budget. As an example,

a positive adjustment can be used to assess the impact of a larger transmit power or reduced noise figure.

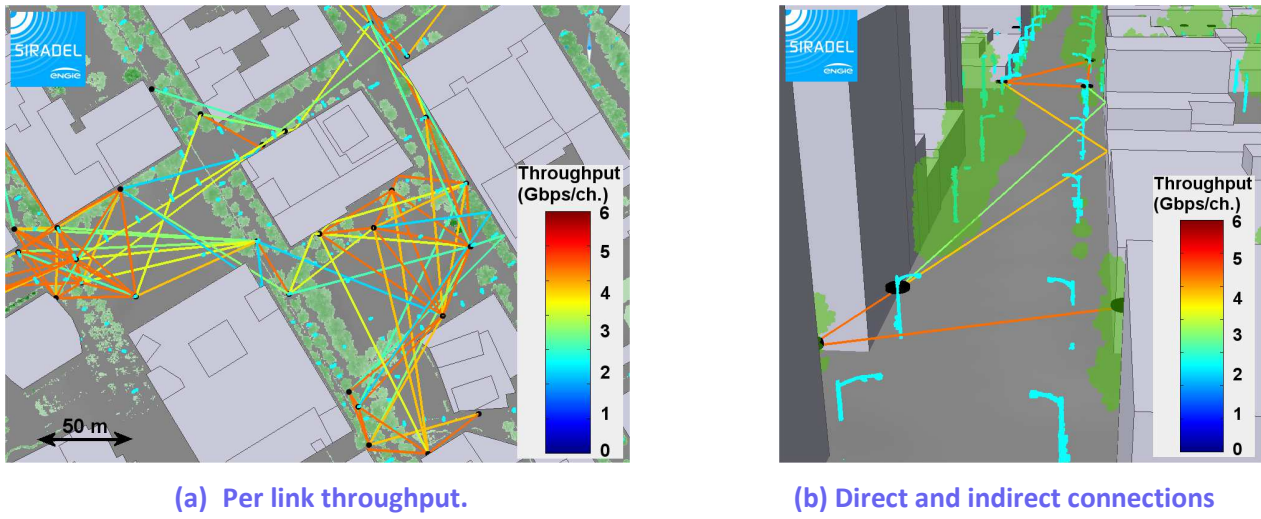


Figure 43: Predicted outdoor backhaul links.

5.2.2 Performance evaluation

The visibility conditions is first determined for each node-to-node link: 136 line-of-sight (LoS) links; 553 vegetation obstructions (Obstructed-LoS or OLoS); and 1204 building obstructions (Non-LoS or NLoS). A total of 585 links have sufficient SNR to establish a connection if antennas at both ends are perfectly aligned on the strongest propagation path. Figure 43 (a) shows the simulated connections with their achievable throughput in one part of the study area; maximum throughput can be reached in clear LoS, while the vegetation significantly degrades the performance. We note that a few connections are allowed in building shadowed area due to indirect paths. Figure 43 (b) zooms on some particular links and displays the main propagation paths, either line-of-sight or reflected along a trajectory out of any tree's obstruction.

Figure 44 (a) gives statistics on the achievable throughput versus the distance between antennas, and for two different situations: 1) in case of LoS/OLoS visibility; 2) in case of a NLoS building obstruction. In first case, 98% links with range below 25 meters reach a peak throughput greater than 4 Gbps/channel; the percentage drops to 81% and 52% for respectively the ranges $]25;50]$ and $]50;75]$ meters, due to more likely and longer obstructions. It further decreases below 35% when the range is longer than 75 meters. This result demonstrates that sub-THz hops longer than 75 meters can provide more than 4 Gbps/channel, but need to be carefully chosen, based on an accurate knowledge of the environment. Figure 44 (a) also gives the statistics for the Non-LoS links, and shows that indirect propagation paths can sometimes lead to high-throughput links, in particular for ranges below 75 meters, which may be very useful for creating a link between orthogonal streets or as a backup connection. Finally, in the last 175-200 meters range, the performance is strongly degraded for most of the predicted links; high-throughput connection is hardly possible.

The sensitivity of those results to the considered link budget parameters is illustrated in Figure 44 (b), where the percentage of connections is plotted as a function of the distance and an additional gain in

range [-5;+5] dB. A 4 dB adjustment in the link budget leads to 100% connection in the]0-25] meters range, while 8% links in same range are losing connection with -5 dB adjustment. Besides, the [-5;+5] dB gain converts into maximum 25% variation in the high-throughput connection rate, as observed in the]25-50] meters range.

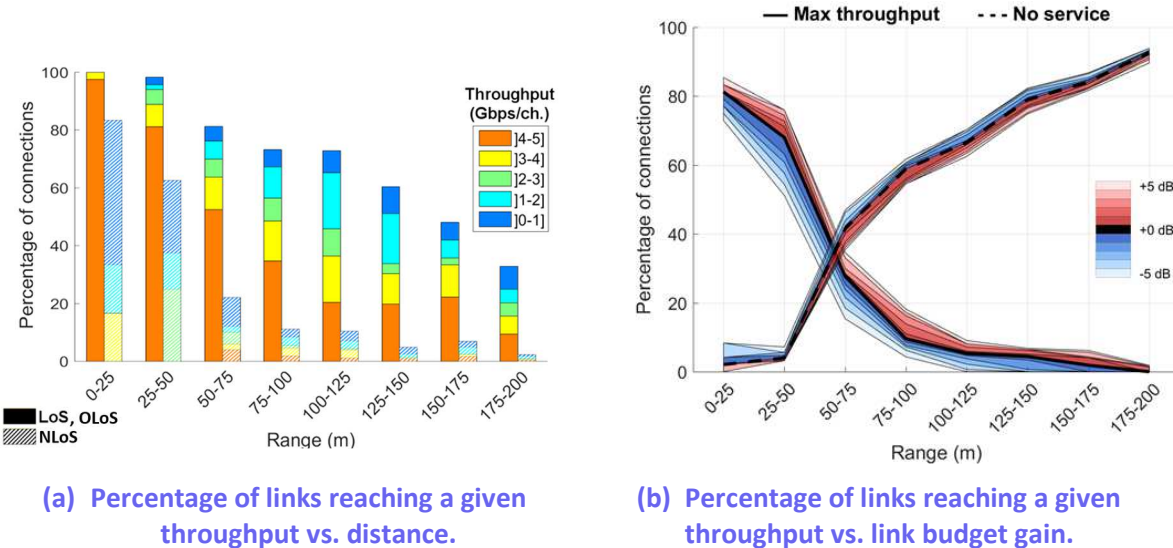


Figure 44: Simulated performance for the outdoor backhaul links.

Figure 45 indicates how many different propagation paths can be used by a node-to-node link in order to get connected, assuming the system is able to automatically align the Tx/Rx antenna beam towards the right departure/arrival directions. This result was computed from all links in range 0 – 200 meters, whatever the visibility situation, but with a non-zero data rate. About 50% of those links do have a single connection path (due to the propagation channel sparsity), while respectively 30% and 10% of the links benefit from 2 or 3 possible connections paths. This number is actually a kind of diversity indicator. Depending on the communication system, the available diversity may be exploited in different ways, either for overcoming an obstruction on the dominant path, or optimizing the routing and inter-link interference, or transmitting several data streams on separated beams. We imagine the links with more than one possible connection path are better candidates when designing a network.

Finally, we have studied the impact of the rainfall rate on the link performance. Previous results were obtained for a rate of 12.5 mm/h, which is exceeded for approximately 0.1% of the time over a year. The same simulation was run for a clear weather and a 30 mm/h rate (0.01% of the time). The resulting throughput statistics are plotted as a function of the distance in Figure 46, and compared. The different visibility conditions are not distinguished here (contrary to Figure 44 (a)) in order to make the illustration more compact. We observe the rainfall rate has no impact on the achievable throughput at ranges below 25 meters, which is normal as the attenuation is proportional to the distance. Throughput degradation increases with the range, as expected, but it remains small. When assessing the link performance at such ranges below 200 meters, the rain attenuation may be considered, but is obviously not a dominant factor. Precise knowledge of the geographical environment, presence of trees, or antenna misalignment issues, are more critical aspects.

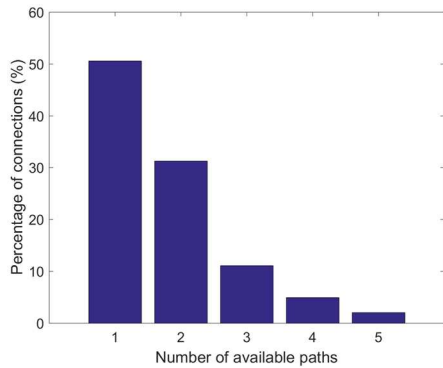


Figure 45: Statistics on the path diversity.

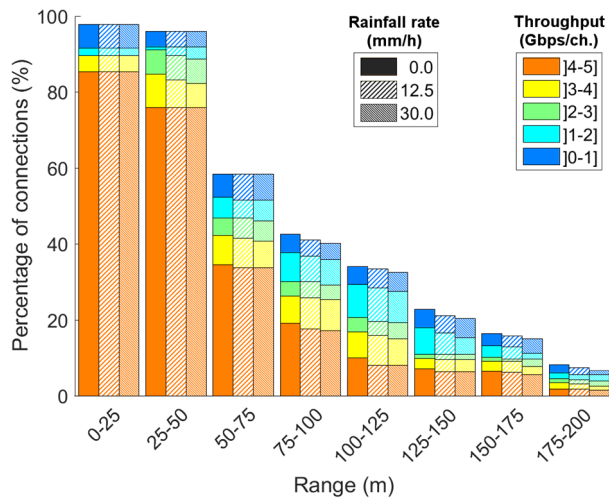


Figure 46: Impact of the rainfall rate on the achieved throughput.

5.2.3 Impact of the Phase Noise level

The phase noise (PN) level at the receiver might strongly affect the sub-THz backhaul link performance, and the modulation scheme must be appropriately selected depending on its robustness against PN impairments. Those considerations are illustrated in Figure 47, where coverage maps and throughput statistics are obtained with either no PN or strong PN ($\sigma_p^2 = 10^{-1}$), based on the traditional QAM or proposed P-QAM (named as the “optimized transceiver” in the figure). The coverage maps have been computed from a central transmitter node to any surrounding receiver pixel at 8 meters above the ground (remark the lampposts i.e. candidate node positions are represented by black circles). And the throughput statistics were simulated from the same links as presented above in the article. The QAM does slightly over-perform the P-QAM modulation in absence of any PN, with 2% more connected links in average. Same kind of improvement is observed under strong PN conditions, but then, the achievable throughput is limited below 2 Gbps/ch., while 64% of the LoS or obstructed-LoS links at ranges up to 100 meters can still reach between 3 and 4 Gbps/ch. thanks to the P-QAM optimization.

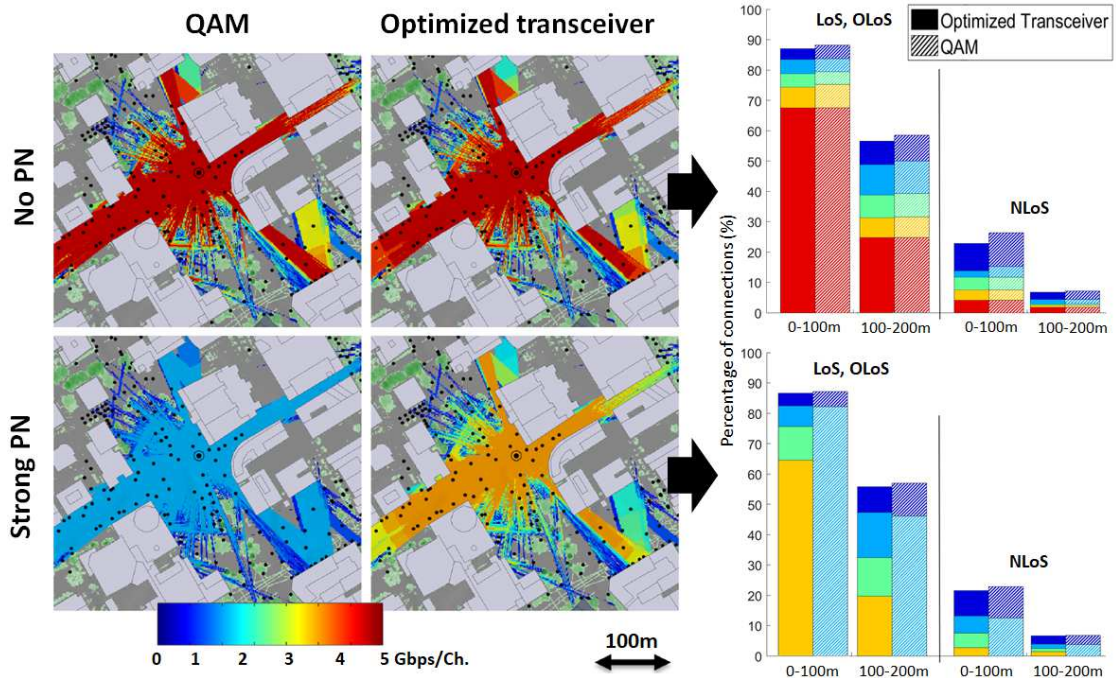


Figure 47: Performance for different PN levels and modulation schemes.

5.2.4 Conclusion

The presented simulation studies demonstrate the feasibility of sub-THz mesh backhaul networks, using a PN-robust modulation scheme, and considering real propagation constraints. This study shows the potential of the sub-THz technology to reach multi Gbps link in outdoor in-street typical scenarios, even in presence of strong phase noise. It is also observed that 50% of connected links have some multi-path diversity, which may be used for improving the capacity or protection of the network. The rainfall attenuation is found to have limited impact when radio links have a range inferior to 200 meters. And finally, the simulation illustrates the benefit of the P-QAM modulation, which permits a large amount of links to reach a throughput greater than 3 Gbps / 1GHz channel in presence of strong PN impairments.